Book of Abstracts

THE 46TH ANNUAL SYMPOSIUM ON POLYMER SCIENCE/ENGINEERING

University of Waterloo
Waterloo, Ontario

May 1st– 2nd, 2024

Institute for Polymer Research
University of Waterloo

The Institute for Polymer Research would like to thank the sponsors for their support of the symposium.

UNIVERSITY OF WATERLOO
FACULTY OF SCIENCE

UNIVERSITY OF WATERLOO
FACULTY OF ENGINEERING

UNIVERSITY OF
WATERLOO
OFFICE OF RESEARCH

UNIVERSITY OF WATERLOO
FACULTY OF SCIENCE
Department of Chemistry

UNIVERSITY OF WATERLOO
FACULTY OF ENGINEERING
Department of Chemical Engineering

2024

PROGRAM

INSTITUTE FOR POLYMER RESEARCH
CELEBRATING 40 YEARS OF OFFICIAL INSTITUTE STATUS
FORTY-SIXTH ANNUAL SYMPOSIUM
ON POLYMER SCIENCE/ENGINEERING 2024
E7 7303-7363
Faculty Hall
University of Waterloo, Waterloo, Ontario
Wednesday May 1 and Thursday May 2, 2024

8:45   a.m.   **Open Symposium Portal**

8:50   **Welcome and Opening Remarks**

9:00 – 9:20   **Sanjay Patel, Chemistry, Waterloo**
                        Could PEF Become the New FRET?
                        (Winner of 2023 IPR Award for Academic Excellence in Polymer Science/Engineering)

9:20 – 10:20   **Industry Speaker: Dr. Steven Teerstra, Arlanxeo.**
                        Elastomers in Commercial Applications – BR, SBR, and Butyl Rubber in Tires to Chewing Gum

10:20 – 10:55   **Coffee**

10:55 – 11:20   <u>**5-Min. Mini Presentations**</u>
                        1) Shayan Ghasemi
                           Unlocking the Potential of Interfacial Assembly for Aerogel Bead Fabrication
                        2) Monica Ho
                           Polymer-MOF Composite Scaffolds for Direct Air CO_2 Capture
                        3) Gillian Binley
                           Hydrogen Peroxide Induced Degradation of Poly(Lactic Acid)
                        4) Akliu Getnet Messele
                           Development of a Multi-filler Nanocompsite for Application of X-ray Shielding
                        5) Ethan Crawford
                           Melt-Blown Fibers for Oil Spill Remediation and Oil Barrier Geotextiles

10:20 – 11:40   **Ryan Lloyd**
                        Studying the Interactions Between DNA and Cationic Surfactants by Pyrene Excimer Fluorescence and Dynamic Light Scattering

11:40 – 12:00   **Debela Tadele**
                        Co-encapsulation of Quercetin and α-Tocopherol Bioactives in Zein Nanoparticles: Synergistic Interactions, Stability, and Controlled Release

12:00 – 1:00   **Lunch**

| 1:00 – 2:00 | **Academic presenter: Prof. Alex Penlidis** |
| | Copolymerization Composition Control Policies: Batch, Semi-batch or Flow? |

2:00 – 2:20   <u>**5-Min. Mini Presentations**</u>

           6)   **Aline Braz Ramirez**

              3D Printing of Soft-Gel with Bio-Derived Solvent for Biomedical Applications

           7)   **Shakiba Samsami**

              Chaotic 3D-Printing of Cellulose Nanocrystal-based Hydrogels for the Fabrication of Electromagnetic Shields

           8)   **Shikuan Xu**

              Chitosan Thermosensitive Hydrogel System

           9)   **Tobechukwu Ohaka**

              Designing Recyclable Natural Rubber – CNC Vitrimers

2:20 – 2:40   **Saba Karimi**

                                      Thermal Expansion Study on Polymer Stable Glasses

2:40 – 3:00   **Hunter Little**

                                      Probing the Local Density of Macromolecules by Fluorescence

                                      (Winner of the 2023 IPR Award for Academic Excellence in Polymer Science/Engineering)

3:00 – 3:40   **Coffee**

3:40 – 4:00   **Franklin Frasca**

                                      Determining the Conformations of Pyrene-Labeled Polyamines and Polyols in Solution via Pyrene Excimer Fluorescence

4:00 – 4:20   **Kristijan Lulic**

                                      Pyrene Excimer Formation as a Means to Investigate Persistence Length of Alkyl Methacrylate Copolymers

4:20 – 4:40   **Shahrzad Ghodrati**

                                      Sensing the Invisible: An Overview of Polymeric Materials for Gas Detection

4:40 – 5:00   **Saeed Hadad**

                                      Highly Conductive MXene Quantum Dots/Starch Nanocomposite Polymer Electrolytes for All-Solid-State Lithium-Ion Batteries: Unveiling Insights for Future Sustainable Energy Storage

5:00-5:15   <u>**5-Min. Mini Presentations**</u>

          10) **Estatira Amirieh**

              Conductive Bacteria Cellulosic Scaffolds

          11) **Naixin Zhao**

              Hydrogen-bond Bearing Conjugated Polymer for Fluoride Sensing

12) Talha Ince
Non-Invasive Sweat Induction for Wearable Sweat-Based Biosensors

5:15   **Closing remarks**

SANJAY PATEL
Chemistry
Waterloo

Could PEF Become the New FRET?

Winner of the 2023 IPR Award for Academic Excellence in Polymer Science/Engineering

Sanjay Patel Biography:
Sanjay Patel graduated with a PhD from the University of Waterloo under the supervision of Prof. Jean Duhamel and is currently pursing his postdoctoral fellowship at the University of Toronto under the supervision of Prof. Mitch Winnik. Over his academic career he has focused on the synthesis and characterization of pyrene labelled macromolecules which he employed to demonstrate experimentally the correlation that exists between pyrene excimer formation (PEF) and the local pyrene concentration, a relationship which has never been proven before. A significant contribution of his work was to show that PEF can be used to provide conformational information on complex macromolecules, in a manner that complements experiments based on scattering techniques or fluorescence resonance energy transfer (FRET).

Could PEF Become the New FRET

Sanjay Patel and Jean Duhamel
Institute for Polymer Research, Waterloo Institute for Nanotechnology, Department of Chemistry, University of Waterloo, ON N2L 3G1, Canada

INTRODUCTION

Förster resonance energy transfer (FRET) occurs when energy is transferred, via dipole-dipole interactions, from an energy donor to an energy acceptor, as demonstrated by the theorical work of Theodore Förster in 1967.[1] A key feature stemming from this theoretical work was that the FRET efficiency (E_{ET}) depends strongly on the distance (R) separating the donor and acceptor dye. This feature was later validated experimentally by Stryer and Haughland in 1967 through a series of experiments using monodisperse oligoproline samples which had been labeled at either end with an acceptor and donor dye.[2] It was this study which established FRET as a "*spectroscopic ruler*" and led to the widespread application of FRET to study the conformation and dynamics of macromolecules in solution. In contrast to the workhorses' of macromolecular conformation characterization, namely scattering and nuclear magnetic resonance (NMR) experiments, FRET has three main advantages. First, E_{ET}, as well as the rate constant of energy transfer (k_{ET}), strongly depend on R. This effectively enables the experimentalist to measure intramolecular distances which, in turn, provides information on macromolecular conformation. Second, fluorescence experiments are conducted at an extremely low concentration (~1 mg/L) of macromolecule compared to scattering (1–40 g/L)[3,4,5] and NMR (1–20 g/L)[6,7] experiments. The extremely low concentrations used in fluorescence experiments thus enable the quantitative characterization of isolated macromolecules in solution. Third, the Förster radius (R_0) characterizes the length scale over which FRET occurs, which defines the distances being probed in the macromolecule by the experimentalist. R_0 values of typical donor-acceptor pairs range from 1–10 nm.[8]

While FRET is touted as a "*spectroscopic ruler*" due to the strong R-dependency, the drawbacks associated with the strong R-dependency is a less acknowledged fact. First, to use FRET as a *spectroscopic ruler* the macromolecule must be attached with a donor and acceptor at two specific positions on the macromolecules. This is because attachment of more then one donor and one acceptor on a macromolecule would yield a distribution of R-distances that would complicate the retrieval of quantitative spatial information. Therefore, to determine the unknown

conformation of a macromolecule using FRET, the experimentalist must do so one distance at a time. Second, FRET can not be used to quantitatively analyze the conformation of flexible macromolecules, as any motion in the macromolecule would result in the displacement of the donor and acceptor dyes, which would affect R and would need to be accounted for. This can be done if the macromolecular conformation is already known, but not for unknown macromolecular conformations. Third, the strong R^6-dependency of k_{ET} and E_{ET}, which endows FRET with outstanding distance sensitivity, implies that it is only related to the local acceptor concentration ($[A]_{loc}$). This is rather unfortunate, as $[A]_{loc}$ reflects the local density of the macromolecule, and thus macromolecular conformation. In contrast to FRET, pyrene excimer formation (PEF), where pyrenyl labels are covalently attached on a macromolecule, is directly proportional to the local concentration of pyrene ($[Py]_{loc}$) in the macromolecule and can thus provides direct insight on macromolecular conformation.[9] Furthermore, PEF can be used to probe macromolecules where pyrene has been randomly attached onto the macromolecule.[10-14] Although there are many pyrene labeled macromolecules which have been characterized, typically pyrene derivatives with alkyl linkers of 2 to 4 carbons are employed. This would equate to a maximum length scale (L_{Py}) probed by PEF equal to ~4.0 nm, which, admittedly, is rather limited compared to the range of length scales available via different FRET donor-acceptor pairs. Therefore, the present study has two objectives. First, to extend and demonstrate that the maximum range over which PEF occurs (L_{Py}) can be adjusted to reach length scales comparable to those achieved via FRET experiments by simply extending the length of the alkyl linker connecting the pyrene dye to the polymer backbone. To this end, a series of pyrene-labeled poly(glutamic acid) samples were characterized in N,N' dimethylformamide (DMF) and dimethyl sulfoxide (DMSO), where the conformation for a poly(D,L) and (L) glutamic acid (PDLGA and PLGA) were known to be a random coil (in DMF and DMSO) and α-helix (in DMF), respectively. The 1-pyrenealkylamine (PyC$_X$NH$_2$) derivatives chosen in this present study were 1-pyrene methyl (X=1), butyl (X=4) and -octylamine (X=8), which resulted in L_{Py} equal to 4.0, 5.7 and 7.7 nm. This study essentially served to demonstrate first, that PEF can be viewed as a new '*spectroscopic ruler*' and second, that PEF presents important advantages compared to FRET, namely that macromolecules where the dyes have been randomly attached onto the macromolecular backbone can be analyzed. This, in turn, enables the experimentalist to analyze the unknown conformation of the macromolecule. Specifically, in the present study the unknown conformation of a PLGA chain in DMSO was determined to be a 3_{10}-helix.

EXPERIMENTAL
PLGA and PDLGA with a degree of polymerization equal to 830 (M_n = 125,300 g/mol, PDI =1.01) and 784 (M_n = 118,400 g/mol, PDI =1.06) were purchased from Alamanda Polymers Inc. The N-terminus of the polypeptide chains were capped with succinimidyl acetate and subsequently purified by dialysis. Water was removed by lyophilization. 1-Pyrenealkylamine derivatives (PyC$_X$NH$_2$ with X = 4 and 8) were synthesized according to Scheme 1,[15,16] while 1-pyrenemethylamine (PyC$_1$NH$_2$) was purchased from Aldrich. The pyrene-labeling of PLGA and PDLGA was done with EDC-HCl as coupling agent as reported elsewhere.[17] The pyrene contents ranged from 2 to 10 mol% and from 1 to 5 mol% for PyC$_4$NAH$_2$ and PyC$_8$NH$_2$, respectively.
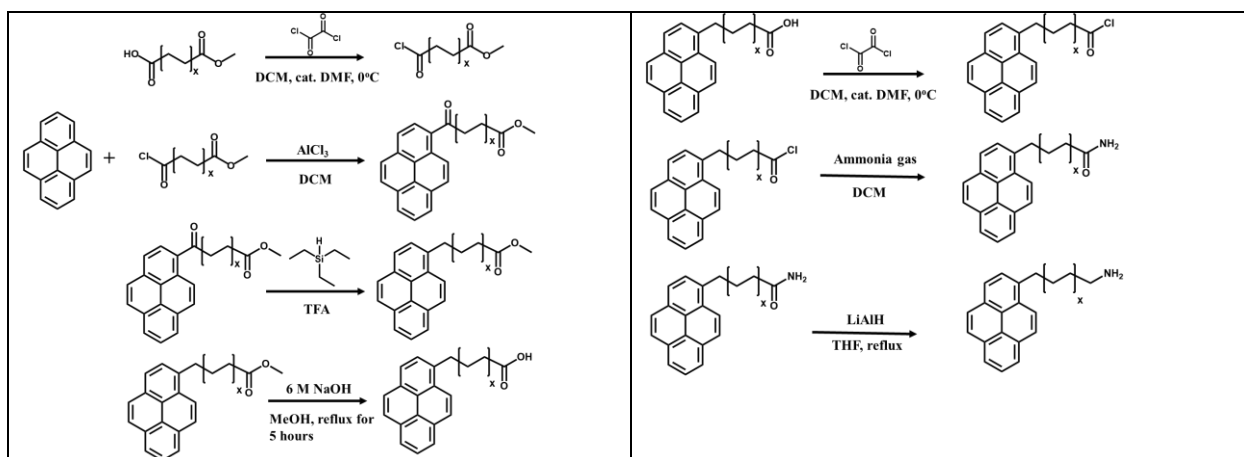
Scheme 1. Synthesis of pyrene derivatives.

The monomer and excimer fluorescence decays were acquired in DMF and DMSO. They were globally analyzed with the fluorescence *blob* model (FBM) to determine the number (N_{blob}^{exp}) of structural units located inside the volume probed by an excited pyrenyl labels called a *blob* for each pyrene content. For a given set of samples, N_{blob}^{exp} was averaged over all pyrene contents to yield $<N_{blob}^{exp}>$. $<N_{blob}^{exp}>$ was compared to N_{blob}^{MMO} determined by molecular mechanic optimizations (MMO) conducted for an α-helix ($\Phi = -58$ °, $\Psi = -47$ °, $\Omega = 180$ °), a 3_{10}-helix ($\Phi = -49$ °, $\Psi = -26$ °, $\Omega = 180$ °), a polyproline type II (PPII) helix ($\Phi = -75$ °, $\Psi = -145$ °, $\Omega = 180$ °) and a random coil (RC). A random coil was generated in HyperChem by placing a restraint of 999 Å between the amino and carboxylic end of an α-helix prepared with 42 glutamic acids. The restraints were removed, and the oligopeptide was allowed to relax. The MMOs for a random coil were conducted 3 times. For all MMOs, a pyrenyl label was placed on the 7th residue, which was denoted as the reference residue. Another pyrenyl label, referred to as secondary pyrene label, was placed on the residue adjacent to the reference residue. The backbone of the peptide was fixed, and the reference and secondary pyrenyl labels were induced to come within 3.4 Å from each other. Since the pyrenyl derivatives were attached onto two successive amino acids (*aa*'s), they had no problem overlapping and the extent of overlap was assessed from the number of carbons of one pyrene overlapping the frame of the other pyrene. Once completed, the secondary pyrenyl label was moved over by one residue and the MMO was conducted again to determine the extent of overlap between the two pyrenyl labels. The process was repeated until the secondary and reference pyrene could no longer touch. PEF occurs only if 7 or more carbons of the reference pyrene overlap the frame of the secondary pyrene and if the pyrenyl units remained planar. The number of times, that this condition was met, represented the reach (N_0) of the reference pyrene toward one side of the polymer. Since the pyrene can reach on the left and right of the helix, N_{blob}^{MMO} was taken as $2 \times N_0 + 1$, where 1 was added to account for the reference residue.

RESULTS AND DISCUSSION

Conformation of PLGA and PDLGA by CD and NMR: Prior to studying the conformation of the pyrene-labeled P*L*GA and P*DL*GA samples in DMF and DMSO, the conformation and conformational changes of unmodified P*L*GA and P*DL*GA chains were studied using circular dichroism (CD) and nuclear magnetic resonance (NMR) spectroscopy. In Figure 1A, the unmodified P*DL*GA had the typical features expected for a random coil conformation, namely a peak maximum centered at ~220 nm followed by a peak minimum centered at ~199 nm, and served to demonstrated that the P*DL*GA samples used in the present study adopt a random coil

10

conformation regardless of pH. P*DL*GA should also retain a random coil conformation in the two organic solvents used in the present study. At high pH P*L*GA has spectral features conducive of a random coil conformation, as would be expected since deprotonation of the P*L*GA carboxylic acid side chains result in electrostatic repulsion destabilizing the α-helical conformation.[18] The same P*L*GA acquired at low pH resulted in the typical CD spectrum expected for an α-helical conformation, namely a double peak minimum at ~222 and ~ 209 nm followed by a peak maximum at ~198 nm.[19] In Figure 1 B&C the NMR of the P*DL*GA and P*L*GA samples were acquired in DMF and DMSO, respectively. Although the exact conformation cannot be determined from the chemical shift of the α-CH proton, the presence of secondary structure can be inferred. Specifically, the signal for the α-CH proton obtained for the P*DL*GA sample is shifted downfield in both Figure 1B & C relative to that of the P*L*GA samples in either DMF or DMSO. This shift suggests the presence of secondary structure in both DMF and DMSO, however it is only in DMF where the conformation of P*L*GA is known to be an α-helix.[20]
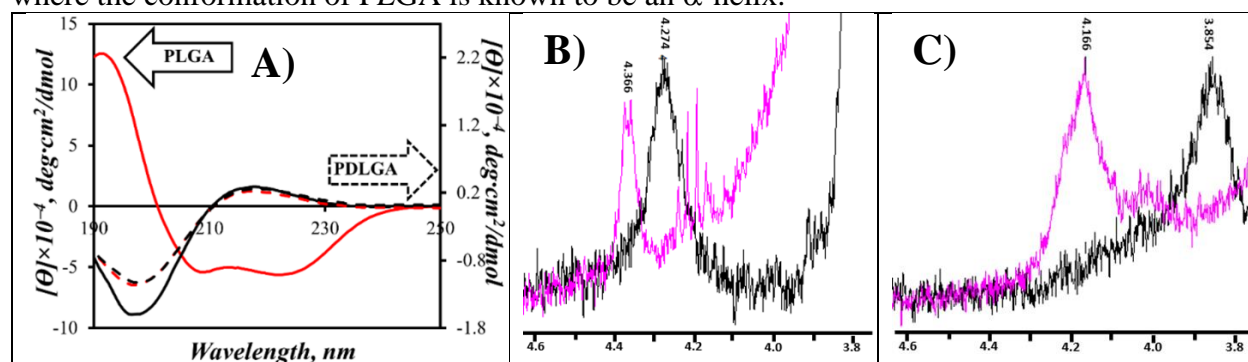
Figure 1. A) Plot of the molar ellipticity as a function of wavelength for (solid) PLGA and (dashed) PDLGA acquired with 10 mM of (black) NaOH or (red) HCl. Region between 3.7 and 4.6 ppm of the ^{1}H NMR spectrum showing the signal from the α-CH proton for (black) PLGA and (purple) PDLGA acquired in B) d_7-DMF and C) d_6-DMSO. [PLGA] = 1 mg/mL and [PDLGA] = 10 mg/mL.

Conformation of PLGA and PDLGA in DMF and DMSO: To establish PEF as a new '*spectroscopic ruler*', the information extracted from the global analysis of the monomer and excimer decays requires the development of a methodology that is benchmarked against polypeptides with a known conformation solution. To this end, the monomer and excimer decays of the P*DL*GA (PyC$_X$(x)-P*DL*GA) and P*L*GA (PyC$_X$(x)-P*L*GA) samples labeled with a 1-pyrenealkylamine derivative, where X and x are the number of carbons in the alkyl linker of the pyrene derivative used and the mole percent of glutamic acids labeled with pyrene, respectively, were acquired in DMF and DMSO. They were analyzed using the FBM to determine the average number $<N_{blob}^{exp}>$ of structural units within a blob. $<N_{blob}^{exp}>$ was found to equal 11 ($\pm$2),[12] 15 ($\pm$2) and 21 ($\pm$2) for the PyC$_1$(x)PDLGA, PyC$_4$(x)PDLGA, and PyC$_8$(x)PDLGA samples, respectively, regardless of solvent. In Figure 2A, comparison of $<N_{blob}^{exp}>$ with N_{blob}^{MMO} determined from Hyperchem simulations using a P*L*GA chain which adopts a random coil, polyproline type II helix, 3_{10}-helix, and α-helix, a good agreement between $<N_{blob}^{exp}>$ and N_{blob}^{MMO} for a random coil conformation occurs, as would be expected based off the CD measurements and NMR studies in Figure 1. In the case of PyC$_1$(x)PLGA, PyC$_4$(x)PLGA and PyC$_8$(x)PLGA in DMF $<N_{blob}^{exp}>$ values were found to equal 21($\pm$1),[12] 30 ($\pm$3), and 42 ($\pm$3), respectively. The comparison shown in Figure 2B reveals a good agreement between $<N_{blob}^{exp}>$ and N_{blob}^{MMO} values for a P*L*GA

chain adopting an α-helical conformation, once again as would be expected in DMF which is known to be a helicogenic solvent. The finding that $PyC_X(x)$-PDLGA (in DMF and DMSO) and $PyC_X(x)$-PLGA (in DMF) were a random coil and an α-helix, respectively, established that the PEF-based experiments could be used to probe macromolecular conformation on different length scales. The methodology established in the present study was extended to determine the conformation of PLGA in DMSO. $<N_{blob}^{exp}>$ values were found to equal to 18(±1),[12] 24 (±3), and 33 (±3) for $PyC_1(x)$PLGA, $PyC_4(x)$PLGA and $PyC_8(x)$PLGA in DMSO, respectively. In Figure 2C, $<N_{blob}^{exp}>$ matched best with N_{blob}^{MMO} for a 3_{10}-helix, which demonstrated that PLGA adopts a 3_{10}-helical conformation in DMSO.
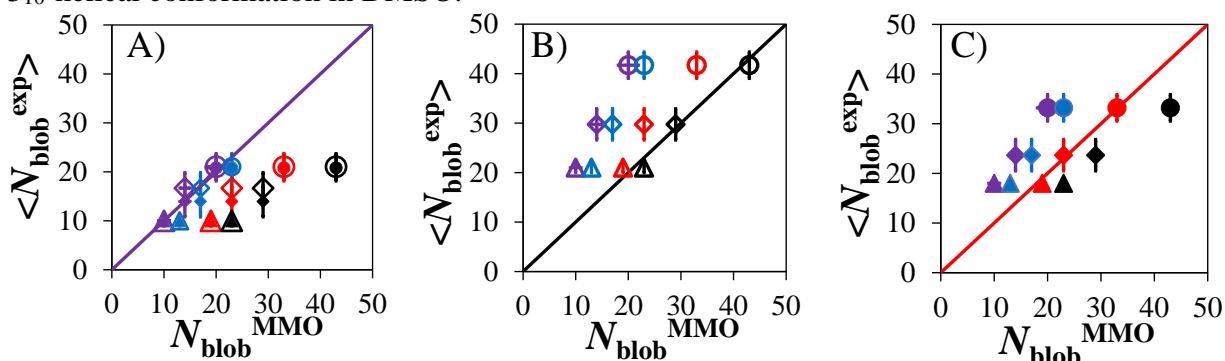
Figure 2. Plot of $<N_{blob}^{exp}>$ for (▲) PyC_1,[12] (◆) PyC_4, and (⬤) PyC_8 labeled A) PDLGA in (hollow) DMF or (filled) DMSO and PLGA in B) DMF or C) DMSO as a function of N_{blob}^{MMO} for (purple) a random coil or (blue) a PPII-, (red) 3_{10}-, and (black) α-helix. The solid line represents the 1:1 diagonal, where data points that land on the 1:1 diagonal demonstrate a good agreement between the $<N_{blob}^{exp}>$ and N_{blob}^{MMO} values.

CONCLUSION

The conformation of the PDLGA and PLGA samples were characterized on different length scales in DMF and DMSO via the use of a series of 1-pyrenenalkylamine derivatives to probe a maximum length scale ranging from 4.0 to 7.7 nm. This study has established that PEF can be viewed as a new '*spectroscopic ruler*', with a length scale on par with FRET experiments (1-10 nm), however with the significant advantage of being able to probe the conformation of macromolecules where the dyes have been randomly attached onto the macromolecules. It is this feature which enabled the determination that the PLGA chains in DMSO form a 3_{10}-helix.

REFERENCES

1. Forster, T. Energy Migration and Fluorescence. *J. Biomed. Opt.* **2012**, *17*, 1-10.
2. Stryer, L.; Haugland, R. Energy Transfer: A Spectroscopic Ruler. *Proc. Natl. Acad. Sci. U.S.A* **1967**, *2*, 719-726.
3. Tuukkanen, A. T.; Spilotros, A.; Svergun, D. I. Progress in Small-Angle Scattering from Biological Solutions at high-Brilliance Synchrotron. IUCrJ. **2017**, *4*, 518−528.
4. Skou, S.; Gillilan, R. E.; Ando, N. Synchrotron-Based Small-Angle X-Ray Scattering of Proteins in Solution. Nat. Protoc. **2014**, *9*, 1727-1739.
5. Liu, Y.; Chen, Y.-C.; Chen, L.-H.; Hong, K.; Shew, Y.-C.; Li, X.; Liu, L.; Melnichenko, Y.; Smith, G. Electrostatic Swelling and Conformational Variation Observed in High-Generation Polyelectrolyte Dendrimers. *J. Phys. Chem. Lett.* **2010**, *1*, 2020– 2024.

6. Joseph, P. R. B.; Sepuru, K. M.; Poluri, K. M.; Rajarathnam, K. Solution NMR Spectroscopy for Characterizing Protein-Glycosaminoglycan Interactions. *Methods Mol. Biol.* **2022**, *2303*, 13-23.

7. Diaz, D.; Canales-Mayordomo, A.; Canada, F. J.; Jimenez-Barbero, J. Solution Conformation of Carbohydrate: A View by Using NMR Assisted by Modeling. *Methods Mol. Biol.* **2015**, 1273, 261-287.

8. Shrestha, D.; Jenei, A.; Nagy, P.; Vereb, G.; Szöllősi, J. Understanding FRET as a Research Tool for Cellular Studies. *Int. J. Mol. Sci.* **2015** *16*, 6718-6756.

9. Little, H.; Patel, S.; Duhamel, J. Probing the Inner Local Density of Complex Macromolecules by Pyrene Excimer Formation. *Phys. Chem. Chem. Phys.* **2023**, *25*, 26515-26525.

10. Thoma, J. L.; Duhamel, J. Characterization of the Local Volume Probed by the Side Chain Ends of Poly(oligo(ethylene glycol) 1-Pyrenemethyl ether methacrylate) Bottle Brushes in Solution Using Pyrene Excimer Fluorescence. *Macromolecules* **2021**, *54*, 9341-9350.

11. Mathew, A.; Siu, H.; Duhamel, J. A *Blob* Model to Study Chain Folding by Fluorescence. *Macromolecules* **1999**, *32*, 7100-7108.

12. Casier, R.; Duhamel, J. Pyrene Excimer Fluorescence as a Direct and Easy Experimental Means to Characterize the Length Scale and Dynamics of Polypeptide *Foldons*. *Macromolecules* **2018**, *51*, 3450-3457.

13. Li, L.; Kim, D.; Zhai, X.; Duhamel, J. A Pyrene Excimer Fluorescence (PEF) Study of the Interior of Amylopectin in Dilute Solution. *Macromolecules* **2020**, *53*, 6850-6860.

14. Li, L.; Duhamel, J. Conformation of Pyrene-Labeled Amylose in DMSO Characterized with the Fluorescence Blob Model. *Macromolecules* **2016**, *49*, 7965-7974.

15. Winnik, F. Fluorescence Studies of Aqueous Solutions of Poly(N-isopropylacrylamide) below and above their LCST. *Macromolecules* **1990** 23, 233-242.

16. Lau, G.; Sathe, N.; Sai, H.; Waring, E.; Yehiely, E.; Barreda, L.; Beeman, Emily.; Palmer, L.; Stupp, S. Oriented Multiwalled Organic-Co(OH)2 Nanotubes for Energy Storage. *Adv. Funct. Mater.* **2017**, *28*, 1702320.

17. Duhamel, J.; Kanagalingam, S.; O'Brien, T.; Ingratta, M. Side-Chain Dynamics of an a-Helical Polypeptide Monitored by Fluorescence. *J. Am. Chem. Soc.* **2003**, *125*, 12810-12822.

18. Donten, M.; Hamm, P. pH-Jump Induced a-Helix Folding of Poly-L-Glutamic Acid. *Chem. Phys.* **2013**, *422*, 124-130.

19. Rodger, A.; Marshal, D. Beginners Guide to Circular Dichroism. *Bichem.* (*Lond.*) **2021**, *43*, 58-64.

20. Matsumoto, M.; Watanabe, H.; Yoshioka, K. Electric and Hydrodynamic Properties of Polypeptides in Solution. II. Conformational Change of Poly(L-glutamic Acid) in Various Organic Solvents. *Biopolymers* **1970**, *9*, 1307-317.

DR. STEVEN TEERSTRA
Industrial Presenter
Arlanxeo Canada Inc.

Elastomers in Commercial Applications – BR, SBR, and Butyl Rubber in Tires to Chewing Gum

ABSTRACT: Elastomers in Commercial Applications - BR, SBR and Butyl Rubber in Tires to Chewing Gum

Presentation by Dr. Steve Teertstra, Technical Service and Development Manager NORAM Region, ARLANXEO Canada Inc.

Structure-property relationships of synthetic polybutadiene (BR), polybutadiene-polystyrene copolymers (SBR) and butyl rubber (IIR) will be discussed. An overview of the commercial production processes will be reviewed, leading to the unique properties required for the applications of each type of elastomer. Specific focus will be given during the presentation to the usage of these three types of synthetic elastomers in tires, and the technology that has developed in the materials due to the ever-increasing demands for improved performance. The unique property requirements of other application areas will also be discussed, including plastics modification, pharmaceutical closures, golf ball and chewing gum.

Steve Teertstra Biography: Steve received both his undergraduate degree (Biochemistry '99) and graduate degree (Ph.D '06) from the University of Waterloo, under the supervision of Prof. Mario Gauthier investigating the structure-property relations of arborescent polymers. Following successful completion of his graduate degree, he accepted a post-doctoral fellowship with Prof. Michael Georges at the University of Toronto working on various projects in the area of controlled radical polymerization. Steve accepted a job at LANXESS, which has since transitioned to ARLANXEO in 2007. He has had various roles within the company, including Butyl R&D new product development, production, process support chemistry and now is working with the commercial team in a technical role supporting existing and new products directly at customers.

SHAYAN GHASEMI
Chemical Engineering
Waterloo

Unlocking the Potential of Interfacial Assembly for Aerogel Bead Fabrication

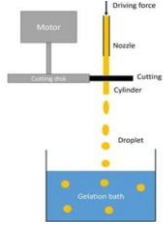Unlocking the Potential of Interfacial Assembly for Aerogel Bead Fabrication

IPR Presenter: Shayan Ghasemi

Supervisor: Dr.Milad Kamkar

3/1/2024

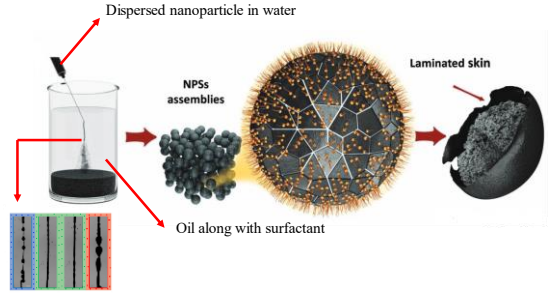## Introduction

What is aerogel?

What is aerogel properties?

Traditional aerogel bead fabrication

PAGE 2

Aerogel Fabrication based on Interfacial Layer

Dispersed nanoparticle in water

Oil along with surfactant
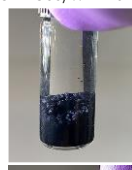
Plateau–Rayleigh instability

PAGE 3

Aerogel Beads

Oil-POSS/W-GO   Oil-POSS/W-MXene   Oil-POSS/W-CNC   Oil-POSS/W-CNF

PAGE 4

Hybrid Aerogels System

Layer by layer and mixed hybrid systems of Mxene, CNC, CNF and GO aerogel beads

PAGE 5

Hybrid Aerogel System

Hybrid freeze dried system

PAGE 6

17

MONICA HO
Chemical Engineering
Waterloo

Polymer-MOF Composite Scaffolds for Direct Air CO$_2$ Capture

Polymer-MOF Composite Scaffolds for Direct Air CO$_2$ Capture
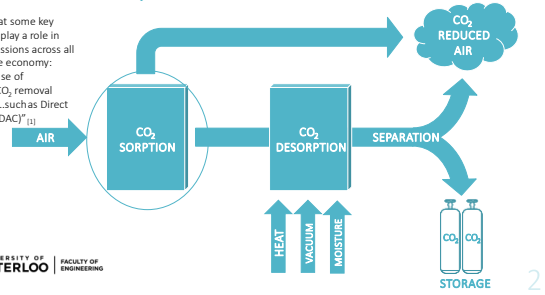
Monica Ho

UW IPR Symposium May 1, 2024
Supervisors: Eric Croiset, Milad Kamkar

UNIVERSITY OF WATERLOO | FACULTY OF ENGINEERING

KMKR LAB
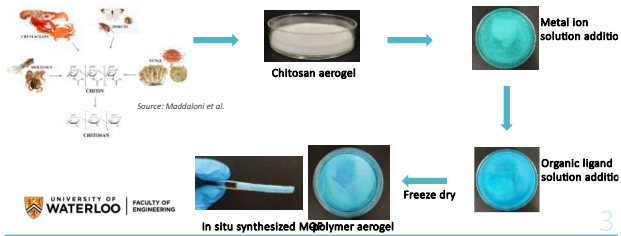Multiscale Materials Design (MMD)

Direct Air Capture

"it is clear that some key enablers will play a role in reducing emissions across all sectors of the economy: ...increased use of engineered CO$_2$ removal technologies..such as Direct Air Capture (DAC)" [1]

AIR → CO$_2$ SORPTION → CO$_2$ DESORPTION → SEPARATION → CO$_2$ REDUCED AIR

HEAT | VACUUM | MOISTURE

STORAGE

UNIVERSITY OF WATERLOO | FACULTY OF ENGINEERING
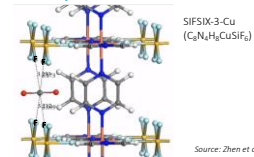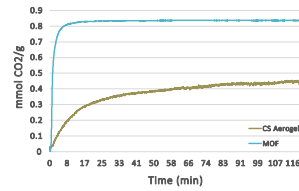
2

Polymer-MOF Aerogel Adsorbent

Metal organic frameworks (MOFs): highly porous crystalline nanomaterials

Chitosan: bio-based polymer obtained from crustaceans, molluscs, fungi, and insects
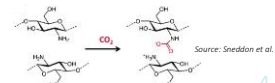

Source: Maddaloni et al.

Chitosan aerogel → Metal ion solution additio

Organic ligand solution additio → Freeze dry → In situ synthesized MOF-polymer aerogel

UNIVERSITY OF WATERLOO | FACULTY OF ENGINEERING

3

CO$_2$ Adsorption Preliminary Results

mmol CO2/g vs Time (min)
— CS Aerogel
— MOF

SIFSIX-3-Cu
(C$_8$N$_4$H$_6$CuSiF$_6$)

Source: Zhen et al.

Source: Sneddon et al.

UNIVERSITY OF WATERLOO | FACULTY OF ENGINEERING

4

UNIVERSITY OF WATERLOO

FACULTY OF ENGINEERING

Thank you for you attention!

References

[1] Environment and Climate Change Canada, Exploring Approaches for Canada's Transition to Net-Zero Emissions (2022), 41. https://unfccc.int/process/the-paris-agreement/long-term-strategies

[2] M. Maddaloni, I. Vassalini, I. Alessandri, Green Routes for the Development of Chitin/Chitosan Sustainable Hydrogels, Sustainable Chemistry 2020, Vol. 1, Pages 325-344 1 (2020) 325–344. https://doi.org/10.3390/SUSCHEM1030022.

[3] H.-G. Zhen, H. Mao, I.U. Haq, S.-H. Li, A. Ahmad, Z.-P. Zhao, In-situ SIFSIX-3-Cu growth into melamine formaldehyde sponge monolith for CO2 efficient capture, Sep. Purif. Technol. 233 (2020) 116042. https://doi.org/10.1016/j.seppur.2019.116042

[4] G. Sneddon, A.Y.Ganin, H.H.P.Yiu, Sustainable CO2 Adsorbents Prepared by Coating Chitosan onto Mesoporous Silicas for Large-Scale Carbon Capture Technology, Energy Technol. 3 (2015) 249–258. https://doi.org/10.1002/ente.201402211.

UNIVERSITY OF WATERLOO | FACULTY OF ENGINEERING

6

GILLIAN BINLEY
Chemical Engineering
Waterloo

Hydrogen Peroxide Induced Degradation of Poly(Lactic Acid)

Slide 1

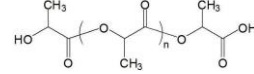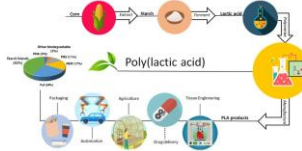# HYDROGEN PEROXIDE INDUCED DEGRADATION OF POLY(LACTIC ACID)

01May2024

Gillian Binley
Chemical Engineering

UNIVERSITY OF WATERLOO

Slide 2

Introduction to PLA

- Thermoplastic
- Sustainable and Compostable

- Wide variety of applications
- Additional applications limited by physical properties

Balks et al, Poly(lactic Acid): A Versatile Biobased Polymer for the Future with Multifunctional Properties from Monomer Synthesis, Polymerization Techniques and Molecular Weight Increase to PLA Applications, *polymers* **2021**, 13(11), 1822.

Hydrogen Peroxide Induced Degradation of Poly(Lactic Acid)   PAGE 2

UNIVERSITY OF WATERLOO

Slide 3

Project Overview

- PLA mixed with varied concentrations of hydrogen peroxide and processed at 250 °C for varied amounts of time
- Characterization of degraded material
  - Rheology (MFI, Parallel plate/capillary)
  - Gel Permeation Chromatography
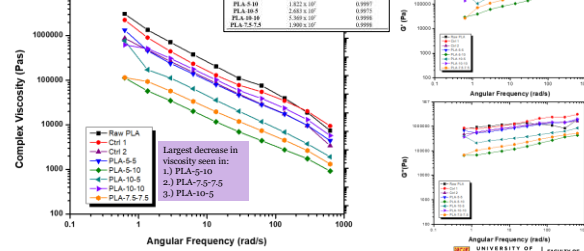 - Spectroscopy (FTIR/H-nmr)

Sample ID	H_2O_2 concentration (phr)	Process time (min)
PLA	This is only pure PLA L105 without processing	
Ctrl 1	0	10
Ctrl 2	10 phr of Water (H_2O)	10
PLA-5-5	5	5
PLA-5-10	5	10
PLA-10-5	10	5
PLA-10-10	10	10
PLA-7.5-7.5	7.5	7.5

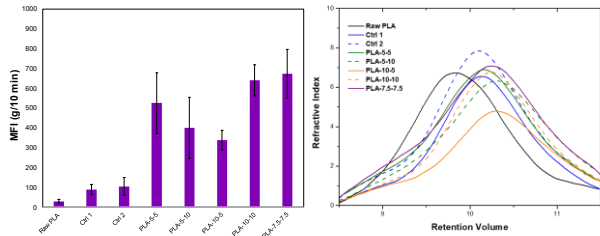Hydrogen Peroxide Induced Degradation of Poly(Lactic Acid)   PAGE 3

UNIVERSITY OF WATERLOO | FACULTY OF ENGINEERING

Slide 4

Results – Parallel Plate

Largest decrease in viscosity seen in:
1.) PLA-5-10
2.) PLA-7.5-7.5
3.) PLA-10-5

Hydrogen Peroxide Induced Degradation of Poly(Lactic Acid)   PAGE 4

UNIVERSITY OF WATERLOO | FACULTY OF ENGINEERING

Slide 5

Results – MFI and GPC

Hydrogen Peroxide Induced Degradation of Poly(Lactic Acid)   PAGE 5

UNIVERSITY OF WATERLOO | FACULTY OF ENGINEERING

Slide 6

Conclusions

- Hydrogen peroxide shows clear potential for lowering viscosity and molecular weight of PLA
- Increased melt flow of material expands the applications available
- Next step is to investigate application in melt blown filter media

Thank you!

Questions?
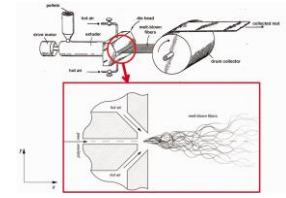
Kara and Molnár, A review of processing strategies to generate melt -blown nano/microfiber mats for high -efficiency filtration applications, *Journal of Industrial Textiles* **2022**, 51(1_suppl), 137S-180S.

Hydrogen Peroxide Induced Degradation of Poly(Lactic Acid)   PAGE 6

UNIVERSITY OF WATERLOO | FACULTY OF ENGINEERING

AKLIU GENET MESSELE
Chemical Engineering
Waterloo

Development of Multi-Filler Nanocomposites for Application of X-Ray Shielding

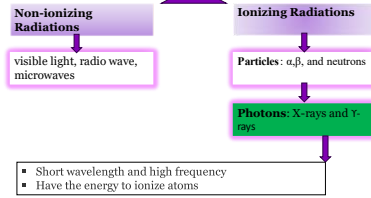# DEVELOPMENT OF MULTI-FILLER NANOCOMPOSITES FOR APPLICATION OF X-RAY SHIELDING

Aklilu Getnet Messele

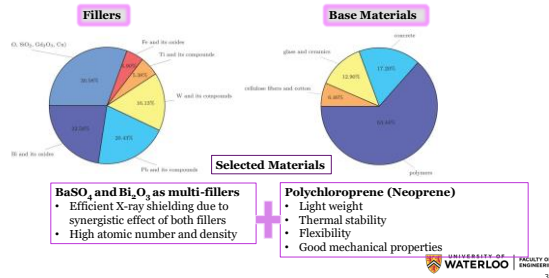Supervised by Professor Tizazu Mekonnen

May 2024

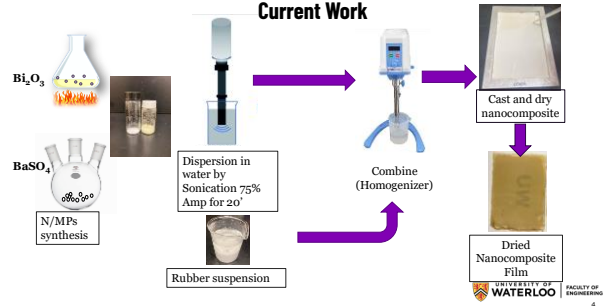UNIVERSITY OF WATERLOO | FACULTY OF ENGINEERING

1

Background

Radiation

Non-ionizing Radiations

visible light, radio wave, microwaves

Ionizing Radiations

Particles: α,β, and neutrons

Photons: X-rays and γ-rays

- Short wavelength and high frequency
- Have the energy to ionize atoms

UNIVERSITY OF WATERLOO | FACULTY OF ENGINEERING

2

Materials

Fillers

Base Materials

Selected Materials

BaSO$_4$ and Bi$_2$O$_3$ as multi-fillers
- Efficient X-ray shielding due to synergistic effect of both fillers
- High atomic number and density

Polychloroprene (Neoprene)
- Light weight
- Thermal stability
- Flexibility
- Good mechanical properties

UNIVERSITY OF WATERLOO | FACULTY OF ENGINEERING

3

Current Work

Bi$_2$O$_3$

BaSO$_4$

N/MPs synthesis

Dispersion in water by Sonication 75% Amp for 20'

Rubber suspension

Combine (Homogenizer)

Cast and dry nanocomposite

Dried Nanocomposite Film

UNIVERSITY OF WATERLOO | FACULTY OF ENGINEERING

4

Results

Film Morphology(SEM), dispersion(EDX) and Mechanical properties

-Cross-sectional view
-Good dispersion of BaSO4 NPs
-Settlement of Bi2O3 microrods due to high density and size
-increase in storage modulus loading of filler increase

Bi

Ba

Storage Modulus (Mpa) vs Temperature (C)
PCP
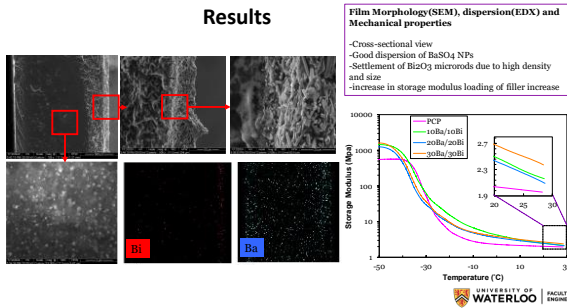10Ba/10Bi
20Ba/20Bi
30Ba/30Bi

UNIVERSITY OF WATERLOO | FACULTY OF ENGINEERING

5

Future Work

- Improving Bi2O3 dispersion
- Perform the x-ray shielding tests
- Comparing the results with Phy-X simulation results
- Multi-layering

Conclusion

- Good dispersion of BaSO4 NPs
- Dispersion of Bi2O3 needs improvement
- An increase in storage modulus

UNIVERSITY OF WATERLOO | FACULTY OF ENGINEERING

6

ETHAN CRAWFORD
Chemical Engineering
Waterloo

Melt-Blown Fibers for Oil Spill Remediation and Oil Barrier Geotextiles

Slide 1

MELT-BLOWN FIBERS FOR OIL SPILL REMEDIATION AND OIL BARRIER GEOTEXTILES

Ethan Crawford,

Supervised by Professor Tizazu Mekonnen

May 2024

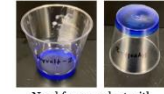UNIVERSITY OF WATERLOO | FACULTY OF ENGINEERING
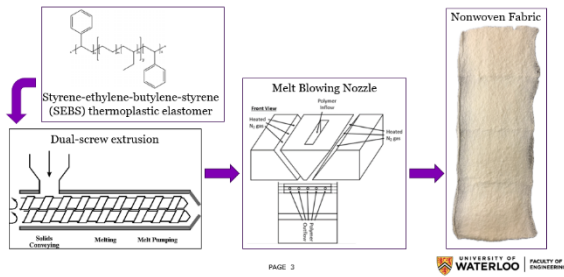
Slide 2

Background

Oil spills pose a danger to the environment

Current textile solutions suffer from leakage and sorption limits

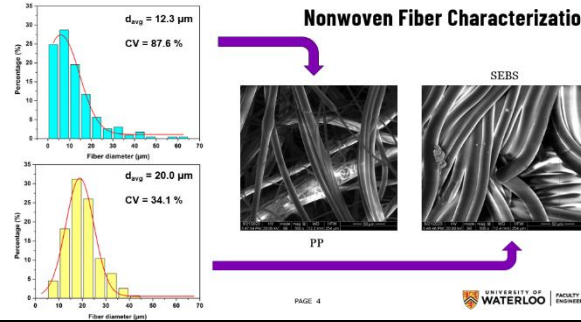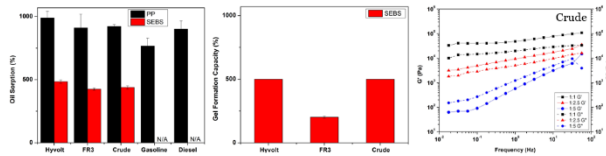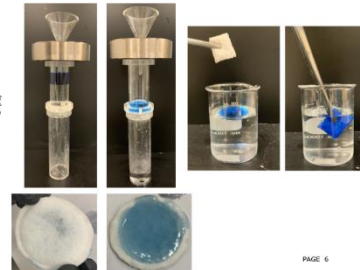Need for a product with superior oil immobilization

PAGE 2

UNIVERSITY OF WATERLOO | FACULTY OF ENGINEERING

Slide 3

Melt Blown Extrusion Processing

Styrene-ethylene-butylene-styrene (SEBS) thermoplastic elastomer

Dual-screw extrusion

Melt Blowing Nozzle

Nonwoven Fabric

PAGE 3

UNIVERSITY OF WATERLOO | FACULTY OF ENGINEERING

Slide 4

Nonwoven Fiber Characterization

d_{avg} = 12.3 µm

CV = 87.6 %

d_{avg} = 20.0 µm

CV = 34.1 %

SEBS

PP

PAGE 4

UNIVERSITY OF WATERLOO | FACULTY OF ENGINEERING

Slide 5

Oil Interaction

Crude

PAGE 5

UNIVERSITY OF WATERLOO | FACULTY OF ENGINEERING

Slide 6

Oil Cleanup and Barrier Demonstration

Future Work

- Increase Compatibility with more types of oil
- Further optimize processing conditions
- Explore other SEBS enabled oil remediation methods

PAGE 6

UNIVERSITY OF WATERLOO | FACULTY OF ENGINEERING

RYAN LLOYD
Chemistry
Waterloo

Studying the Interactions Between DNA and Cationic Surfactants by Pyrene Excimer Fluorescence and Dynamic Light Scattering

Studying the Interactions Between DNA and Cationic Surfactants by Pyrene Excimer Fluorescence and Dynamic Light Scattering

Ryan Lloyd and Jean Duhamel

Institute for Polymer Research, Waterloo Institute for Nanotechnology, Department of Chemistry, University of Waterloo, ON, N2L 3G1, Canada

INTRODUCTION

Gemini surfactants (GS) have attracted research interest due to their potential use in a variety of applications, such as in oil recovery and as vectors for drug loading and release.[1] One important research application however is their use as potential gene transfection agents for gene delivery.[2,3] In this context, a significant challenge in the field of gene therapy is the successful delivery of therapeutic genes to the desired cell.[3] Successful delivery of the genetic cargo to the desired cell requires an effective delivery vector, that can efficiently interact with the cell membrane.[4] These desirable membrane interactions were made possible by modifying the chemical structure of cationic gemini surfactants (CGS). Past studies have shown that CGS can form high and low order structures to efficiently interact with endosomal and model membranes.[4] The versatility of gemini surfactants in generating a variety of aggregate types is due to the modularity of their chemical structure composed of building blocks (spacer, head groups, hydrophobe), that can be easily modified. The length and structure of the alkyl tails, as well as the length and nature of the alkyl spacer can all be optimized to maximize transfection efficiency.[2,3] Adjustment in these molecular parameters can lead to more efficient delivery vectors for gene therapy, and analytical tools are required to assess the effectiveness of a given change in the molecular structure of a surfactant to improve delivery efficiency. In this context, molecular level information about the lipoplexes formed between DNA and cationic surfactants can be obtained through the analysis of the fluorescence spectra and decays acquired with the pyrene-labeled cationic gemini surfactant PyO-3-12 embedded in a lipoplex (Figure 1). These experiments take advantage of the ability of the dye pyrene to form an excimer upon encounter between an excited and a ground-state pyrene and the fact that the process of pyrene excimer formation (PEF) depends on the local pyrene concentration in the lipoplexes.[5]
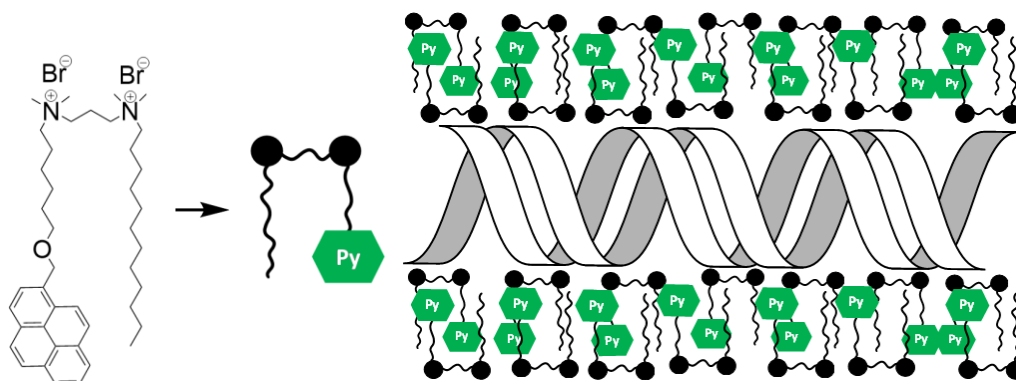

Figure 1. Molecular structure of PyO-3-12 (left). Schematic representation of the electrostatic interactions between PyO-3-12 and DNA leading to intermolecular pyrene excimer fluorescence (right).

The fluorophore pyrene is widely used to characterize macromolecules due to its long lifetime, high quantum yield, and especially for its ability to form excimer.[6] When PEF occurs within and/or among pyrene-labeled macromolecules, a pyrenyl label is found in one of three states.[6] Upon absorption of a photon, an excited pyrenyl label can be either isolated ($Py_{free}*$) in a pyrene-poor domain of the macromolecule, where it emits with the lifetime τ_M of the pyrene monomer, or it can form an excimer either upon diffusive encounter with a ground-state pyrene ($Py_{diff}*$) or via direct excitation of a pyrene aggregate ($Py_{agg}*$).[6]

Past research has used a pyrene-labeled surfactant to study its interactions with DNA.[7] While these earlier studies used an alkyl spacer to link pyrene to the surfactant, introduction of a heteroatom such as oxygen in the position beta-to-pyrene, as was done with the surfactant PyO-3-12 (see Figure 1), enables the pyrenyl label to sense the polarity of its local environment. This is achieved by monitoring its I_1/I_3 ratio, which represents the ratio of the fluorescence intensity of the first peak (I_1) over that of the third peak (I_3) in the steady-state fluorescence spectrum of the pyrene monomer.[6] The transition corresponding to the first fluorescence band (I_1), which is also the 0-0 transition for pyrene, is relatively weak in apolar solvents, to the point that it is described as symmetry forbidden in numerous publications, but is significantly stronger in more polar solvents, which explains the sensitivity of the I_1/I_3 ratio to solvent polarity, taking a value of 0.58 in hexane or 1.87 in water.[5]

Studies utilizing methods based on pyrene excimer fluorescence typically employ two major techniques. The first technique is steady-state fluorescence, which involves the acquisition of an emission spectrum ranging from 350 to 600 nm. The areas under the fluorescence spectrum corresponding to the regions of emission for the pyrene monomer (I_M) and pyrene excimer (I_E) can be used to calculate the I_E/I_M ratio, which can be related to several parameters pertaining to the system under study according to Equation 1.[6]

$$\langle k \rangle = k_{diff} \times [Py]_{loc} \propto \frac{I_E}{I_M} \tag{1}$$

The I_E/I_M ratio is proportional to the average rate constant for PEF, which is equal to the product of the bimolecular rate constant k_{diff} for PEF times the local concentration $[Py]_{loc}$ of ground-state pyrene. k_{diff} in Equation 1 reflects the internal dynamics of a system such as those experienced by the surfactant PyO-3-12 bound to DNA as it forms excimer (see Figure 1).[9] Due to the permanent positive charges of PyO-3-12, addition of DNA to a dilute PyO-3-12 aqueous solution results in the association of PyO-3-12 with DNA. In the process, PyO-3-12 is transferred from the polar aqueous solution to the hydrophobic environment of the PyO-3-12 aggregates bound to DNA, where it is concentrated and forms excimer.[7] Consequently, the dilute PyO-3-12 aqueous solution yields a low I_E/I_M ratio since $[Py]_{loc}$ is low in Equation 1 and a large I_1/I_3 ratio characteristic of pyrene in polar water. Upon complexation with DNA, microdomains of PyO-3-12 bound to DNA are formed even though the PyO-3-12 concentration remains low, resulting in a large I_E/I_M ratio since $[Py]_{loc}$ is large inside the PyO-3-12 aggregates bound to DNA and I_1/I_3 takes a lower value characteristic of the more hydrophobic environment of the PyO-3-12 aggregates.

The second major technique used to characterize pyrene excimer fluorescence is time-resolved fluorescence which involves the acquisition of the fluorescence decays for both the pyrene monomer and excimer. Both are obtained using cutoff filters of 370 and 470 nm, respectively, to reduce stray light from reaching the detector. The pyrene monomer and excimer fluorescence decays are then fitted according to the model free analysis (MFA) which uses sums of exponentials. The parameters retrieved from the MFA of the fluorescence decays yield the average rate constant <k> for PEF and the molar fractions f_{diff}, f_{free}, and f_{agg} of the pyrene species

$Py_{diff}*$, $Py_{free}*$, and $Py_{agg}*$, respectively. These parameters enable one to characterize the state of the pyrene species through the molar fractions f_{diff}, f_{free}, and f_{agg} and the dynamics experienced by the medium where the pyrenyl labels are embedded through $<k>$. These features make the combined use of PEF and MFA a powerful analytical tool to study colloidal systems in water by enabling the study at the molecular level of the interactions between polymers and surfactants in solution.

In the present study, the formation of aggregates between PyO-3-12 and DNA were characterized at the molecular and macromolecular level by fluorescence and dynamic light scattering (DLS), respectively. The formation of PyO-3-12/DNA aggregates led to a sharp increase in the local concentration of pyrenyl labels, a change toward a less polar environment being felt by pyrene, and a switch in ζ-potential from +15 to -50 mV upon binding of PyO-3-12 to DNA. The stability of the PyO-3-12/DNA complexes was investigated by adding sodium dodecyl sulfate (SDS) to a 1.5:1.0 DNA:PyO-3-12 mixture. The fluorescence and scattering techniques were able to follow the behavior of the PyO-3-12/DNA complexes as they interacted with SDS by forming ter-complexes until the DNA was freed from PyO-3-12, which was associated with SDS forming PyO-3-12/SDS mixed micelles. This study demonstrates that PyO-3-12 is a reliable fluorescent probe to study the interactions between DNA and surfactants at the molecular level.

EXPERIMENTAL

Chemicals: Deoxyribonucleic acid from calf thymus (CT-DNA) and sodium dodecyl sulphate (SDS) were purchased from Sigma-Aldrich. Doubly distilled deionized water from Millipore Milli-RO 10 Plus and Milli-Q UF Plus (Bedford, MA) was used to prepare all aqueous solutions.

Solution preparation: A 56 μM PyO-3-12 solution, below the CMC of PyO-3-12 equal to 0.38 mM, was used in all fluorescence experiments. The (−/+) ratio represented the concentration ratio of DNA base pairs over PyO-3-12, keeping in mind that one DNA base pair and one PyO-3-12 molecule have two negative and two positive charges, respectively. The (−/+) ratio was used to express the relative concentration of DNA with respect to the PyO-3-12 concentration. A solution of the desired (−/+) ratio was obtained by preparing two solutions, one with double the desired concentration of CT-DNA and the other with double the desired concentration of PyO-3-12. Mixing 2 mL of each solution produced a mixture of CT-DNA and PyO-3-12 of the desired (−/+) ratio. The solutions were left for at least one hour to reach equilibrium before being analyzed by dynamic light scattering, steady-state fluorescence, and time-resolved fluorescence.

Dynamic light scattering: The particle size distribution (PSD) and ζ potential were determined on a Malvern Zetasizer Nano ZS 90 with a He−Ne laser (633 nm) used to irradiate the solution which was kept at 25 ºC and whose scattering was detected at a 90° angle. The scattering data were analyzed with the Malvern Dispersion Technology Software 4.20. The ζ-potential was determined by measuring the electrophoretic mobility using the Smoluchowski approximation. Measurements were repeated 3 times to obtain the number average size and the ζ-potential for each sample.

Transmission Electron Microscopy: Samples were adhered to Formvar coated copper grids and allowed to dry for 2 minutes. Excess liquid was blotted away before the grid were stained with 1% (w/v) uranyl acetate. The grids were then observed using an FEI Tecnai G2 F20 transmission electron microscope operated at 200 kV and equipped with a bottom mount Gatan 4k CCD camera under standard operating conditions.

RESULTS AND DISCUSSION

The I_E/I_M and I_1/I_3 ratios retrieved from the analysis of the fluorescence spectra were plotted in Figure 2A as a function of the (–/+) ratio. The fluorescence spectra of PyO-3-12 showed little excimer being formed at low (–/+) ratios resulting in a low I_E/I_M ratio in Figure 2A. But as the (–/+) ratio approached unity, a rapid and dramatic increase in PEF and I_E/I_M was observed. Past the equicharge point, the excimer signal remained high, indicating strong PEF, although a small decrease of I_E/I_M was observed with increasing (–/+) ratios. The significant increase in I_E/I_M observed at the equicharge point confirms the binding of PyO-3-12 to CT-DNA, since the 56 μM PyO-3-12 concentration was below the 0.38 mM CMC of PyO-3-12. Since PyO-3-12 could not micellize in solution, excimer formation between PyO-3-12 surfactants could only occur if PyO-3-12 formed aggregates with CT-DNA.
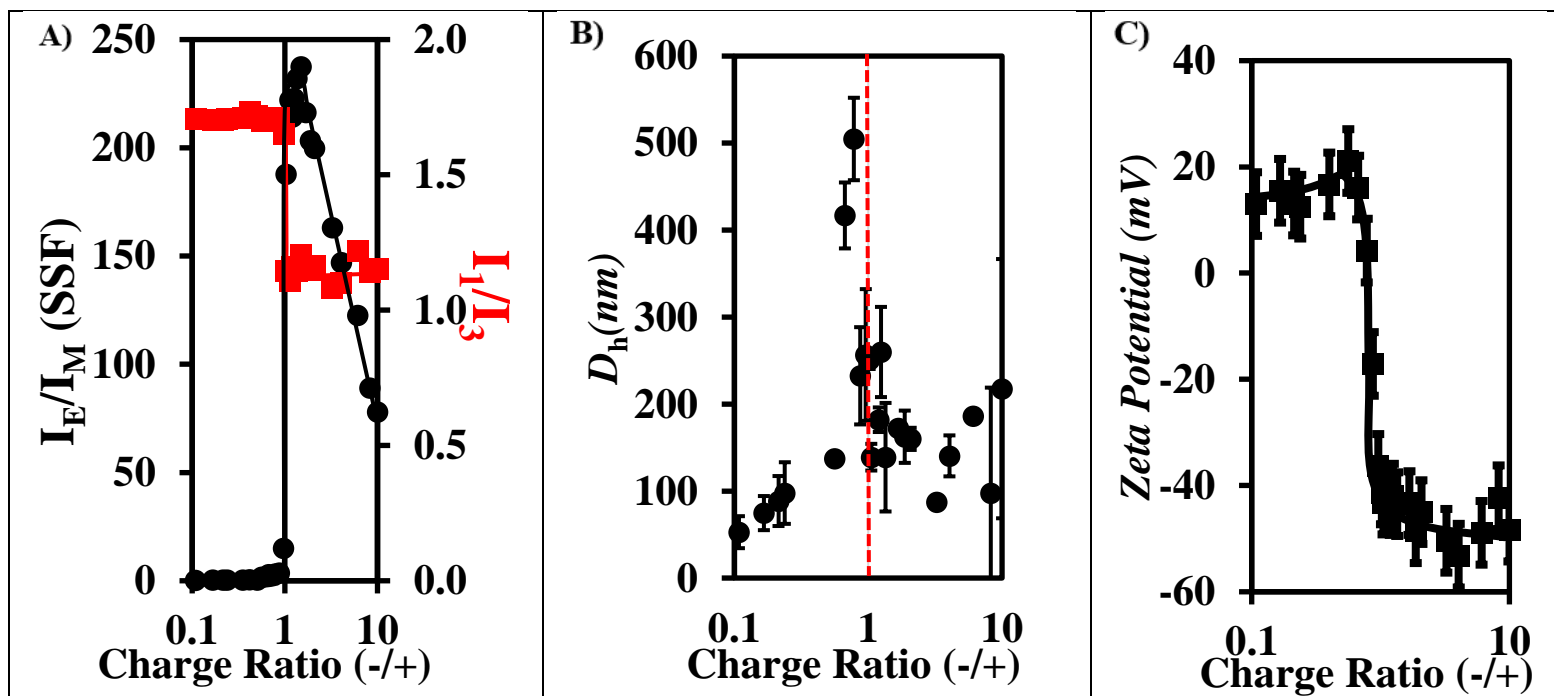

Figure 2. Plot of A) the I_1/I_3 and I_E/I_M ratios, B) the number average hydrodynamic diameter (D_h), and C) the ζ-potential for a 56 μM PyO-3-12 aqueous solution as a function of the CT-DNA concentration.

Another spectroscopic feature of PyO-3-12 is its sensitivity to the polarity of its local environment through the I_1/I_3 ratio. I_1/I_3 was plotted in Figure 2C as a function of the (–/+) ratio. For (–/+) ratios lower than the equicharge point, I_1/I_3 remained constant and equal to 1.72 (±0.01), close to the I_1/I_3 ratio of 1.73 reported for PyO-3-12 in water. However, the I_1/I_3 ratio showed a significant and sudden drop at the equicharge point, above which it equaled 1.27 (±0.02) for (–/+) ratios greater than 1.0.[8] The I_1/I_3 ratio found for the PyO-3-12/CT-DNA complexes suggests that PyO-3-12 experiences a less polar environment than that experienced by PyO-3-12 in water, confirming that PyO-3-12 self-assembled into PyO-3-12 aggregates upon binding onto CT-DNA.[8]

A similar trend is observed for the ζ-potential of solutions containing 56 μM PyO-3-12 as the CT-DNA concentration was increased in Figure 2C. Upon reaching the equicharge point, a

charge inversion occurs. While the ζ-potential remained positive and equal to +15.8 ($\pm$2.5) mV below the equicharge point, the ζ-potential turned negative and equal to -45 ($\pm$3) mV for ($-$/+) ratios above unity. The charge inversion was correlated to an increase in the number average hydrodynamic diameter (D_h) of the PyO-3-12/CT-DNA aggregates observed in Figure 2B. This increase in D_h at the equicharge point is reasonable since all charges are neutralized, which reduces the solubility of the species in solution leading to their aggregation into larger objects. As the CT-DNA concentration increases past the equicharge point, the PyO-3-12 molecules distribute themselves across a larger number of DNA strands and the PyO-3-12/CT-DNA aggregates are negatively charged and better stabilized by electrostatic repulsion, leading to a reduction in D_h. As the CT-DNA concentration increases much further from the equicharge point, the PyO-3-12/DNA aggregates are stabilized by the negatively charged DNA present in excess.

The stability of the PyO-3-12/DNA complexes was investigated by adding SDS to the complexes. To this end, the PyO-3-12/DNA aggregates were prepared with a constant ($-$/+) ratio of 1.5 to ensure that all PyO-3-12 was fully bound to the CT DNA. The plot of I_1/I_3 as a function of SDS concentration in Figure 3A indicates that with and without CT-DNA, I_1/I_3 remained constant and equal to, respectively, 1.22 ($\pm$0.02) and 1.72 ($\pm$0.01) prior to the equicharge point between PyO-3-12 and SDS corresponding to an SDS concentration of 112 μM. These I_1/I_3 ratios matched those of 1.27 and 1.73 reported for PyO-3-12 in water with and without CT-DNA, respectively.[5] However, the I_1/I_3 ratio showed a significant and sudden drop at the equicharge point, above which it equaled 0.89 ($\pm$0.03) and 0.94 ($\pm$0.04) for samples with and without CT DNA, respectively. These low I_1/I_3 ratios indicate that PyO-3-12 is shielded from water and experiences a more hydrophobic environment than in the PyO-3-12/CT-DNA complexes and even inside PyO-3-12/SDS mixed micelles. This observation suggests that PyO-3-12 is located inside multilamellar vesicles probably formed between SDS and PyO-3-12, where the inner lamellae were less exposed to water resulting in the much lower I_1/I_3 ratios. As the SDS concentration was further increased, the I_1/I_3 ratio continuously increased up to 1.48 ($\pm$0.01) which matched the I_1/I_3 ratio of PyO-3-12 in SDS micelles. Although PyO-3-12 yielded a similar I_1/I_3 ratio for the samples with and without CT-DNA for SDS concentrations above 112 μM corresponding to the equicharge point between PyO-3-12 and SDS, the I_E/I_M ratio given in Figure 3B showed differences between 112 and 400 μM. These differences suggest that within this SDS concentration range, a *ter*-complex must be formed between PyO-3-12, SDS, and CT-DNA. Past 1 mM SDS, the good match found between the I_1/I_3 and I_E/I_M ratios implies that PyO-3-12 is no longer interacting with CT-DNA and forms primarily PyO-3-12/SDS mixed micelles. The release of CT-DNA was also confirmed by TEM images and by the drop in D_h observed at higher SDS concentrations in Figure 3C. The drop in D_h occurred above 8.0 mM SDS which is the CMC for SDS. Past the CMC, a small average D_h value of 1.5 ($\pm$0.5) nm was obtained in Figure 3A suggesting the formation of SDS micelles. Above the CMC, the formation of SDS micelles leads to the encapsulation of individual PyO-3-12 surfactants inside the SDS micelles resulting in their isolation and low I_E/I_M ratios in Figure 3B.
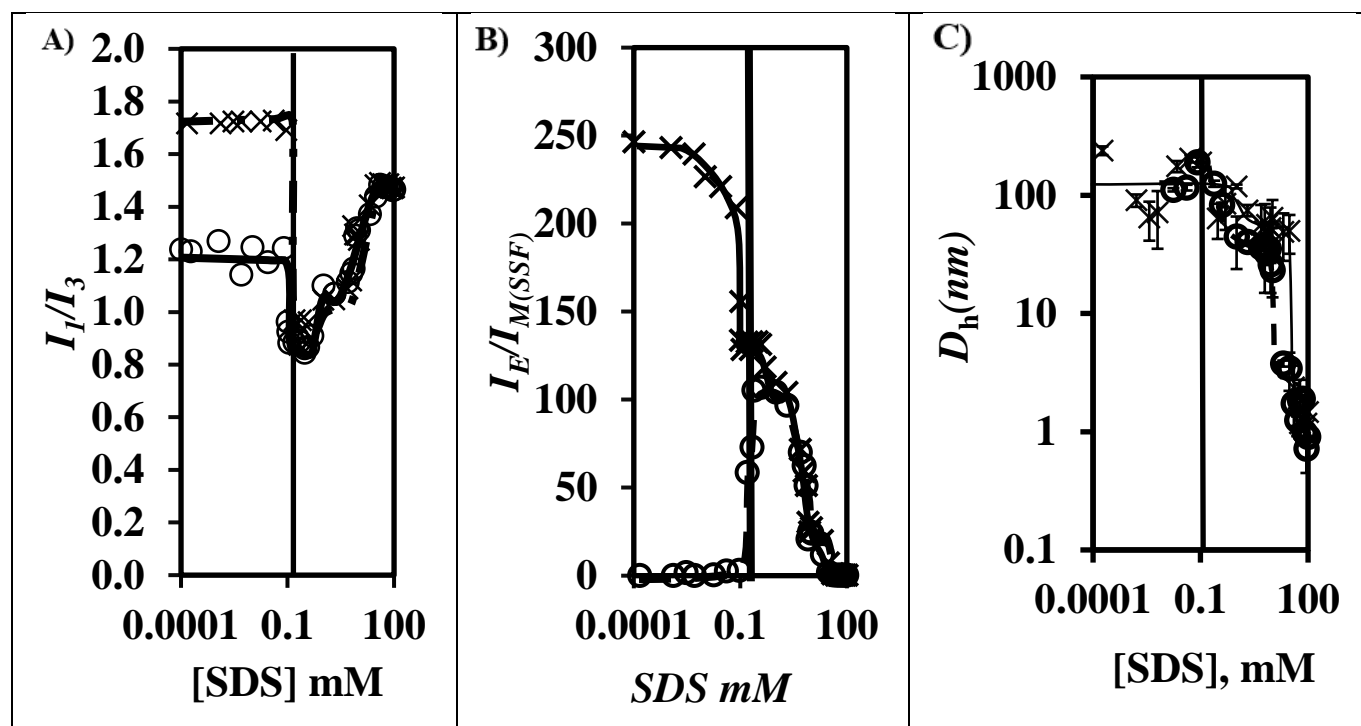
Figure 3. Plot of A) I_1/I_3, B) I_E/I_M, and C) the number average hydrodynamic diameter (D_h) for an aqueous solution of 56 µM PyO-3-12 and 84 µM CT-DNA as a function of SDS concentration for samples (crosses) with and (hollow circles) without DNA.

CONCLUSIONS

The interactions between PyO-3-12 and CT-DNA were characterized by using fluorescence, scattering, and TEM experiments. Fluorescence probes the environment of PyO-3-12 at the molecular level over a ~ 4 nm length scale, much smaller than the overall dimension of the PyO-3-12/CT-DNA complexes, which was found to be around 150 nm by DLS. The morphology of the PyO-3-12/CT-DNA complexes could be visualized by TEM. PyO-3-12 was found to form complexes with CT-DNA and the PyO-3-12/CT-DNA complexes could be disrupted by adding negatively charged SDS. The trends observed in this report matched those obtained earlier at a lower PyO-3-12 concentration of 16 µM indicating that while complex, these trends reflect the interactions taking place between PyO-3-12, CT-DNA, and SDS. Worth noting is the poor performance of DLS at the low 16 µM PyO-3-12 concentration which did not generate sufficient scattering. Similarly, the larger concentration of salt generated by the experiments conducted with 56 µM PyO-3-12 led to blurry TEM pictures. In contrast, the fluorescence experiments provided reliable results at both PyO-3-12 concentrations. The combination of fluorescence, DLS, and TEM provided a detailed description of the PyO-3-12/CT-DNA complexes and their interactions with SDS. Since the complexation of polynucleotides such as DNA or RNA with oppositely charged surfactants has found interest for gene delivery or RNA vaccines, PyO-3-12 appears to be a valuable probe to study these complexes at the molecular level.

32

REFERENCES

1. Wettig, S.; Verrall, R.; Foldvari, M. Gemini Surfactants: A New Family of Building Blocks for Non-Viral Gene Delivery Systems. *Curr Gene Therapy* **2008**, *8*, 9–23.
2. Kirby, A.J.; Camilleri, P. Gemini surfactants: New synthetic vectors for gene transfection. *Angew. Chem. Int. Ed.* 2003, *42*,1448–1457.
3. Ren, S.; Wang, M.; Wang, C.; Wang, Y.; Sun, C.; Zheng, Z.; Cui, H.; Zhao, X. Application of Non-Viral Vectors in Drug Delivery and Gene Therapy. *Polymers* **2021**, *13*, 3307-3316.
4. Bell, P. C.; Bergsma, M.; Dolbnya, I. P.; Bras, W.; Stuart, M. C. A.; Rowan, A. E.; Feiters M. C.; Engberts J. B. F. N. Transfection Mediated by Gemini Surfactants: Engineered Escape from the Endosomal Compartment. *J. Am. Chem. Soc.* **2003**, *125*, 1551−1558.
5. Ba Salem, A. Probing the Interactions between Pyrene-labelled Gemini Surfactants and DNA by Fluorescence. PhD thesis at UW, 2022
6. Duhamel, J. Global Analysis of Fluorescence Decays to Probe the Internal Dynamics of Fluorescently Labeled Macromolecules. *Langmuir* **2014**, *30*, 2307-2324.
7. Ba-Salem, A. O.; Duhamel, J. Synthesis and Characterization of a Pyrene-Labeled Gemini Surfactant Sensitive to the Polarity of Its Environment. *Langmuir* **2021**, *37*, 13824–13837.
8. Ba-Salem, A.; Gong, R.; Duhamel, J. Characterization of the Interactions between a Cationic Pyrene-Labeled Gemini Surfactant, and the Anionic Surfactant Sodium Dodecyl Sulfate. *Langmuir* **2022**, *38*, 7484-7495.
9. Little, H.; Patel, S.; Duhamel, J. Probing the Inner Local Density of Complex Macromolecules by Pyrene Excimer Formation. *Phys. Chem. Chem. Phys.* **2023**, *25*, 26515-26525.

DEBELA TADELE
Chemical Engineering
Waterloo

Co-Encapsulation of Quercetin and α-Tocopherol Bioactives in Zein Nanoparticles: Synergistic Interactions, Stability, and Controlled Release

Co-encapsulation of Quercetin and α-Tocopherol bioactives in Zein Nanoparticles: Synergistic interactions, stability, and controlled release

Debela T. Tadele, Tizazu H. Mekonnen

Institute of Polymer Research, Waterloo Institute of Nanotechnology, University of Waterloo, Waterloo, ON, N2L 3G1, Canada

Abstract

Chronic diseases, such as cancer, diabetes, and cardiovascular and respiratory conditions, currently account for approximately 71% of the global death rates[1]. The increasing prevalence of chronic diseases has generated heightened interest in nutraceuticals and functional food ingredients, which are believed to offer health benefits beyond basic nutrition and may aid in the prevention and management of various health conditions[2,3]. Nutraceuticals, particularly bioactive compounds such as quercetin and α-tocopherol, have emerged as potent agents owing to their antioxidant, antimicrobial, and anti-inflammatory properties[4–8]. However, their clinical efficacy is hampered by their poor solubility and bioavailability[5,8]. This study introduces a novel co-encapsulation approach using zein nanoparticles to address these challenges with the aim of enhancing the therapeutic potential of quercetin and α-tocopherol through improved delivery and stability.

We employed an antisolvent co-precipitation technique to fabricate zein nanoparticles for the co-encapsulation of quercetin and α-tocopherol. This process involves optimizing the nanoparticle formulation to achieve an ideal particle size and high encapsulation efficiency. We utilized various characterization techniques, such as dynamic light scattering for particle sizing, scanning electron microscopy (SEM), transmission electron microscopy (TEM) for morphological analysis, and in vitro gastrointestinal digestion studies to evaluate the release profiles.

The Zein/Que/Toc nanoparticles exhibited optimal encapsulation efficiency, characterized by a controlled and sustained release of both quercetin and α-tocopherol over an 8-hour period, indicating a synergistic interaction. Scanning electron microscopy (SEM) and transmission electron microscopy (TEM) images revealed a uniform particle distribution with no significant aggregation, confirming the effectiveness of the method. In vitro digestion studies further highlighted the stability and bioavailability of the encapsulated bioactive compounds, suggesting the potential of NPs to enhance the therapeutic effects of quercetin and α-tocopherol. These findings highlight the potential of zein-based nanoparticles as a versatile platform for the co-delivery of nutraceuticals. The co-encapsulation of quercetin and α-tocopherol overcomes the solubility and bioavailability challenges and leverages their synergistic properties to enhance therapeutic efficacy, as illustrated in Fig. 1. This approach holds significant promise for the development of functional foods and nutraceutical products for chronic disease management and prevention.
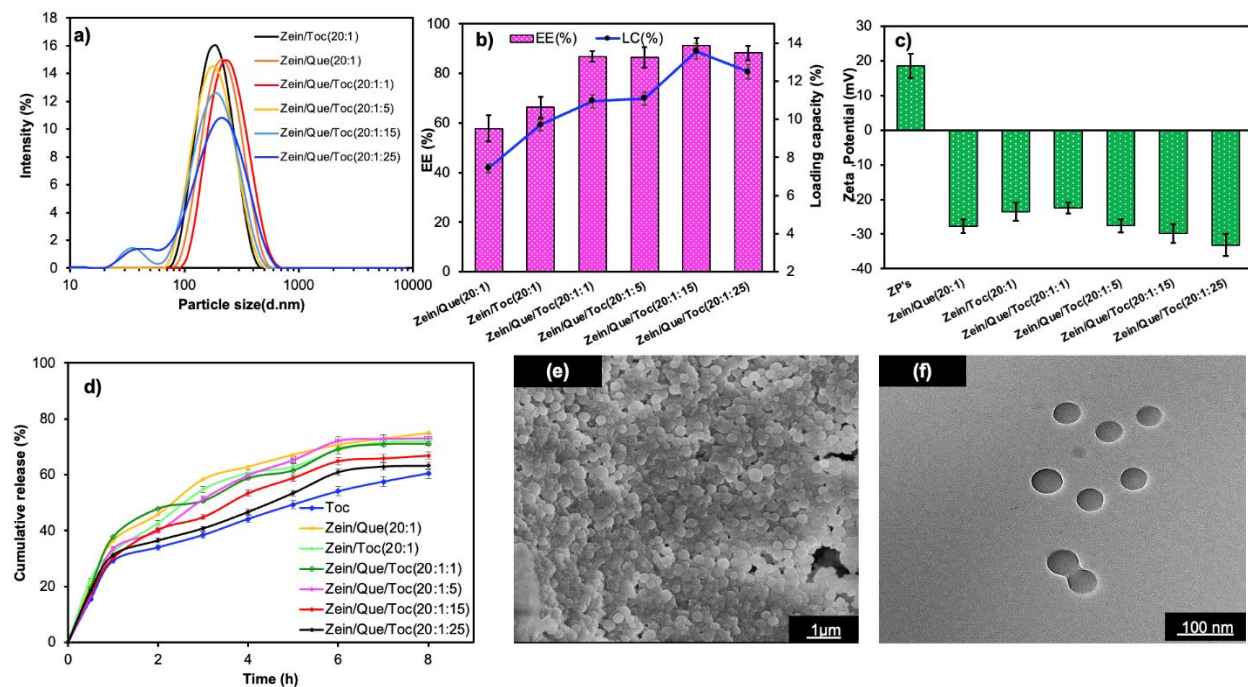
Figure 1: Comprehensive Characterization of Zein/Que/Toc Nanoparticles. (a) Particle Size Distribution ranging from 50 nm to 320 nm. (b) Encapsulation Efficiency of up to 96%. (c) Zeta Potential indicating the surface charge and colloidal stability. (d) Control Release Profile, demonstrating sustained release over 8h . (e) SEM and (f) TEM images of surface morphology and internal structure, respectively.

Reference:

1.   WHO. (2018). Noncommunicable diseases. https://www.who.int/news-room/fact-sheets /detail/noncommunicable-diseases.

2.   Daliu, P., Santini, A. & Novellino, E. From pharmaceuticals to nutraceuticals: bridging disease prevention and management. *Expert Rev Clin Pharmacol* **12**, (2019).

3.   Bergamin, A. *et al.* Nutraceuticals: Reviewing their Role in Chronic Disease Prevention and Management. *Pharmaceutical Medicine* vol. 33 Preprint at https://doi.org/10.1007/s40290-019-00289-w (2019).

4.   Rodríguez-Félix, F. *et al.* Preparation and Characterization of Quercetin-Loaded Zein Nanoparticles by Electrospraying and Study of In Vitro Bioavailability. *J Food Sci* **84**, (2019).

5.   Zhang, Z. *et al.* Physicochemical stability, antioxidant activity, and antimicrobial activity of quercetin-loaded zein nanoparticles coated with dextrin-modified anionic polysaccharides. *Food Chem* **415**, (2023).

6.   Ye, F., Astete, C. E. & Sabliov, C. M. Entrapment and delivery of α-tocopherol by a self-assembled, alginate-conjugated prodrug nanostructure. *Food Hydrocoll* **72**, 62–72 (2017).

7.   Zhang, L., Liu, Z., Sun, Y., Wang, X. & Li, L. Effect of α-tocopherol antioxidant on rheological and physicochemical properties of chitosan/zein edible films. *LWT* **118**, (2020).

8.   Zhang, F., Khan, M. A., Cheng, H. & Liang, L. Co-encapsulation of α-tocopherol and resveratrol within zein nanoparticles: Impact on antioxidant activity and stability. *J Food Eng* **247**, 9–18 (2019).

PROF. ALEX PENLIDIS
Academic Speaker
IPR Member

Copolymerization Composition Control Policies: Batch, Semi-Batch, or Flow

ABSTRACT: Copolymerization Composition Control Policies: Batch, Semi-batch or Flow?

Presentation by Prof. Alexander Penlidis

Characteristics of three classes of copolymer composition control policies are presented and discussed with applications on several typical copolymer systems. The effects of these policies are shown on polymerization rate, copolymer composition, and molecular weight, branching and sequence length properties. Extensions to terpolymerizations (and hence, other multi-component polymerizations) are also modeled and presented. Generalized procedures for practical implementation and comparisons among policies are highlighted, along with some special cases.

	Alex Penlidis Biography: Professor Penlidis, Chemical Engineering, has had almost four decades of experience in Polymer Reaction Engineering (PRE), Polymer Reactor Optimization and Troubleshooting, and Mathematical Modelling. He has been the Director of the Institute for Polymer Research (IPR) from 1994-2010. After four decades in the area of polymerization, 400 refereed publications and the supervision of 35 PhD students, he is more confident that he can find his way around copolymerization aspects.

ALINE BRAZ RAMIREZ
Chemical Engineering
Waterloo

3D Printing of Soft-Gel with Bio-Derived Solvent for Biomedical Applications

3D printing of soft-gel with bio-derived solvent for biomedical applications

Ramirez, A. B; Bauman, L.; Zhao, B. [1]

04/01/2024

UNIVERSITY OF WATERLOO

1Surface Science and Bio-nanomaterials Laboratory, Waterloo Institute for Nanotechnology, Institute for Polymer Research, Centre for Bioengineering and Biotechnology, Department of Chemical Engineering,

---

Introduction

- Organogel that can overcome printing mechanical stress;
- Double Network Hydrogel of poly(HEA-co-SPA) and Quaternized Chitosan;
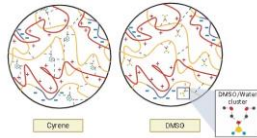- Solvent comparison of Dimethyl sulfoxide (DMSO) and Cyrene;
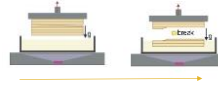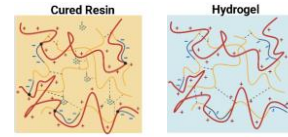
DMSO ❌	Cyrene ✅
Deep skin penetration and carrier	Biomass-derived, similar solubility properties

PAGE 2

UNIVERSITY OF WATERLOO


Solvent Comparison

Cyrene: More elastic, weaker
DMSO: Less elastic, stronger

Tensile Test

Max. Stress ~155 kPa
Max. Strain ~390%

Max. Stress ~58 kPa
Max. Strain ~650%

Compression Test

Max. Stress ~640 kPa
Max. Strain ~82%

Max. Stress ~410 kPa
Max. Strain ~93%

UNIVERSITY OF WATERLOO
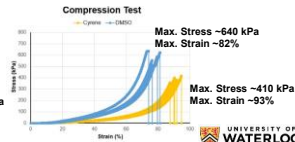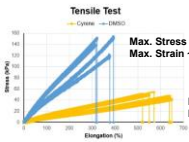
Hydrogel Characterization

Fatigue	Resistance to cyclic strain
Swelling	Volume increase of 4x
Dehydration	~86% water content
Adhesion	Low adhesion
Printability	Resolution of 0.05mm
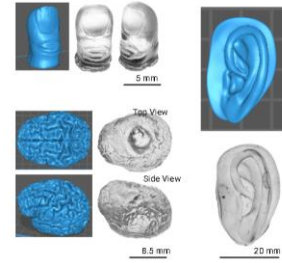
Proposed Biomedical Application

- Customized
- Higher effectiveness
- Bio-derived material

Patient & 3D scanning → 3D model analysis → 3D printing → Customized healthcare tools

---
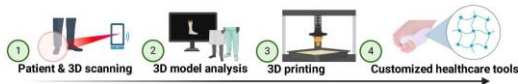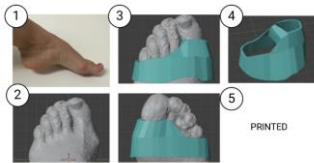
Conclusion and outlook

- Low toxicity
- Bio-derived material
- Remarkable printability
- Potential applicability as a Hallux Valgus toe separator

Outlook: Increase mechanical properties & perform cytotoxicity tests

Questions?
Thank you!

PAGE 6

UNIVERSITY OF WATERLOO

SHAKIBA SAMSAMI
Chemical Engineering
Waterloo

Chaotic 3D-Printing of Cellulose Nanocrystal-based Hydrogels for the Fabrication of Electromagnetic Shields

CHAOTIC 3D-PRINTING OF CELLULOSE NANOCRYSTAL -BASED HYDROGELS FOR THE FABRICATION OF ELECTROMAGNETIC SHIELDS

PRESENTER: SHAKIBA SAMSAMI
SUPERVISORS: PROF. TAM AND PROF. KAMKAR
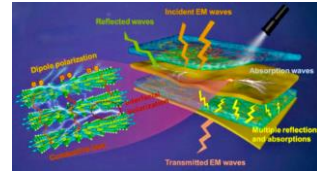
IPR SYMPOSIUM
MAY 1, 2024

UNIVERSITY OF WATERLOO | FACULTY OF ENGINEERING

Electromagnetic Interference (EMI) Shielding

Health Canada , safety code 6:
Limits of human exposure to electromagnetic fields

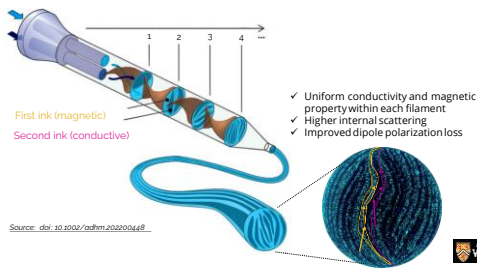Electromagnetic waves radiation
Source: Genengnews.com

EMI shielding mechanisms-
Source: doi: 10.1016/j.jjmst.2023.05.056

UNIVERSITY OF WATERLOO | FACULTY OF ENGINEERING

What is Chaotic Printing?

❖ Creating **multi -layered** filaments for printing

First ink (magnetic)

Second ink (conductive)

✓ Uniform conductivity and magnetic property within each filament
✓ Higher internal scattering
✓ Improved dipole polarization loss

Simulation | Experimental

The number of layers are dictated by the number of mixing elements

Source: doi: 10.1002/adhm.202200448

UNIVERSITY OF WATERLOO NMKR LAB

Multi-layered Filaments

Filament

CNC/PEDOT hydrogel

CNC/Fe3O4 hydrogel

Mixing elements
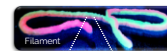
Cross -sectional view of the multi -layered filament by fluorescent microscopy

UNIVERSITY OF WATERLOO NMKR LAB

Printed Sample

o CNC gel
o Needle: 0.72 mm (19G)
o Flow rate: 1.5 mL/min

3D printed sample

3D printing setup
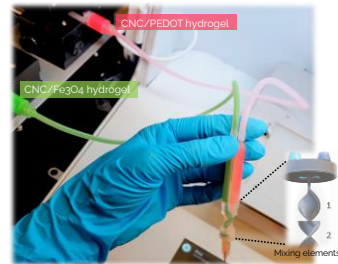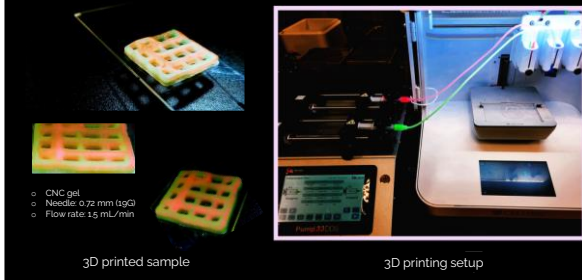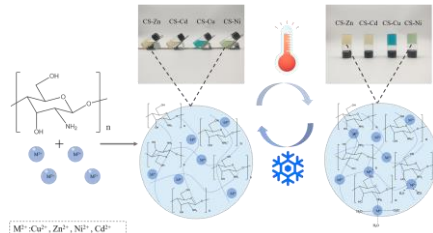

Thank you for your attention

SHIKUAN XU
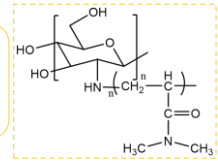Chemical Engineering
Waterloo

Chitosan Thermosensitive Hydrogel System

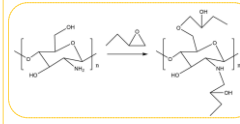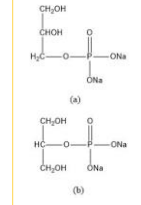# Chitosan thermosensitive hydrogel system

3/14/2024

Shikuan Xu

Supervisor : Michael Tam

s369xu@uwaterloo.ca

UNIVERSITY OF WATERLOO

M^{2+}:Cu^{2+}, Zn^{2+}, Ni^{2+}, Cd^{2+}

Chitosan thermosensitive hydrogel

1. β-Glycerophosphate system

2. Hydroxybutyl chitosan (HBC) system

3. Poly-N-isopropylacrylamide/chitosan system

PAGE 2

UNIVERSITY OF WATERLOO

Chitosan-metal ions thermosensitive hydrogel
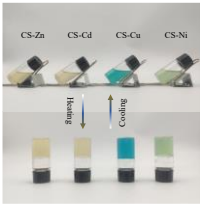
Multiple metal ions system

Gel temperature(℃)
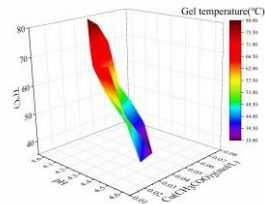
Controlled gel points

PAGE 3

UNIVERSITY OF WATERLOO

Chitosan-metal ions thermosensitive hydrogel

Simple and rapid preparation for **scale production**

PAGE 4

UNIVERSITY OF WATERLOO

Thank you!

PAGE 5

UNIVERSITY OF WATERLOO
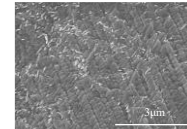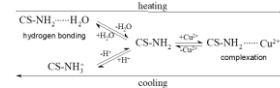
45

TOBECHUKWU OHAKA
Chemical Engineering
Waterloo

Designing Recyclable Natural Rubber – CNC Vitrimers

DESIGNING RECYCLABLE NATURAL RUBBER – CNC VITRIMERS

Tobechukwu Ohaka,
MASc Candidate, Chemical Engineering

UNIVERSITY OF WATERLOO | FACULTY OF ENGINEERING

Background

- Natural Rubber(NR) is a valuable bio-based elastomer
- To obtain desirable mechanical, chemical and thermal properties, natural rubber must undergo chemical processing and vulcanization
- Vulcanization creates permanent cross-linking networks
- This results in the loss of:
    - Recyclability
    - Biodegradability
- Dynamic crosslinking helps address the need to create sustainable natural rubber products
- Cellulose nanocrystals are high molecular weight bio-sourced materials produced from cellulose fibers

Image from: https://www.rubbernews.com/article/20190521/NEWS/190519986/global -platform-for-sustainable-natural-rubber-takes-shape

---

Previous Work

- Vitrimers have thermo-chemical bond exchange
- These polymer networks have an additional transition temperature (T_v)

  Thermoset $< T_v <$ Thermoplastic

- To create the dynamic covalent network, maleated NR was batch mixed with the epoxy DGEBA at varying molar ratios
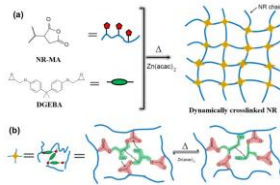

Image from: **Recyclable and Self-Healing Natural Rubber Vitrimers from Anhydride - Epoxy Exchangeable Covalent Bonds**
DOI: 10.1021/acsapm.3c00258

Previous Work

- NR Vitrimer was produced and confirmed using FTIR below and above T_v
- The optimal formulation was NR-MA-DGEBA 2 (1.5 mols DGEBA to 1 mol MA)
- Mechanical testing confirmed that the NR Vitrimer retained most of its mechanical properties even after 4 recycling stages
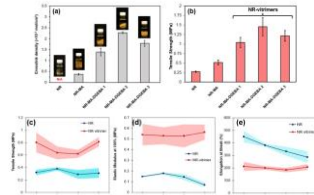
Image from: **Recyclable and Self-Healing Natural Rubber Vitrimers from Anhydride - Epoxy Exchangeable Covalent Bonds**
DOI: 10.1021/acsapm.3c00258

Current Work
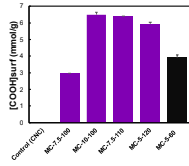
CNC Modification

Maleated nanocellulose crystals are being studied as an additive for the vitrimer

N = No initiator N = No initiator D = DCP N = No initiator A = A96
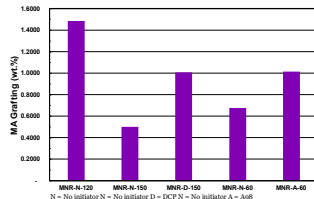
Optimization of NR Modification

The % grafting of MA is being optimized to increase the dynamic crosslinking and reduce the static crosslinking

---

UNIVERSITY OF WATERLOO

FACULTY OF ENGINEERING

Questions?

SABA KARIMI
Physics & Astronomy
Waterloo

Thermal Expansion Study on Polymer Stable Glasses

An Extended Abstract:
Thermal Expansion Study on Polymer Stable Glasses

Saba Karimi

Department of Physics and Astronomy, University of Waterloo, Waterloo, Ontario, Canada

Glass is an amorphous solid that is trapped in a non-equilibrium state [6], and plays an important role in our life[6]; Since the glass transition remains an unsolved problem despite decades of study, glassy state, and glass transition is called the "deepest and most interesting unsolved problem in solid-state theory" [3].

Recently there has been the discovery of making stable glasses in the lab with physical vapour deposition to have glass near to "ideal glass", the ground state that ordinary glasses are trying to reach by aging [8]. Aging is the slow evolution toward an ideal equilibrium state in the glasses that happened over thousands or even millions of years in nature [3], which is considered similar to "ideal glass" prepared in the limit of infinitely slow cooling to the Kauzmann temperature T_K [6, 8]. In the last decades, challenges to learn more about ideal glasses have led us to study stable glasses which has been an interesting area in this field. As mentioned above, these stable glasses are prepared by physical vapour deposition giving the ability to have a glass with high kinetic stability, high density, and low fictive temperature [8].

Polymers are interesting materials due to their behaviors and application in our life and studying them in different aspects is crucial. Since polymers easily avoid crystallization and their tunability in glass transition temperature, T_g, with changing the number of polymerizations, they are a great candidate for studying glasses. Although Making polymer-

stable glasses with physical vapour deposition is a challenge due to the thermal sensitivity of polymers, interesting research has been done[7, 12].

We focus on polymer-stable thin film glasses and their properties in different aspects. In this work, we are investigating the polymer stable glasses with a thermal expansion perspective. These studies include the rejuvenation, transforming from glass to supercooled by the propagation of front originating from the interface in thin-film that with the time of this transformation, we can estimate the relaxation time in supercooled liquid [8] and aging of the films for the slow evolution toward an ideal and investigating the thermal expansion gives us valuable information about glasses.

In our most recent work [7] we measured the depth-dependent local dynamics in thin polystyrene and PMMA films through the rejuvenation of ultrastable glasses with an Ellipsometer. Anomalous dynamics and glass transition temperatures in thin polymer films have been studied for 3 decades and continue to be an active research area. While it has long been noted that a measure of depth-dependent dynamics is the necessary measurement to develop our understanding, such measurements have been elusive. Direct measures of dynamics have been reported for the free surface region only, and low-resolution layer-by-layer measures of Tg remain the only report of depth dependence related to structural relaxation. We introduce a new technique that utilizes the front-mediated rejuvenation of recently discovered stable polymer glass to obtain a nm precision measure of relaxation in thin polymer films. This technique is used to measure depth-dependent relaxation in PS and PMMA. In both materials, an unexpected long-range relaxation process is observed in addition to the expected near-free surface enhancement of dynamics. We demonstrate that

the propagation of the front responsible for the transformation to a supercooled liquid state can serve as a highly localized probe of the local supercooled dynamics. We use this connection to probe the depth-dependent relaxation rate with nanometric precision for a series of polystyrene films over a range of temperatures near the bulk glass transition temperature. The analysis shows the spatial extent of enhanced surface mobility and reveals the existence of an unexpectedly large dynamical length scale in the system. The results are compared with the cooperative-string model for glassy dynamics. The data reveals that the film-thickness dependence of whole film properties arises only from the volume fraction of the near-surface region. While the dynamics in the middle of the samples show the expected bulk-like temperature dependence, the near-surface region shows very little temperature dependence. The part of results are illustrated in Figures 1,2,3.

The surface mobile layer in a glass has been directly linked to the ability to prepare these ultrastable glasses by vapour deposition [7, 4]. Upon heating, thin films of such materials rejuvenate to the normal supercooled liquid by the propagation of a transformation front originating from the free surface [2, 13] a situation reminiscent of many phase-transition fronts in physics, such as freezing fronts. The propagation velocity of that front has been correlated to the relaxation dynamics of the supercooled liquid [9]. This connection is usually of the form $v = C\tau_\alpha^{-\gamma}$, where v is the rejuvenation-front velocity, τ_α is the alpha relaxation time, and γ is an exponent in the range 0.8-1 [9]. Previous studies [5, 10] have modeled ellipsometric data to identify the position of the front as a function of time. Since the front is highly localized in space, the front-propagation rate should provide a precise measure of the local dynamics at each specific depth as the front moves from the free surface to the supporting substrate of the sample. In this work, we use the established mechanism of

rejuvenation by front propagation in thin films as well as the link between rejuvenation-front velocity and material relaxation properties to demonstrate that ellipsometric measurements of isothermal rejuvenation of ultrastable glasses can be used to probe the depth-dependent local dynamics of supercooled thin polymer films at temperatures near the dilatometric T_g with nanometric precision throughout the film. We compare the measurements with calculations based on the cooperative-string theory for supercooled dynamics in thin films. The results provide an independent and reasonably direct measure of the size of the surface region and reveal the existence of an intriguing long-range dynamical effect. In addition, the results indicate a very narrow range of temperatures above T_g where enhanced surface dynamics are observed.

Figure 2: Depth z of the rejuvenation front as a function of time t (solid line), for a PS film with a typical thickness of 90 nm, at a temperature T = 315.5 K. [7]
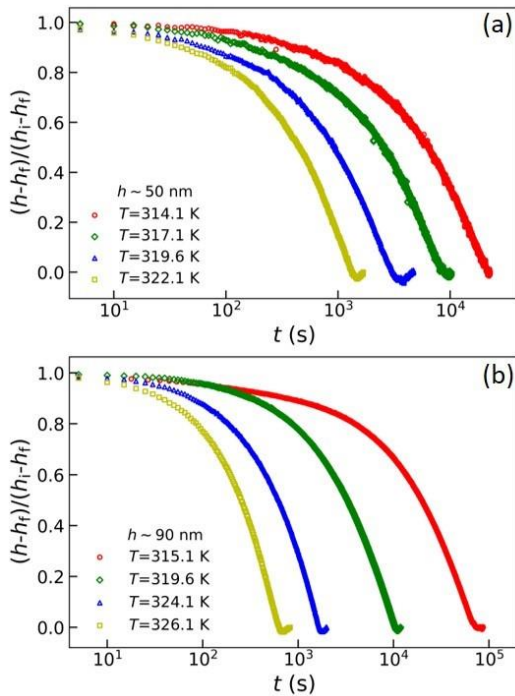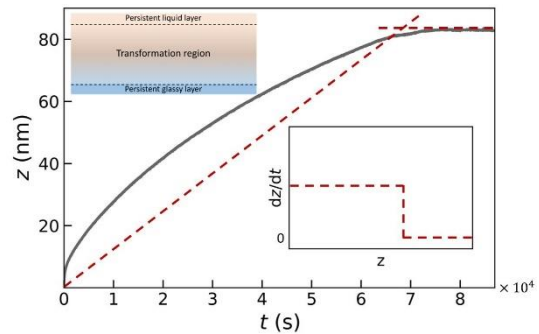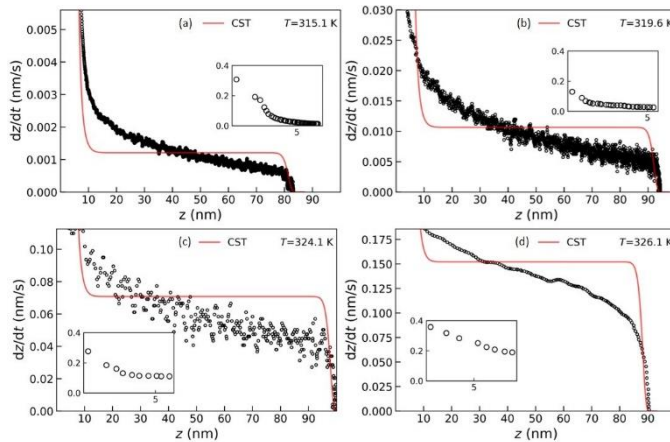
Figure 1: Total film thickness h, normalized using the initial and final values, h_i and h_f respectively, as a function of time t during isothermal rejuvenation [7]

Figure 3: Local rejuvenation-front velocity *dz/dt* as a function of front depth *z* from the position of the free surface, for various temperatures as indicated, as obtained from ellipsometric data. Insets provide zooms of the experimental data near the free surface. For comparison, predictions from the cooperative-string theory (CST) near interfaces [11, 1] are shown with solid lines [7]

References

[1] November 2022. [Online; accessed 15. Mar. 2024].

[2] Scholars@Duke publication: Front-Mediated Melting of Isotropic Ultrastable Glasses., March 2024. [Online; accessed 15. Mar. 2024].

[3] P. W. Anderson. Through the Glass Lightly. *Science*, 267(5204):1615–1616, March 1995.

[4] Ludovic Berthier, Patrick Charbonneau, Elijah Flenner, and Francesco Zamponi. Origin of Ultrastability in Vapor-Deposited Glasses. *Phys. Rev. Lett.*, 119(18):188002, November 2017.

[5] Shakeel S. Dalal, Zahra Fakhraai, and M. D. Ediger. High-Throughput Ellipsometric Characterization of Vapor-Deposited Indomethacin Glasses. *J. Phys. Chem. B*, 117(49):15415–15425, December 2013.

[6] M. D. Ediger, C. A. Angell, and Sidney R. Nagel. Supercooled Liquids and Glasses. *J. Phys. Chem.*, 100(31):13200–13212, January 1996.

[7] Saba Karimi, Junjie Yin, Thomas Salez, and James A. Forrest. Measurement of the depth-dependent local dynamics in thin polymer films through rejuvenation of ultrastable glasses. *arXiv*, December 2023.

[8] Adam N. Raegen, Junjie Yin, Qi Zhou, and James A. Forrest. Ultrastable monodisperse polymer glass formed by physical vapour deposition. *Nat. Mater.*, 19:1110–1113, October 2020.

[9] Cristian Rodriguez-Tinoco, Marta Gonzalez-Silveira, Miguel Angel Ramos, and Javier Rodriguez-Viejo. Ultrastable glasses: new perspectives for an old problem. *Riv. Nuovo Cimento*, 45(5):325–406, May 2022.

[10] Dalal S. S., Walters D. M., I. Lyubimov, De Pablo J. J., and Ediger M. D. Tunable molecular orientation and elevated thermal stability of vapor-deposited organic semiconductors. *Proc. Natl. Acad. Sci. U.S.A.*, 112(14):4227–4232, March 2015.

[11] Thomas Salez, Justin Salez, Kari Dalnoki-Veress, Elie Raphaël, and James A. Forrest. Cooperative strings and glassy interfaces. *Proc. Natl. Acad. Sci. U.S.A.*, 112(27):8227– 8231, July 2015.

[12] Stephen F. Swallen, Kenneth L. Kearns, Marie K. Mapes, Yong Seol Kim, Robert J. McMahon, M. D. Ediger, Tian Wu, Lian Yu, and Sushil Satija. Organic Glasses with Exceptional Thermodynamic and Kinetic Stability. *Science*, 315(5810):353–356, January 2007.

[13] Stephen F. Swallen, Katherine Traynor, Robert J. McMahon, M. D. Ediger, and Thomas E. Mates. Stable Glass Transformation to Supercooled Liquid via Surface-Initiated Growth Front. *Phys. Rev. Lett.*, 102(6):065503, February 2009.

HUNTER LITTLE
Chemistry
Waterloo

Probing the Local Density of Macromolecules by Fluorescence

Winner of the 2023 IPR Award for Academic Excellence in Polymer Science/Engineering

Hunter Little Biography:
Hunter first joined the Duhamel Lab in 2015 as an undergraduate co-op student, and under the supervision of Prof. Duhamel completed his Bachelor's (2019) and Master's (2022) degrees during which he worked towards developing and applying advanced fluorescence techniques to probe the conformation and internal dynamics of complex macromolecules. In 2023 he began his doctoral studies under the supervision of Prof. Duhamel probing the effect of proline on protein folding using fluorescence. To date, Hunter has contributed to 9 published articles, 12 conference presentations, and has been recognized at the institutional, provincial, and federal levels for his academic achievements, including holding the OGS-M (2020–2021), NSERC-CGSM (2021–2022), and OGS-D (2023–2024). Most recently he has been recognized with the IPR Award for Academic Excellence (2023).

Probing the Local Density of Macromolecules by Fluorescence

<u>Hunter Little</u>, Sanjay Patel, Jean Duhamel.

Institute for Polymer Research, Waterloo Institute for Nanotechnology, Department of Chemistry, University of Waterloo, ON, N2L 3G1, Canada

INTRODUCTION

Macromolecular density is frequently used to characterize the conformation of a macromolecule, often through the radius of gyration (R_g) determined from scattering experiments such as X-ray, static light, or neutron scattering.[1] In theory, any technique capable of measuring the local density of a macromolecule should provide the same information on macromolecular conformation as scattering techniques do. Fluorescence collisional quenching (FCQ) between an excited dye and a quencher covalently attached onto a macromolecule is one such technique that could provide information about the local density of a macromolecule. FCQ yields the rate constant (k_q) for the quenching of a dye by quenchers, which is proportional to the local concentration ($[Q]_{loc}$) of quenchers covalently attached onto a macromolecule through the relationship $k_q = k_{diff} \times [Q]_{loc}$, where k_{diff} is the bimolecular rate constant for diffusive encounters between dyes and quenchers. Two main reasons rationalize why FCQ is not included in the list of techniques capable of characterizing macromolecular conformations. The first reason is the perceived difficulty in accurately measuring $[Q]_{loc}$ inside a macromolecule spanning just a few nanometers, and the second reason is that historically, FCQ has been used to measure the internal dynamics of macromolecules. Work from the Duhamel group has attempted to counter the first of these two factors by proposing that $[Q]_{loc}$ is known from the scheme selected by the experimentalist to label a macromolecule, either at the chain-ends, or randomly along the backbone. Three possible labelling schemes are depicted in Figures 1A–C for linear oligomers and branched dendrimers end-labelled with the fluorophore pyrene and linear polymer chains randomly labelled with pyrene. Of the available fluorophores, pyrene presents many important advantages when used in FCQ experiments. Notably, pyrene forms an excited-state dimer, or excimer, eliminating the need for the selection of a distinct quencher and associated labelling protocol.[2] Therefore, in all further discussion, $[Q]_{loc}$ is replaced with $[Py]_{loc}$ obtained for various pyrene-labeled macromolecules (PyLM).
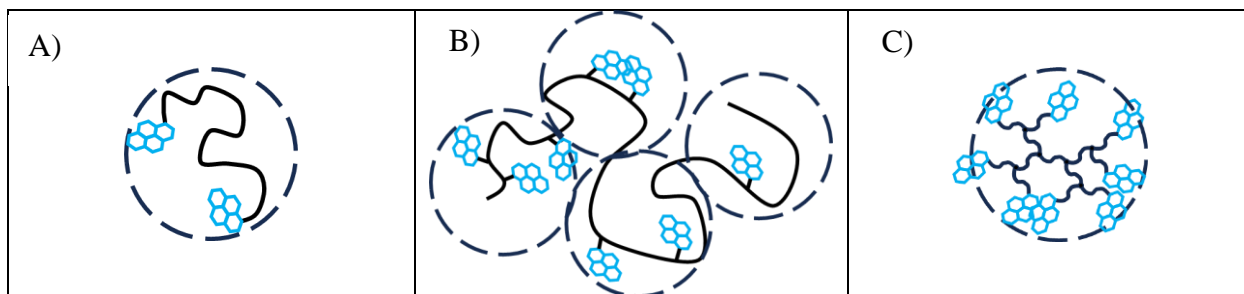
Figure 1. Schematic representation of the three pyrene-labelling schemes studied, (A) pyrene end-labelled linear polymers, (B) polymers randomly labelled with pyrene, and (C) pyrene end-labelled dendrimers. The volume probed by a pyrenyl label is denoted by the dashed circles being either larger in A) and C) or smaller in B) than the macromolecule being studied.

Herein two recent advancements in the ability to probe the local conformation of macromolecules will be discussed. The first experiments demonstrate that $<k>$ determined for PyLM is directly related to the product $k_{diff} \times [Py]_{loc}$, where $[Py]_{loc}$ reflets the conformation of the PyLM, and thus that FCQ can be used to characterize the conformation of macromolecules in solution. The second, built off the first study, demonstrates that this information does not require using the specialized programs developed by the Duhamel laboratory, but can be determined with the standard analysis package of any commercial time-resolved fluorimeter.[3]

EXPERIMENTAL

To demonstrate that FCQ could be used to characterize the conformation of a wide range of macromolecules, three distinct classes of PyLM were identified among those characterized by the Duhamel laboratory over the past 15 years. Monodisperse, pyrene end-labelled polystyrene,[4] poly(ethylene oxides),[5] and poly(N-isopropylacrylamide)[6] were selected to describe the family of PyLM in Figure 1A. Linear chains randomly labeled with pyrene made of poly(methyl acrylate),[7] poly(methyl methacrylate),[7,8] polystyrene,[4] poly(butyl methacrylate),[7] poly(oligo(ethylene glycol methyl ether methacrylate) with side-chain degrees of polymerization equal to 1, 2, 3, 4, 5, 9, 16 and 19,[8] and poly(N-isopropylacrylamide)[6] were selected to represent the PyLM in Figure 1B. Finally, two series of pyrene end-labelled dendrimers consisting of *bis*(hydroxymethyl)propionic acid dendrimers of generations 1–4,[9,10] and polyamidoamine dendrimers of generations 0–2[11] were selected to represent the PyLM in Figure 1C. The initial acquisition and decay analysis for the selected series of macromolecules has been reported elsewhere.[12,13]

RESULTS & DISCUSSION

The Model Free Analysis[14] makes no assumptions about the labeling scheme applied to generate a given PyLM. It only acknowledges that the fluorescence decays of the pyrene monomer and excimer can be described by sums of exponentials, whose pre-exponential factors and decay times are coupled. Experimentally, $<k>$ is then calculated according to Equation 1, using the pre-exponential factors (a_i) and decay times (τ_i) retrieved from the analysis of the monomer decay, along with the natural lifetime of the pyrene monomer (τ_M). A theoretical expression of $<k>$ is obtained by taking the ratio of the number (n_{Py}) of ground-state pyrenes within the volume (V_{Py}) in the PyLM probed by an excited pyrene, whereby V_{Py} can be approximated as a sphere of diameter (L_{Py}) given by the square root of the mean squared end-to-end distance of the polymer segment within that volume.[1]

$$< k >= \frac{\sum_{i=1}^{n} a_i}{\sum_{i=1}^{n} a_i \tau_i} - \frac{1}{\tau_M} = k_{diff} \times [Py]_{loc} = k_{diff} \times \frac{n_{Py}}{V_{Py}} = k_{diff} \times \frac{n_{Py}}{(\pi/6)L_{Py}^3} \tag{1}$$

While n_{Py} is known for the end-labeled linear chains and dendrimers, n_{Py} for randomly labelled polymers is determined from the analysis of the pyrene monomer and excimer fluorescence decays with the fluorescence blob model (FMB). The FBM divides the polymer coil into a cluster of identical *blobs* comprised of N_{blob} structural units which are labelled with n_{Py} pyrenes and both N_{blob} and n_{Py} are determined from the FBM analysis of the fluorescence decays. Since $<k>$ is known from the MFA analysis, and n_{Py} can be determined experimentally, the only remaining unknown in Equation 1 is L_{Py}. The expression of L_{Py} could thus be used as a means of testing the conformation of the macromolecule with the expectation that, for the correct expression of L_{Py}, a plot of $<k>$-vs-n_{Py}/L_{Py}^3 would be linear.

As a first approximation, L_{Py} was expressed for each structural category of macromolecules by considering the chain-segment found inside V_{Py}, with the chain segment representing the whole macromolecule in the case of the end-labelled polymers and dendrimers, or the segment within a *blob* for the randomly labelled polymers. Assuming that the chain segments used to describe the macromolecule obey gaussian statistics, L_{Py} could be approximated by Equation 3, where N is the number of structural units comprising the entire linear chain, or N_{blob} for the chain segment encompassed inside a *blob*, and N_{bb} is the number of backbone atoms per structural unit.

$$L_{Py} = l \times \sqrt{N_{bb} \times N} \tag{3}$$

The description of L_{Py} for the branched dendrimers is more involved, due to the various distances between an excited and ground-state pyrene attached to different ends of the dendrimer which must be accounted for. The derived expressions for L_{Py} as a function of generation number for the PAMAM[10] and HMPA[8] dendrimers have been reproduced below as Equations 5[10] and 6,[8] respectively, where G is the generation number, and the parameters describing the atomistic length of the chain-segments are reported in the original publications.[1,8,10] In Equations 3–5, l is a normalization factor equivalent to the bond-length.[1,8,10]

$$L_{Py}^2(G) = \left(2a + \frac{\left[2 - 2^{G+2} + (G+1) \times 2^{G+3} \right]b + 2^{G+1}c + 2^{G+1} - 1}{2^{G+2} - 1} \right) \times l^2 \tag{4}$$

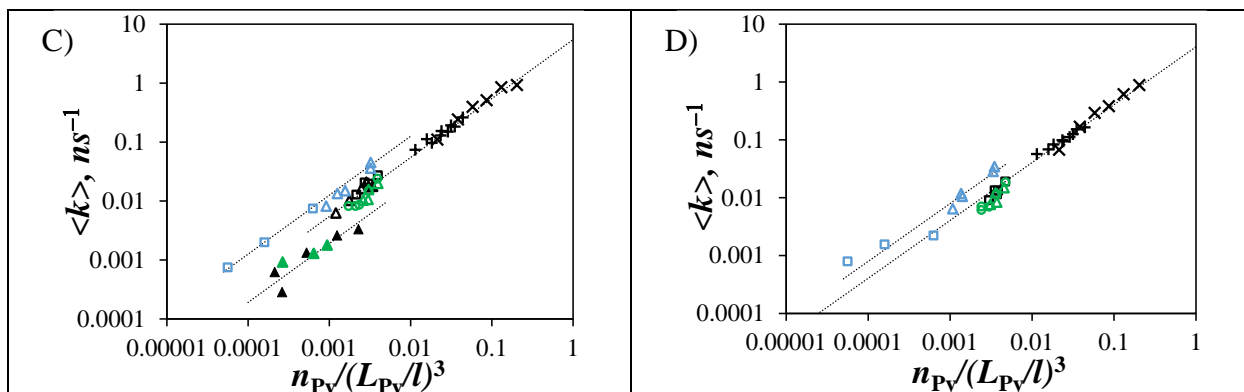$$L_{Py}^2(G) = \left(1 + 2d + e \frac{G \times 2^G - 2^{G+1} + 2}{2^G - 1} \right) \times l^2 \tag{5}$$
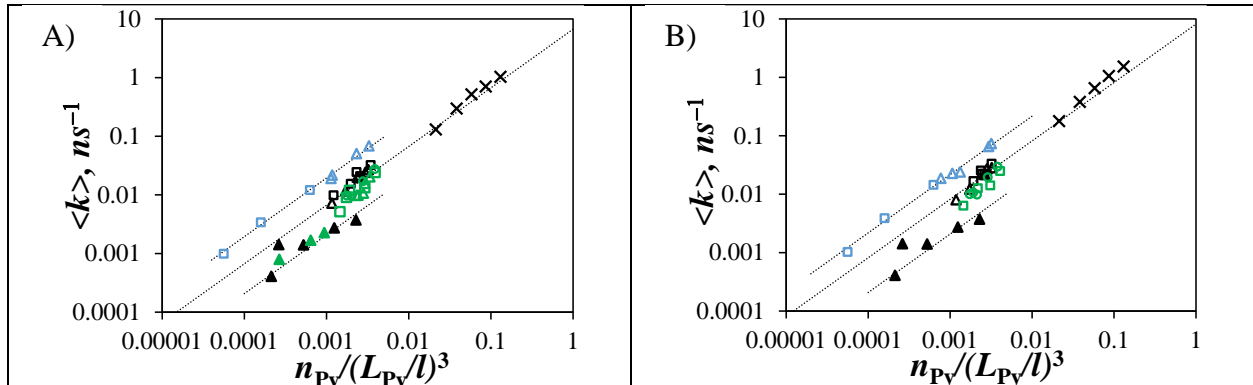
Figure 2. Plots of $<k>$-vs-n_{Py}/L_{Py}^3 in (A) tetrahydrofuran, (B) toluene, (C) dimethylformamide, (D) dimethyl sulfoxide for ($\square$) Py$_2$-PEO,[4] ($\triangle$) Py-PC1A,[6] ($\blacksquare$) Py-PC1MA,[6,7] ($\blacktriangle$) Py-PS,[3] ($\times$) Py-HMPA,[9,10] ($+$) Py-PAMAM,[11] ($\square$) Py-PC4MA,[6,7] ($\bigcirc$) Py-PEG$_1$MA,[7] ($\triangle$) Py-PNIPAM,[5] ($\blacktriangle$) Py$_2$-PS,[3] ($\blacktriangle$) Py$_2$-PNIPAM.[5] In all pots, the slopes have been fixed at unity.

Plotting $<k>$ as a function of n_{Py}/L_{Py}^3 in tetrahydrofuran, toluene, dimethylformamide, and dimethyl sulfoxide for each of the three families of macromolecules resulted in the plots shown in Figures 2A–D. Three lines are observed in Figures 2A–D due to changes in k_{diff} shifting the $<k>$-vs-n_{Py}/L_{Py}^3 up or down for flexible or stiff polymers, respectively.[1] This is perhaps most noticeable for the difference between poly(methyl acrylate) and poly(methyl methacrylate) where the line corresponding to poly(methyl methacrylate) is shifted down towards the main trendline due to the slower dynamics of the backbone induced by the backbone methyl-group. More interestingly are the three regimes seen in each solvent corresponding to each of the three distinct labelling schemes. End-labelled polymer in Figure 1A have low $[Py]_{loc}$ and have correspondingly low $<k>$, while the pyrene-dense dendrimers in Figure 1C have a correspondingly high $[Py]_{loc}$ and $<k>$, and the randomly labelled polymers in Figure 1B with their medium $[Py]_{loc}$ occupy the span between the two extremes. The good linear fits support the assumption that the backbone-segments probed by the pyrene moieties do behave as Gaussian chains in solution. The data shown in Figure 2 represent one of the first examples where FCQ was applied to probe the local density, and thus the conformation, of a macromolecule in solution.

While $<k>$ values thus far have been obtained with the specialized analysis programs used by the Duhamel lab to characterize both the state of the pyrenyl labels (aggregated versus unassociated) and the internal dynamics and local concentration of a pyrene-labeled macromolecules, the question was raised whether $<k>$ could be determined independently from the parameters retrieved from fitting the pyrene monomer decays only with a simple sum of exponentials (SoE). While the parameters retrieved from the global MFA of the pyrene monomer and excimer fluorescence decays are much more accurate, the SoE analysis of the individual fluorescence decays of the pyrene monomer could be easily implemented by any researchers using the standard analysis packages of commercial time-resolved fluorometers. To this end, the monomer and excimer fluorescence decays of the poly(oligo(ethylene glycol) methyl ether methacrylate)s[8] and polyamidoamine dendrimers[11] were reanalyzed using the sum of exponentials described in Equations 6 & 7, respectively.

$$[M^*]_{(t)} = [Py^*]_o \times \left[f_{diff} \sum_{i=1}^{N} a_i \exp(-t/\tau_i) + f_{free} \exp(-t/\tau_M) \right] \tag{6}$$

59

$$[E^*]_{(t)} = \sum_{i=1}^{N} b_i \exp(-t / \tau_i) \tag{7}$$

$<k>$ was then calculated according to Equation 1 using the parameters retrieved from Equation 7, and the ratio $-A_E-/A_{E+}$ which is the sum of the negative pre-exponential factors divided by the sum of the positive pre-exponential factors, was calculated from the parameters retrieved from Equation 8. The $-A_E-/A_{E+}$ ratio is expected to report on the amount of pyrene able to form excimer by diffusion, with a $-A_E-/A_{E+} \approx 1.0$ or 0.0 corresponding to excimer formed solely through diffusive encounters or direct excitation of a pyrene dimer, respectively. Consequently, the $-A_E-/A_{E+}$ ratio reflects the parameter f_{diff}, which is the molar fraction of pyrene forming excimer by diffusion, determined from the MFA. Figure 3 shows a comparison of the two analyses,[3] with Figure 3A showing the direct comparison of $<k^{SoE-M}>$ and $<k^{MF}>$, and Figure 3B and C showing the values taken by the ratios $f_{diff}/(f_{diff}+f_{agg})$ and $-A_E-/A_{E+}$ for the MFA and SoE analysis, respectively.

In Figure 3A, the $<k>$ values retrieved from the two different analyses cluster along the one-to-one diagonal with a Pearson correlation coefficient of 0.99. This indicates that, despite the large differences in the analysis protocols, the MFA and SoE both retrieved the same information, which can then be used to determine the conformation of the macromolecule. This is advantageous as it allows other research groups who rely on the commercial analysis package of the time-resolved fluorometer to use $<k>$ to characterize the unknown conformation of their macromolecule. Figure 3B and C compare the ratios $f_{diff}/(f_{diff}+f_{agg})$ and $-A_E-/A_{E+}$ as a function of $<k>$, respectively. Since only pyrenes which form excimer through diffusive encounters report on the dynamics and conformation of a macromolecule, this procedure is useful to ensure that excimer formation occurs through diffusive encounters between pyrenyl labels. It also demonstrates that the qualitative information obtained with $-A_E-/A_{E+}$ about the state of the pyrenyl labels obtained from the simpler SoE analysis reflects the quantitative information retrieved with $f_{diff}/(f_{diff}+f_{agg})$ from the superior MFA.

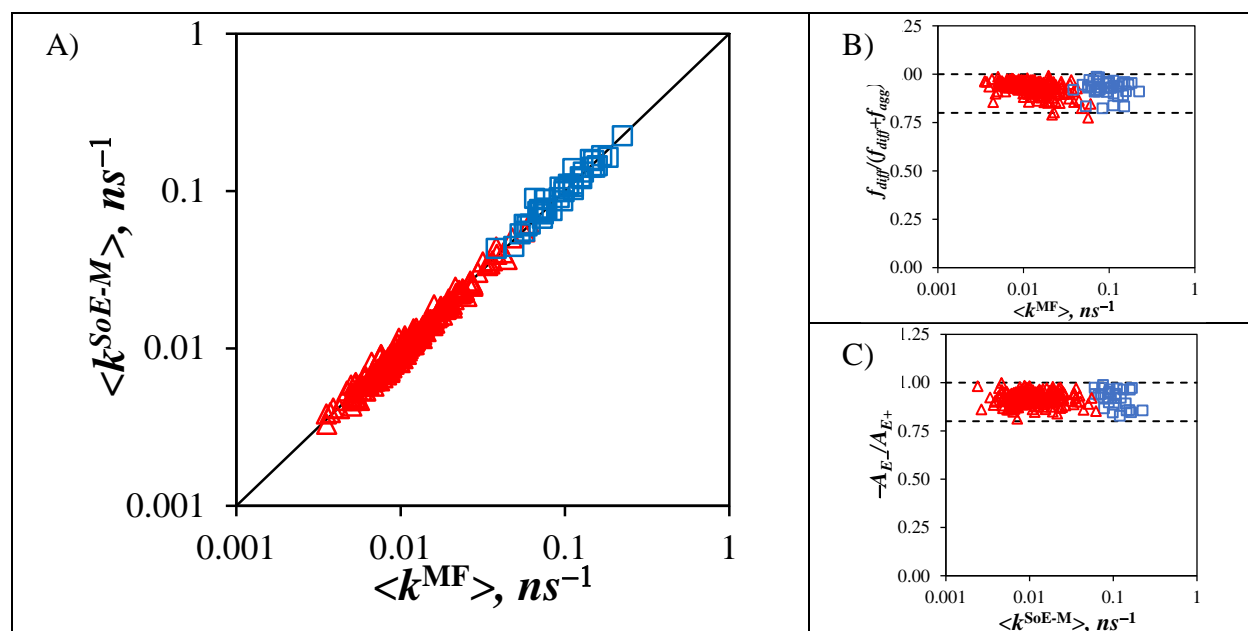**Figure 3.** Plots of A) $<k^{SoE\text{-}M}>$ as a function of $<k^{MF}>$, B) $f_{diff}/(f_{diff} + f_{agg})$ as a function of $<k^{MF}>$ and C) $-A_{E-}/A_{E+}$ as a function of $<k^{SoE\text{-}M}>$ for the for the ($\triangle$) Py-PEG$_n$MA and ($\square$) PyCX-PAMAM-GY samples.[3]

CONCLUSIONS

These two recent studies from the Duhamel laboratory have shown that not only is it possible to use FCQ as a complementary technique to determine the local density, and thus the conformation, of a macromolecule, but that such studies can be completed with a simpler analysis of fluorescence decays, that is readily available with any commercial time-resolved fluorimeters. This represents a significant advantage over the traditional scattering methodologies which require high concentrations of monodisperse polymers, experimental requirements that are easily circumvented by FCQ studies. Furthermore, the good match obtained between the $<k>$ values retrieved from the analysis of fluorescence decays with a simple SoE and those found from the superior MFA opens the doors for the use of the simpler SoE analysis to study other more complex macromolecular systems.

REFERENCES

(1) Little, H.; Patel, S.; Duhamel, J. Probing the Inner Local Density of Complex Macromolecules by Pyrene Excimer Formation. *Phys. Chem. Chem. Phys.* **2023**, *25*, 26515–26525.

(2) Duhamel, J. Global Analysis of Fluorescence Decays to Probe the Internal Dynamics of Fluorescently Labeled Macromolecules. *Langmuir* **2014**, *30*, 2307–2324.

(3) Hunter Little; Sanjay Patel; David Suh; Jean Duhamel. Accurate Determination of the Average Rate Constant of Pyrene Excimer Formation for Pyrene-Labeled Macromolecules from the Analysis of Individual Fluorescence Decays with Sums of Exponentials. *J. Phys. Chem. B* **2024**.

(4) Ingratta, M.; Hollinger, J.; Duhamel, J. A Case for Using Randomly Labeled Polymers to Study Long-Range Polymer Chain Dynamics by Fluorescence. *J. Am. Chem. Soc.* **2008**, *130*, 9420–9428.

(5) Chen, S.; Duhamel, J.; Winnik, M. A. Probing End-to-End Cyclization beyond Willemski and Fixman. *J Phys Chem B* **2011**, *115*, 3289–3302.

(6) Yip, J.; Duhamel, J.; Qiu, X. P.; Winnik, F. M. Long-Range Polymer Chain Dynamics of Pyrene-Labeled Poly(N -Isopropylacrylamide)s Studied by Fluorescence. *Macromolecules* **2011**, *44*, 5363–5372.

(7) Farhangi, S.; Weiss, H.; Duhamel, J. Effect of Side-Chain Length on the Polymer Chain Dynamics of Poly(Alkyl Methacrylate)s in Solution. *Macromolecules* **2013**, *46*, 9738–9747.

(8) Little, H.; Thoma, J. L.; Yeung, R.; D'Sa, A.; Duhamel, J. Persistence Length and Encounter Frequency Determination from Fluorescence Studies of Pyrene-Labeled Poly(Oligo(Ethylene Glycol) Methyl Ether Methacrylate)s. *Macromolecules* **2023**, *56*, 3562–3573.

(9) McNelles, S. A.; Thoma, J. L.; Adronov, A.; Duhamel, J. Quantitative Characterization of the Molecular Dimensions of Flexible Dendritic Macromolecules in Solution by Pyrene Excimer Fluorescence. *Macromolecules* **2018**, *51*, 1586–1590.

(10) Thoma, J. L.; McNelles, S. A.; Adronov, A.; Duhamel, J. Direct Measure of the Local Concentration of Pyrenyl Groups in Pyrene-Labeled Dendrons Derived from the Rate of Fluorescence Collisional Quenching. *Polymers* **2020**, *12*, 2919.

(11) Patel, S.; Duhamel, J. Macromolecular Conformation of Low-Generation PAMAM Dendrimers Probed by Pyrene Excimer Formation. *Macromolecules* **2023**, *56*, 4012–4021.

(12) Fowler, M. A.; Duhamel, J.; Bahun, G. J.; Adronov, A.; Zaragoza-Galán, G.; Rivera, E. Studying Pyrene-Labeled Macromolecules with the Model-Free Analysis. *J. Phys. Chem. B* **2012**, *116*, 14689–14699.

(13) Farhangi, S.; Casier, R.; Li, L.; Thoma, J. L.; Duhamel, J. Characterization of the Long-Range Internal Dynamics of Pyrene-Labeled Macromolecules by Pyrene Excimer Fluorescence. *Macromolecules* **2016**, *49*, 9597–9604.

(14) Siu, H.; Duhamel, J. Comparison of the Association Level of a Pyrene-Labeled Associative Polymer Obtained from an Analysis Based on Two Different Models. *J. Phys. Chem. B* **2005**, *109*, 1770–1780.

FRANKLIN FRASCA
Chemistry
Waterloo

Determining the Conformations of Pyrene-Labeled Polyamines and Polyols in Solution via Pyrene Excimer Fluorescence

Determining the Conformations of Pyrene-Labeled Polyamines and Polyols in Solution via Pyrene Excimer Fluorescence

Franklin Frasca and Jean Duhamel

INTRODUCTION

The ability of pyrene to fluoresce differently whether it exists either as a lone monomer or an excited dimer, also known as an excimer formed upon the encounter between a ground-state and an excited pyrene, provides a powerful tool for obtaining information about the dynamics and conformation of macromolecules of any size in solution. Pyrene excimer formation (PEF) allows for the characterization of many complex pyrene-labeled macromolecules (PyLMs) in solution which would be difficult to characterize by any other common techniques based on scattering, viscosity, or NMR experiments. Due to the high molar extinction coefficient and fluorescence quantum yield of pyrene, PEF also enables the study of PyLMs under extremely dilute conditions (~ 1 – 10 mg/L) which provides an unperturbed view of the PyLM of interest. This is in direct contrast to most other techniques which often require concentrations (~ 1 – 10 g/L) that are so high that the polymers are likely undergoing intermolecular interactions, further complicating the resolution of the internal dynamics and conformation of single macromolecules. While many experiments have been conducted to get a qualitative measure of the PEF efficiency, for example using the I_E/I_M ratio to determine the relative amounts of excimer and monomer fluorescence, respectively, the quantitative analysis of PEF remains difficult and as a result is much more rarely used to glean information on macromolecular dynamics and conformation.

In earlier works, PEF was used to determine the rate of end-to-end cyclization (k_{cy}) of monodisperse linear chains with a pyrene appended to each end by using time-resolved (TRF) and steady-state (SSF) fluorescence.[1-3] These studies took advantage of the theoretical work by Wilemski and Fixman,[4,5] who had found that the slowest internal relaxation time of a polymer was the rate constant k_{cy} of end-to-end cyclization, which was proportional to the rate constant for PEF determined through analysis of the fluorescence decays of the pyrene end-labeled polymer. While useful, these studies highlighted the requirement for monodisperse chains for the accurate determination of k_{cy}, which provided the internal relaxation time of a polymer. Furthermore, the limitation of having only two pyrenes per molecule restricted the determination of k_{cy} to chains that were sufficiently short to enable PEF between the two terminal pyrenyl labels. Following this preliminary work, numerous other studies and models were developed in an attempt to better quantify polymer dynamics and conformation using PEF, namely the Model Free Analysis (MFA) which makes no assumptions about the nature of excimer formation to determine the average rate constant of PEF ($<k>$), and the Fluorescence Blob Model (FBM) which views a polymer which has been randomly labeled with pyrene as a series

of blobs in which the pyrenes can only form excimer within a blob to yield information on polymer backbone conformation and flexibility.

Because PEF is a bimolecular process, the rate of PEF depends on the local pyrene concentration ($[Py]_{loc}$) of a pyrene-labeled molecule in solution given by Equation 1. In Equation 1, $<L_{Py}^2>^{1/2}$ represents the average end-to-end distance between two pyrenyl labels on the PyLM, defining a volume equal to $(<L_{Py}^2>^{1/2}/l)^3$ occupied by the ground-state pyrenes and PyLM. The general scheme of PEF and the associated SSF spectrum of a pyrene-labeled small molecule (PyLsM) are shown in Figure 1.

$$[Py]_{loc} = \frac{\# \, GS \, Py}{V_{PyLM}} \propto \frac{\# \, GS \, Py}{\left(\langle L_{Py}^2 \rangle^{1/2}/l\right)^3} = n_{Py} / \left(L_{Py}/l\right)^3 \tag{1}$$
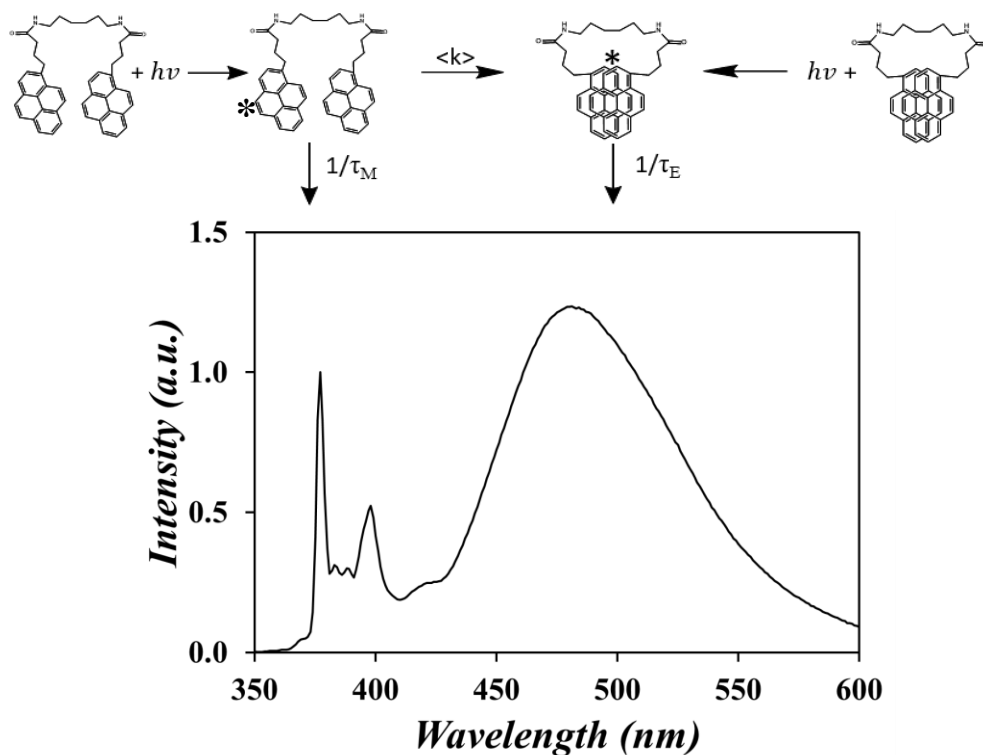
Figure 1. Top: The general scheme of PEF. Bottom: The steady-state fluorescence spectrum of hexamethylene *bis*(1-pyrenebutyramide) (Py₂-HMDA), normalized to the monomer peak at 377 nm; λ_{ex} = 344 nm, [Py] = 2.5×10⁻⁶ M in THF.

Analysis of SSF spectra can provide qualitative information on PEF via integration of the excimer and monomer emissions between 500 – 530 and 372 – 378 nm, respectively, to yield the I_E/I_M ratio and gauge the relative amounts of excimer and monomer fluorescence of the PyLM of interest in solution. While useful for many studies, the SSF spectra are prone to suffer from several artifacts due to solvent effects, aggregation of the

pyrenyl labels (right pathway for PEF in the reaction scheme shown in Figure 1), and/or the presence of residual unreacted pyrene derivative used in the preparation of the PyLM which can distort the spectra and greatly complicate the use of the I_E/I_M ratio. On the other hand, MFA of the monomer and excimer decays obtained through TRF measurements can yield both the molar fractions of different pyrene species contributing to PEF and $<k>$, the average rate constant for PEF by diffusion (left pathway for PEF in the reaction scheme in Figure 1). The MFA of the TRF decays also yields the molar fractions f_{diff}, f_{agg}, and f_{free} representing the pyrenes forming excimer diffusively, through aggregation, or not forming excimer and fluorescing as monomers, respectively. The molar fractions can provide information on both the extent of free pyrene impurities in solution and through which pathway, either diffusive or aggregation, the excimer is being formed. The number average lifetime ($<\tau>$) is obtained with the MFA and is used to determine $<k>$ as described in Equation 2. Both $<k>$ and the I_E/I_M ratio have been shown in previous work to be proportional to $[Py]_{loc}$ based on Equation 3.[Error! Bookmark not defined.-7] k_{diff} in Equation 3 is the bimolecular rate constant for PEF by diffusion, and provides a measure of the dynamics of the PyLM in solution. Since $[Py]_{loc}$ is related to the conformation of the macromolecule through L_{Py}, so is $<k>$ according to Equation 3.

$$< k >=\frac{1}{<\tau>}-\frac{1}{\tau_M} \tag{2}$$

$$\frac{I_E}{I_M} \propto k_{diff} \times [Py]_{loc} =< k > \tag{3}$$

The linear relationship between $<k>$, the I_E/I_M ratio, and $[Py]_{loc}$ has thus far only been demonstrated quantitatively for series of pyrene end-labeled dendrimers, linear oligomers, and linear chains randomly labeled with pyrene.[Error! Bookmark not defined.,8] Because of the direct correlation between $[Py]_{loc}$, local macromolecular density, and thus macromolecular conformation, the $<k>$-vs-$[Py]_{loc}$ relationship given in Equation 3 can be used to characterize macromolecular conformation. Since Equation 3 has been applied solely to probe the conformation of PyLM to date, the present work aims to expand its validity to much smaller pyrene-labeled macromolecules (PyLsM) such as pyrene-labeled polyols (Py-POs) and polyamines (Py-PAs) to confirm that this PEF-based methodology can be applied to characterize the internal dynamics and conformation of not only PyLM but also PyLsM in dilute solution.

EXPERIMENTAL

A series of pyrene-labeled polyamines (Py-PAs) and pyrene-labeled polyols (Py-POs), whose structures are shown in Figures 2 and 3 respectively, were synthesized yielding both doubly end-labeled linear chains and branched architectures having more than two

pyrenyl moieties. Dilute solutions of each Py-PA and Py-PO were prepared in THF, dioxane, DMF, and DMSO, a set of common organic solvents which solubilize a wide range of both synthetic and bio-based polymers. Their SSF spectra were acquired to yield their I_E/I_M ratios, and MFA of the monomer and excimer TRF decays yielded their $<k>$ values, respectively. Each Py-PA or Py-PO was diluted to [Py] = 2.5×10^{-6} M before acquisition of the SSF spectra and monomer and excimer TRF for analysis with the MFA.
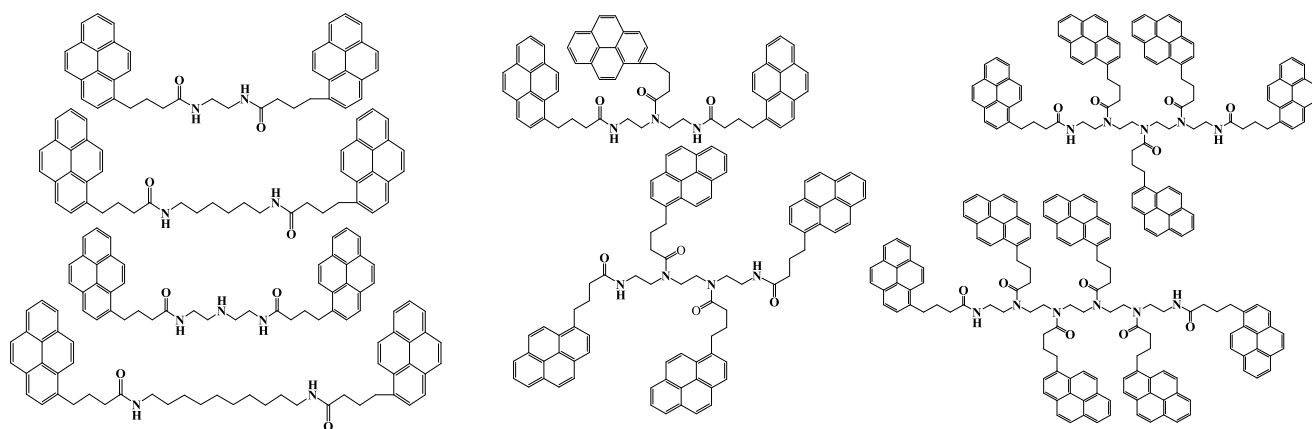
Figure 2. Chemical structures of the Py-PAs prepared for this study.
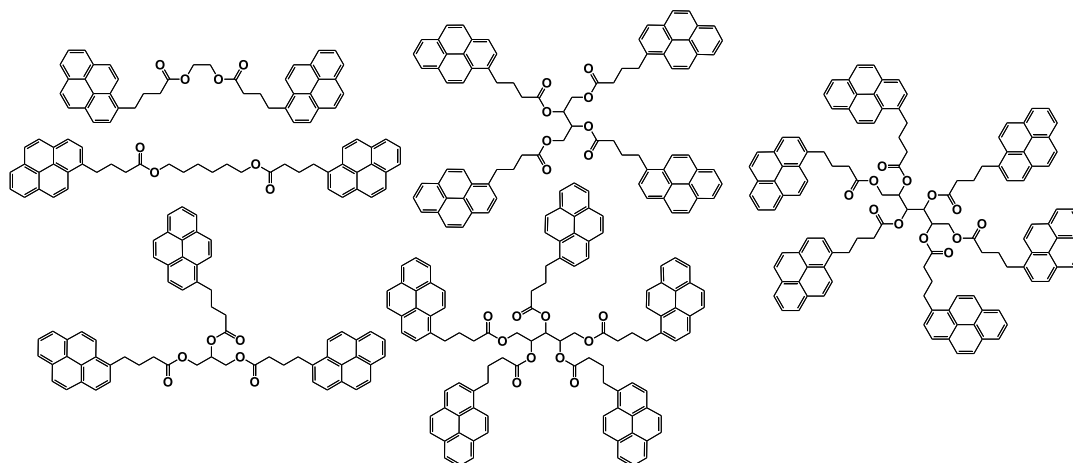
Figure 3. Chemical structures of the Py-POs prepared for this study.

RESULTS & DISCUSSION

Analysis of the SSF spectra and MFA of the TRF decays yielded the I_E/I_M ratio and $<k>$, respectively, for each Py-PA and Py-PO in THF, dioxane, DMF, and DMSO. $[Py]_{loc}$ was calculated for each Py-PA and Py-PO according to Equation 1 to generate plots of $<k>$-*vs*-$[Py]_{loc}$ in each solvent studied, which are shown in Figure 4.

  The $<k>$ values for the Py-PAs and Py-POs in both DMF and DMSO shown in Figures 4B and D exhibit a linear trend against $[Py]_{loc}$, supporting the validity of Equation 1 for determination of $[Py]_{loc}$ and in turn the internal density of PyLMs in solution, now

for a series of small molecules. While the Py-POs also showed a linear trend of *<k>-vs-*[*Py*]loc in the less-polar THF and dioxane, the Py-PAs showed a deviation from linearity for the branched molecules having more than 2 pyrene moieties. Of note was that even though the Py-POs displayed similar behaviour in both the polar and non-polar solvents, the Py₂-Ethylene glycol Py-PO showed a stark deviation from the other Py-POs (although more diols require pyrene labeling to fully assess the Py-POs' *<k>-vs-*[*Py*]loc behaviour).
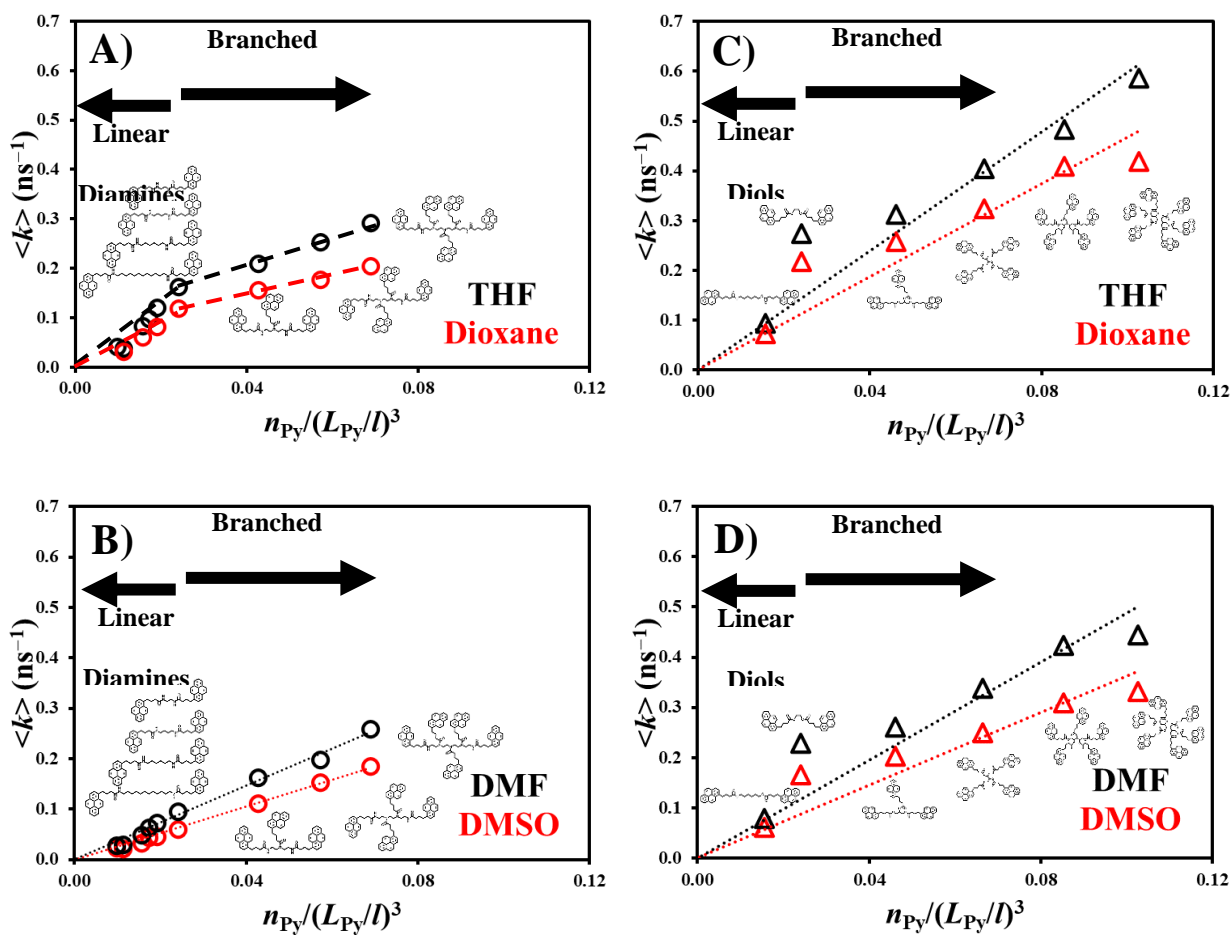
Figure 4. Plots of *<k>-vs-*[*Py*]loc obtained from the MFA of the monomer and excimer fluorescence decays for Py-PAs acquired in A) THF and dioxane, and B) DMF and DMSO, and the Py-POs acquired in C) THF and dioxane, and D) DMF and DMSO; [Py] = 2.5×10⁻⁶ M.

The Py-POs on the right of Figure 4 are seen to span a wider range of [*Py*]loc values than the Py-PAs, and thus reach higher *<k>* values. Furthermore, the slopes for the Py-POs are greater than those for the Py-PAs in the same solvents. This shows that with each of the [*Py*]loc values for the Py-PAs and Py-POs calculated in the same manner, the differences in *<k>-vs-*[*Py*]loc trends between the two Py-LsM families can be attributed to

68

the difference in k_{diff} and in-turn a measure of the dynamics of the pyrene-modified Py-PAs or Py-POs. To be put more simply, this means that the pyrenes on the Py-PAs diffuse more slowly and thus have a lower rate of excimer formation (or pyrene-pyrene encounters) compared to the pyrenes on the Py-POs which diffuse more quickly yielding a higher rate of excimer formation $<k>$. Since both the Py-PAs and Py-POs have a similar mix of difunctional and branched structures, it leaves the amide or ester groups, respectively, as the major difference between the two families. It is worth noting that the pyrene groups are linked directly to amines in the backbone of the branched Py-PAs, whereas the ester linkages of the Py-POs reside 1 atom away from the polyol backbone, possibly providing a greater degree of flexibility and higher k_{diff} value to the Py-POs in contrast to the Py-PAs.

CONCLUSIONS

A series of Py-PAs and Py-POs were synthesized and their SSF spectra and TRF decays were acquired and analysed. Equation 1 was applied to determine $[Py]_{loc}$ for each Py-PA and Py-PO before $<k>$ was obtained from the MFA of the monomer and excimer fluorescence decays and plotted as a function of $[Py]_{loc}$ in THF, dioxane, DMF, and DMSO. The $<k>$-vs-$[Py]_{loc}$ trends were linear for both the Py-PAs and Py-POs in DMF and DMSO, with the Py-POs also yielding linear trends in the less-polar THF and dioxane. The trends in DMSO and DMF confirmed that the PEF-based methodology can be applied not only to study large PyLM but also PyLsM to characterize the internal dynamics and conformation of pyrene-labeled molecules, in this instance specifically the Py-PAs and Py-POs. These findings also further validate the assumption that the pyrene-labeled chain ends of these small molecules obey gaussian statistics, opening the door for future studies of the internal dynamics of more complex PyLMs in solution.

REFERENCES

1. Winnik, M. A.; Redpath, T. The Dynamics of End-to-End Cyclization in Polystyrene Probed by Pyrene Excimer Formation. *Macromolecules* **1980**, *13*, 328-335.
2. Winnik, M. A.; Redpath, A. E. C.; Paton, K.; Danhelka, J. Cyclization dynamics of polymers: 10 Synthesis, fractionation, and fluorescent spectroscopy of pyrene end-capped polystyrenes. *Polymers* **1984**, *25*, 91-99.
3. Winnik, M. A. End-to-End Cyclization of Polymer Chains. *Acc. Chem. Res.* **1985**, *18*, 73-79.
4. Wilemski, G.; Fixman, M. Diffusion controlled intrachain reactions of polymers. I Theory. *J. Chem. Phys.* **1974**, *60*, 866-877.
5. Wilemski, G.; Fixman, M. Diffusion controlled intrachain reactions of polymers. II Results for a pair of terminal reactive groups. *J. Chem. Phys.* **1974**, *60*, 878-890.

6. Duhamel, J. New Insights in the Study of Pyrene Excimer Fluorescence to Characterize Macromolecules and their Supramolecular Assemblies in Solution. *Langmuir* **2012**, *28*, 6527-6538.
7. Thoma, J.; McNelles, S. A.; Adronov, A.; Duhamel, J. Direct Measure of the Local Concentration of Pyrenyl Groups in Pyrene-Labeled Dendrons Derived from the Rate of Fluorescence Collisional Quenching. *Polymers* **2020**, *12*, 2919.
8. Little, H.; Patel, S.; Duhamel, J. Probing the inner local density of complex macromolecules by pyrene excimer formation. *Phys. Chem. Chem. Phys.* **2023**, *25*, 26515.

KRISTIJAN LULIC
Chemistry
Waterloo

Pyrene Excimer Formation as a Means to Investigate Persistence Length of Alkyl Methacrylate Copolymers

Pyrene Excimer Formation as a means to Investigate Persistence Length of Alkyl Methacrylate Copolymers

Kristijan Lulic, Gregoire Muller, Renzo Gutierrez, and Jean Duhamel*

Institute for Polymer Research, Waterloo Institute for Nanotechnology, Department of Chemistry, University of Waterloo, ON N2L 3G1, Canada

INTRODUCTION

The mechanical properties of plastics or gels are fundamental to our understanding of their behaviour. The rate at which a plastic or a gel can deform at the macroscopic level is a direct consequence of the flexibility of its individual polymer chains, and their ability to bend under stress at the molecular level.[1] The persistence length (l_p) of a polymer is a parameter used to quantify this flexibility. For polymers possessing a greater persistence length, a more extended conformation is expected, resulting in a stiffer plastic/gel when compared to those prepared from a polymer with a shorter persistence length.[2,3] In the case of gels, relating l_p to other physical parameters such as the modulus, G, has been the focus of concerted research effort to better understand the viscoelastic properties of a polymer in solution.[4,5] Furthermore, predicting l_p for polymer chains bears industrial significance, particularly for polymers such as poly(alkyl methacrylate)s (PAMA), which are used as engine oil additives in lubricant formulations.[6] These polymers can serve as pour-point depressants (PPDs) that interact with paraffinic wax crystals that form a network in oil below a certain threshold temperature, known as the pour-point, leading to a dramatic increase in the oil viscosity.[7] This increase in viscosity does not automatically result in catastrophic failure of engine components, but does significantly reduce the lifetime expectancy of these parts upon ignition in colder climates. PPDs maintain the fluidity of an engine oil at low temperatures by interacting with these wax crystals.[7] Although not explicitly stated in the technical literature, these macromolecules are PAMAs with alkyl side chains of different lengths that modulate the viscosity of the oil in an internal combustion engine. Longer alkyl side chains are essential to the disruption of the wax crystal network formation, while intermediate alkyl side chain lengths contribute to stabilizing the polymer in the nonpolar environment generated by an engine oil.[8] Shorter side chains serve as spacers that enhance backbone flexibility to better accommodate the microstructure of the wax crystal, and ultimately make a more effective PPD.[8,9]

The l_p of a polymer can be determined experimentally, but the methods involved have their own challenges. As a result, and despite its importance, l_p remains unknown for many polymers. Techniques traditionally used in the determination of l_p include static light scattering,[1] intrinsic viscosity,[1] and gel permeation chromatography (GPC) with a scattering or viscosity detector,[2] which relate l_p to the radius of gyration, or intrinsic viscosity, respectively. Though these are powerful tools for the characterization of polymers, stringent limitations remain regarding their applicability to the determination of l_p. First, scattering experiments require that the polymers have a narrow molecular weight distribution (MWD),[10] which are typically generated by living polymerization techniques. Unfortunately, not all monomers can be polymerized by living techniques and those monomers yield polymers with broad MWD. The determination of the

persistence length for such polymers requires that they be analyzed with a GPC instrument equipped with a static light scattering or viscosity detector. However, GPC instruments are commonly used with a specific solvent, which may not always be ideal for a particular polymer. Polymers which are poorly soluble in a given solvent, interact with the packing material of the GPC column, yielding distorted GPC traces that prevent their analysis to determine l_p.[11] The appeal of these techniques for determining l_p resides in their ability to probe the local density of a macromolecule inside the macromolecular volume through the determination of the radius of gyration or intrinsic viscosity. Since a more flexible polymer can accommodate a larger number of structural units within the macromolecular volume compared to its stiffer counterpart, the coil of the latter polymer is less dense than that of the former. Hence, the interest in techniques capable of probing the local density of a macromolecule to determine l_p. Consequently, any technique able to probe the local density of a macromolecule, can in theory, be used to determine l_p.

One such technique is based on pyrene excimer formation (PEF). Pyrene has been extensively used in the characterization of macromolecules in solution, owing in part to its long fluorescence lifetime, high quantum yield, and above all else, its ability to form an excimer.[12] The excimer is formed upon encounter between an excited and a ground state pyrenes. The emission of the pyrene excimer is broad and distinct from that of the pyrene monomer.[12] Conveniently, hardly any energy hopping occurs between pyrene derivatives attached onto a macromolecule due to the reduced 0-0 transition of pyrene so that when excited, the excitation remains localized on a pyrene molecule. Therefore, PEF is exclusively governed by the diffusion of the polymer backbone. Moreover, PEF can be monitored through the analysis of the time-resolved fluorescence (TRF) decays of the pyrene monomer and excimer.

In a typical experiment, the pyrene monomer and excimer fluorescence decays are globally analyzed with the fluorescence blob model (FBM). The FBM acknowledges that an excited pyrenyl label can only probe a certain volume around itself during the finite temporal window (~ 1 μs) of its excitation.[13] This volume is referred to as a *blob* and is used as a unit volume to compartmentalize the macromolecule into a cluster of identical *blobs*, whose size depends on the internal dynamics and flexibility of the polymer, the solvent viscosity, and the length of the spacer used to link the pyrene moiety to the polymer backbone. The power of the FBM resides in its ability to analyze the fluorescence decays of polydisperse polymers randomly labeled with pyrene and obtain the absolute number (N_{blob}) of structural units encompassed inside a *blob*.[13] This quantity has been extensively used in the Duhamel Lab to quantify the flexibility of a polymer, with more flexible polymers yielding greater N_{blob} values. As both l_p and N_{blob} reflect the ability of a polymer chain to bend, these two parameters are correlated.[14,15] Taking this into consideration, a series of pyrene-labeled PAMAs were synthesized through terpolymerization of *n*-butyl, stearyl, and 1-pyrenebutyl methacrylate. Although the resulting polymers are terpolymers, they are referred to as pyrene-labeled copolymers of *n*-butyl and stearyl methacrylate due to their low pyrene content (< 8 mol%) which is neglected when discussing the effect of their composition on l_p. The fluorescence decays of the pyrene-labeled copolymers were acquired and analyzed with the FBM to determine N_{blob}, which was subsequently compared to the N_{blob} values previously determined for the pyrene-labeled PAMA homopolymers.[16] This comparison indicates that homopolymer and copolymer alike yield identical N_{blob} values given the same average molecular

weight of a structural unit. N_{blob} was then used to determine l_p for the PAMA copolymers and l_p was found to increase linearly with the squared molar fraction of stearyl methacrylate in the copolymers, as expected theoretically.[17] This study represents the first example in the literature where the persistence length of PAMA copolymers was characterized as a function of the molar fraction of one of their comonomers and the simple relationship found between l_p and the molar fraction of the comonomer of a PAMA copolymer should provide a powerful means to predict l_p for these commercially important polymers. This study also confirms that the PEF-based methodology is a powerful tool to determine l_p for polymers.

EXPERIMENTAL

Chemicals: *n*-Butyl methacrylate, stearyl methacrylate, methacrylic anhydride, azobisisobutyronitrile (AIBN), 1-pyrenebutanol, dimethylaminopyridine (DMAP), toluene, methanol, and dichloromethane were purchased from Sigma-Aldrich.

Synthesis of the pyrene-labeled poly(n-butyl methacrylate-co-stearyl methacrylate): A series of copolymers composed of butyl methacrylate (C_4MA), stearyl methacrylate ($C_{18}MA$), and 1-pyrenebutyl methacrylate (PyBuMA) (Py-P(C_4MA-co-$C_{18}MA$)) were prepared by free radical polymerization in toluene at 63 °C, using AIBN as the initiator. To minimize composition drift, the polymerization was monitored by ^1H NMR to keep the conversion below 20%. Once an appropriate conversion was achieved, the polymerization was terminated by exposure to air. The product was precipitated four times in chilled methanol to eliminate any unreacted material and the mixture was centrifuged to recover the copolymers. Following purification, the samples were dried under vacuum for a minimum of 12 hours to remove residual solvent. PyBuMA used to introduce the pyrenyl label in the Py-P(C_4MA-co-$C_{18}MA$) samples was synthesized by methacrylation of 1-pyrenebutanol. PyBuMA was synthesized by reacting 0.42 mL (2.8 mmol) of methacrylic anhydride with 0.50 g (1.8 mmol) of 1-pyrenebutanol in the presence of 0.0445 g (0.36 mmol) of dimethylaminopyridine in 50 mL of distilled dichloromethane. A series of copolymers with a same C_4MA-to-$C_{18}MA$ ratio were prepared with pyrene contents ranging from 0.5 to 8 mol%. The C_4MA-to-$C_{18}MA$ ratio was adjusted from 0.19 to 21 to generate 5 series of Py-P(C_4MA-co-$C_{18}MA$) samples with varying pyrene contents.

Chemical composition and molecular weight distribution of the copolymers: The pyrene content of the Py-P(C_4MA-co-$C_{18}MA$) samples was determined by UV-Vis spectroscopy. Solutions of Py-P(C_4MA-co-$C_{18}MA$) with a known mass concentration (m) were prepared in THF. The absorbance was then measured at 344 nm using a Varian Cary 100 Bio UV-Vis spectrophotometer with a 1 cm pathlength cell. The molar extinction coefficient of 1-pyrenebutanol was determined to equal 42,250 $M^{-1}.cm^{-1}$ in THF.[15] Application of the Beer-Lambert's Law yielded the pyrene concentration ([Py]). The molar fraction (x) of pyrene-labeled structural units in the copolymer was determined based on the pyrene content ($\lambda_{Py} = [Py]/m$) with Equation 1, where y is the molar ratio of $C_{18}MA$-to-C_4MA ($y = x_{C18MA}/x_{C4MA}$) determined beforehand by ^1H NMR. In Equation 1, M_{C18MA}, M_{C4MA}, and M_{Py} are the molar masses of stearyl methacrylate, *n*-butyl methacrylate, and 1-pyrenebutyl methacrylate equal to 338.6, 142.2, and 342.4 g/mol, respectively.

$$x = \frac{yM_{C18MA}+M_{C4MA}}{(1+y)/\lambda_{Py}+yM_{C18MA}+M_{C4MA}-(1+y)M_{Py}} \qquad (1)$$

Py-P(C$_4$MA-*co*-C$_{18}$MA) copolymers with five molar ratios with *y* equivalent to 0.19, 1.1, 2.4, 4.3, and 21 were prepared and characterized, corresponding to 15, 50, 70, 80, and 95 mol% of C$_{18}$MA, respectively. The molar ratio was determined through the analysis of the ^{1}H NMR and UV-Vis absorption spectra acquired with all of the Py-P(C$_4$MA-co-C$_{18}$MA) samples.

The number (M_n) and weight (M_w) average molecular weights of the Py-P(C$_4$MA-*co*-C$_{18}$MA) samples were determined by gel permeation chromatography (GPC) with a Viscotek GPC instrument equipped with a 305 triple detection array, comprising a differential refractive index (DRI), viscosity, and light scattering detectors.

Fluorescence Analysis: The fluorescence measurements were performed on the Py-P(C$_4$MA-co-C$_{18}$MA) samples dissolved in THF with an optical density (OD) of 0.1, corresponding to a pyrene concentration of 2.5 µmol/L or a polymer mass concentration of approximately 5 mg/L. Samples were degassed for 30 minutes under a steady nitrogen flow to remove oxygen, as it is a known quencher of fluorescence. Fluorescence spectra were acquired from 350 to 600 nm, with an excitation wavelength of 344 nm. For time-resolved fluorescence measurements, the excitation wavelength was set at 379 and 510 nm for the pyrene monomer and excimer, respectively. The FBM was then applied to fit the monomer and excimer fluorescence decays globally to determine N_{blob}. The calculation of N_{blob} was conducted with Equation 2, where $<n>$ is the average number of ground-state pyrenes per *blob*, f_{Mfree} is the molar fraction of monomers that did not form excimer and were detected in the monomer fluorescence decay, and *x* is the pyrene content determined with Equation 1.

$$< N_{blob} > = \frac{1 - f_{Mfree}}{x} \times < n > \tag{2}$$

RESULTS AND DISCUSSION

Five sets of Py-P(C4MA-co-C18MA) copolymers were prepared by free radical polymerization with 15, 50, 70, 80, and 95 mol% of C$_{18}$MA. Each set of copolymer composition was prepared with a range of pyrene contents between 2-8 mol%, as well as an additional sample with a pyrene content of less than 1 mol% to determine the lifetime of the pyrene monomer. This Py-P(C$_4$MA-*co*-C$_{18}$MA) sample with a low pyrene content was referred to as the model compound for that copolymer series. The exact chemical composition of the Py-P(C$_4$MA-*co*-C$_{18}$MA) samples was determined through the analysis of the ^{1}H NMR and absorption spectra acquired with these samples after determining the conversion of the copolymerization by analyzing the ^{1}H NMR spectrum of the reaction mixture with the copolymer and the monomers. The fluorescence decays of the Py-P(C$_4$MA-*co*-C$_{18}$MA) samples were acquired and analyzed globally according to the FBM to determine N_{blob}, which was plotted as function of pyrene content in Figure 1A. Since N_{blob} remained constant with pyrene content in Figure 1A, the N_{blob} values were averaged to yield $<N_{blob}>$ which was plotted as a function of the average number ($<N_S>$) of atoms in the side chain for the Py-P(C$_4$MA-*co*-C$_{18}$MA) samples and the Py-PAMA samples characterized earlier[14] in Figure 1B.

The constancy of N_{blob} with pyrene content indicated that within experimental error, the pyrene derivatives do not alter the conformation of the copolymer. These N_{blob} values were averaged to yield $<N_{blob}>$ which was then plotted as a function of the average number of carbon atoms in the structural unit ($<N_s>$), along with the $<N_{blob}>$ values previously obtained for the PAMA

homopolymers. $<N_s>$ for the homopolymers represents the number of non-H atoms in the side chain, whereas for the copolymer samples, $<N_s>$ is calculated according to Equation 3.

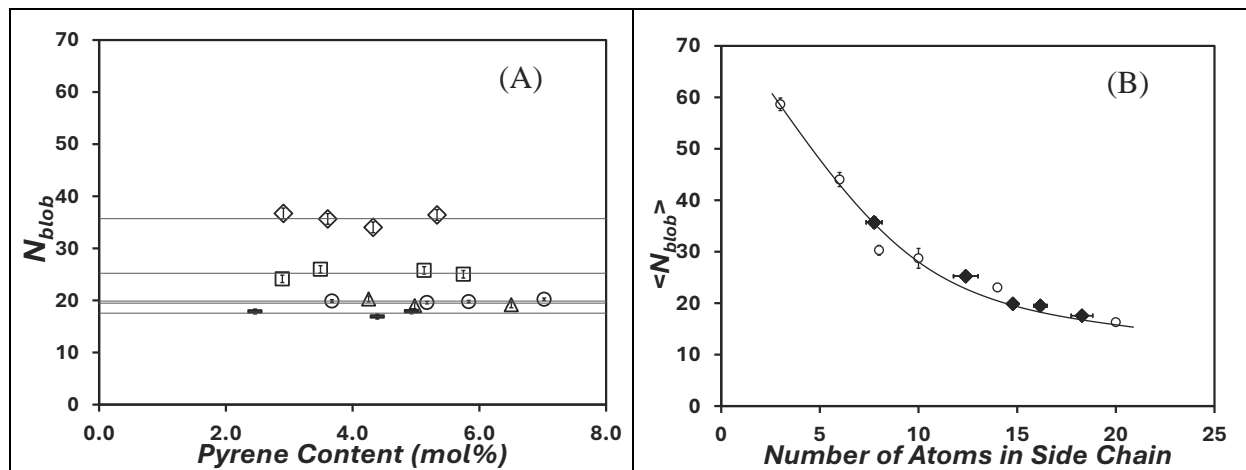$$<N_S> = 4 \times \frac{1}{1+y} + 18 \times \frac{y}{1+y} \qquad (3)$$

Figure 1. (A) Plot of $<N_{blob}>$ as a function of pyrene content for Py-P(C$_4$MA-co-C$_{18}$MA) samples with varying C$_{18}$MA compositions (15 mol% C$_{18}$MA ($y = 0.19$; $\diamond$), 50 mol% C$_{18}$MA ($y = 1.1$; $\square$), 70 mol% C$_{18}$MA ($y = 2.4$; O), 80 mol% C$_{18}$MA ($y = 4.3$; $\triangle$), 95 mol% C$_{18}$MA ($y = 21$; ▪)). (B) Plot of as a function of the number of atoms in the side chain. (O) Py-PAMA homopolymers (PC$_1$MA, PC$_4$MA, PC$_6$MA, PC$_8$MA, PC$_{12}$MA, PC$_{18}$MA),[14] (◆) Py-P(C$_4$MA-co-C$_{18}$MA) copolymers (15% C$_{18}$MA, 50% C$_{18}$MA , 70% C$_{18}$MA, 80% C$_{18}$MA, and 95% C$_{18}$MA).

For homopolymers and copolymers alike, N_{blob} exhibited a constant decrease with increasing alkyl side chain length in Figure 1B from 59 (±5) for Py-PC$_1$MA (poly(methyl methacrylate) to 16 (±1) for Py-PC$_{18}$MA (poly(stearyl methacrylate)). This decrease is indicative of a loss of flexibility in the polymeric backbone. With the introduction of longer side chains, the excited pyrenyl labels probe a smaller volume within the polymer coil due to steric hindrance. In addition, N_{blob} values of 36 (±1), 25 (±0.7), 20 (±0.2), 19 (±0.6), and 17(±0.5) were obtained for the Py-P(C4MA-co-C18MA) copolymers prepared with 15, 50, 70, 80, and 95 mol% of C$_{18}$MA, respectively. As shown in Figure 1B, these N_{blob} values matched those obtained with the homopolymers with equivalent side chain lengths. These results suggest that the persistence length of these polymers, which is related to the flexibility of the backbone, depends on the average side chain length of the methacrylate structural unit.

The methodology developed in the Duhamel lab[15] based on the modified Kratky-Porod equation, shown in Equation 4, was used with Equation 5 to calculate the persistence length of the Py-P(C$_4$MA-*co*-C$_{18}$MA) samples based on their $<N_{blob}>$ value. In Equation 5, $<r^2_{EE}>_{blob}$ is the mean squared end-to-end distance of a chain segment within a *blob*, and b is the length of a monomer unit taken to be 0.25 nm. In Equation 5, $N_{blob,\infty}$ is taken as the N_{blob} value of a fully extended chain.
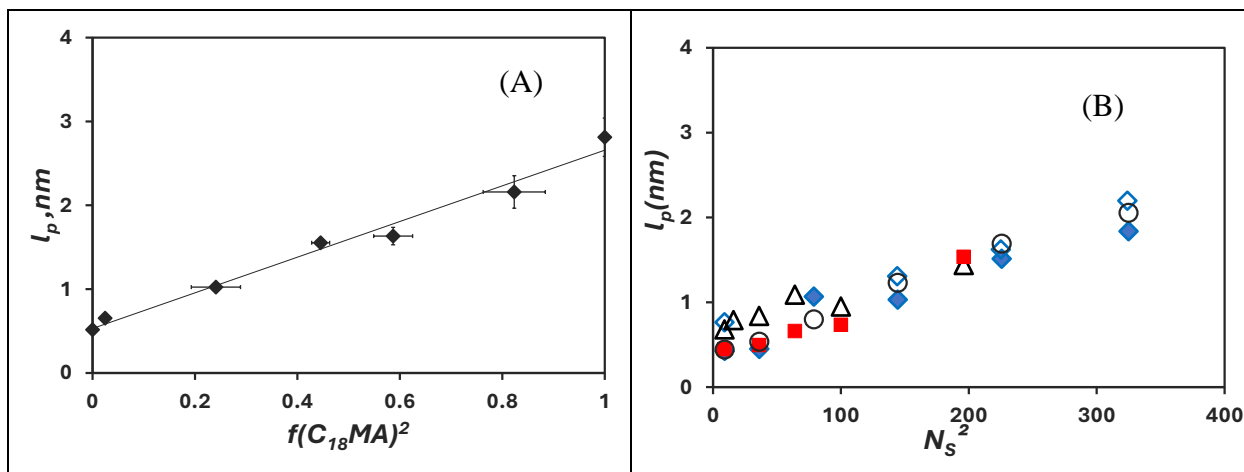
Figure 2. (A) Plot of l_p as a function of the square of the fraction of stearyl methacrylate content in the copolymer (◆). (B) Plot of l_p as a function of the square of the number of carbon atoms in the side chain for PyPEG5-PEG$_n$MA samples in DMF (◇),[15] PyBuMA-PEG$_n$MA samples in DMF (◆),[16] poly(alkyl methacrylate) where l_p was determined by intrinsic viscosity measurements (△),[3] PyBuMA-PAMA samples in o-xylene (■), and PyBuMA-PEG$_n$MA samples in o-xylene (○).

As demonstrated by Figure 2A, the persistence length increased linearly as a function of the square of the fraction of stearyl methacrylate in the copolymer, a trend which is in fundamental agreement with predictions by Fredrickson regarding the scaling of l_p with an increasing molar fraction of a bound oligomeric surfactant.[17] Unfortunately, pyrene excimer formation being controlled by diffusion, N_{blob} and l_p are both affected by solvent viscosity. As it turns out, the ideal solvent viscosity, where diffusive effects do not affect the N_{blob} and l_p values has been determined to equal 0.74 mPa.s at 25 °C, slightly larger than the viscosity of THF (0.46 mPa.s at 25 °C).[15] This implies that the persistence length determined for the copolymers in THF is only an apparent persistent length. Consequently, the fluorescence experiments conducted thus far in THF for the Py-P(C$_4$MA-co-C$_{18}$MA) copolymers will be repeated in o-xylene with a viscosity of 0.76 mPa.s at 25 °C, which is similar to the ideal viscosity (0.74 mPa.s). For instance, l_p values determined for the Py-PAMA homopolymers in o-xylene, as well as pyrene-labelled poly(oligo(ethylene glycol)methyl ether methacrylate)s (Py-PEG$_n$MAs with n = 0–5, 9, 16, 19) that have been studied in o-xylene and DMF (viscosity = 0.79 mPa.s at 25 °C) show remarkable agreement with each other when l_p was plotted against N_S^2 in Figure 2B.

$$< r_{EE}^2 >_{blob} = 2l_p(b \times N_{blob}) - 2l_p^2 \left[1 - exp \left(-\frac{b \times N_{blob}}{l_p} \right) \right] \qquad (4)$$

$$< r_{EE}^2 > = (b \times N_{blob,\infty})^2 \qquad (5)$$

CONCLUSIONS

The persistence length is frequently presented as a parameter for assessing polymer flexibility, yet due to the demanding prerequisites of current methods such as intrinsic viscosity, scattering techniques, or GPC experiments, the persistence lengths of many polymers remain unknown. This research showcases the viability of utilizing PEF to determine l_p as was done for a series of Py-P(C$_4$MA-co-C$_{18}$MA) samples. Because the FBM segregates the polymer into *blobs*, the FBM

analysis is highly suitable for polydisperse polymers such as those obtained industrially. Moreover, the methodology based on the FBM can handle any solvent in which the polymer can be dissolved as long as the solvent does not interfere with the fluorescence of pyrene, and the short butyl linker connecting the pyrene moiety to the polymer backbone ensures that the motion of the pyrene remains correlated with that of the backbone, thereby eliminating the influence of the linker on the PEF measurement itself.

The l_p values determined for the homopolymer Py-PAMA and copolymer Py-P(C$_4$MA-co-C$_{18}$MA) samples not only confirmed the theoretical predictions regarding how l_p scales with side chain length (N_S) but also with the molar fraction (f_{C18}) of comonomer. Since similar l_p values were obtaine for homopolymers (PAMA and PEG$_n$MA samples) and P(C$_4$MA-co-C$_{18}$MA) copolymers, it suggests that the polymer structure through the average side chain length affects l_p more significantly than the actual chemical composition of the side chains. Incorporating PEF into the array of methodologies already available for determining l_p might enable its determination for industrially relevant macromolecules, such as the PAMA samples characterized in the present study.

REFERENCES

(1)   Kikuchi, M.; Nakano, R.; Jinbo, Y.; Saito, Y.; Ohno, S.; Togashi, D.; Enomoto, K.; Narumi, A.; Haba, O.; Kawaguchi, S. Graft Density Dependence of Main Chain Stiffness in Molecular Rod Brushes. *Macromolecules* **2015**, *48*, 5878–5886.
(2)   Mourey, T.; Le, K.; Bryan, T.; Zheng, S.; Bennett, G. Determining Persistence Length by Size-Exclusion Chromatography. *Polymer (Guilford)*. **2005**, *46*, 9033–9042.
(3)   Tricot, M. Chain Flexibility Parameter and Persistence Length of Various Poly(Methacrylic Acid Esters). *Macromolecules* **1986**, *19*, 1268–1270
(4)   Odijk, T. The Statistics and dynamics of confined or entangled stiff polymers. *Macromolecules* **1983**, *16*, 1340–1344.
(5)   Morse, D.C. Viscoelasticity of Concentrated Isotropic Solutions of Semiflexible Polymers. 1. Model and Stress Tensor. *Macromolecules* **1998**, *31*, 7030–7043.
(6)   Savoji, M. T.; Zhao, D.; Muisener, R. J.; Schimossek, K.; Schoeller, K.; Lodge, T. P.; Hillmyer, M. A. Poly (alkyl methacrylate)-grafted polyolefins as viscosity modifiers for engine oil: A new mechanism for improved performance. *Ind. Eng. Chem. Res* **2018**, *57*, 1840-1850.
(7)   Van Horne, W. L. Polymethacrylates as Viscosity Index Improvers and Pour Point Depressants. *Ind. Eng. Chem* **1949**, *41*, 952-959.
(8)   Florea, M.; Catrinoiu, D.; Luca, P.; Balliu, S. The influence of chemical composition on the pour-point depressant properties of methacrylate copolymers used as additives for lubricating oils. *Lubr. Sci* **1999**, *12*, 31-44.
(9)   Li, T.; Li, H.; Wang, H.; Lu, W.; Osa, M.; Wang, Y.; Mays, J.; Hong, K. Chain flexibility and glass transition temperatures of poly(n-alkyl (meth)acrylate)s: Implications of tacticity and chain dynamics. *Polymer (Guilford)*, **2021**, *213*, 123207.
(10)   Rudin, A. *The Elements of Polymer Science & Engineering*; Elsevier Science & Technology Books, 1998.
(11)   Yekta, A.; Duhamel, J.; Adiwidjaja, H.; Brochard, P.; Winnik, M. A. Association Structure of Telechelic Associative Thickeners in Water. *Langmuir* **1993**, *9*, 881–883.

(12)   Duhamel, J. Global Analysis of Fluorescence Decays to Probe the Internal Dynamics of Fluorescently Labeled Macromolecules. *Langmuir* **2014**, *30*, 2307–2324.

(13)   Mathew, A. K.; Siu, H.; Duhamel, J. A Blob Model To Study Chain Folding by Fluorescence. *Macromolecules* **1999**, *32*, 7100–7108.

(14)   Thoma, J.L.; Little, H.; Duhamel, J.; Zhang, L.; Leung, K.T. Persistence Length of PEGMA Bottle Brushes Determined by Pyrene Excimer Fluorescence. *Polymers* **2023**, *15*, 3958

(15)   Little, H.; Thoma, J.L.; Yeung, R.; D'Sa, A.; Duhamel, J. Persistence Length and Encounter Frequency Determination from Fluorescence Studies of Pyrene-Labeled Poly(oligo(ethylene glycol) methyl ether methacrylate)s. *Macromolecules* **2023**, *56*, 3562 – 3573.

(16)   Farhangi, S.; Weiss, H.; Duhamel, J. Effect of Side-Chain Length on the Polymer Chain Dynamics of Poly(Alkyl Methacrylate)s in Solution. *Macromolecules* **2013**, *46*, 9738– 9747.

(17)   Fredrickson, G. H. Surfactant-Induced Lyotropic Behavior of Flexible Polymer Solutions. *Macromolecules* **1993**, *26*, 2825–2831.

SHAHRZAD GHODRATI
Chemical Engineering
Waterloo

Sensing the Invisible: An Overview of Polymeric Materials for Gas Detection

Sensing the Invisible: An Overview of Polymeric Materials for Gas Detection

Shahrzad Ghodrati, Bhoomi Mavani, Alexander Penlidis
Institute for Polymer Research, Department of Chemical Engineering, University of Waterloo

There are many applications in which sensing and monitoring hazardous gases and toxic organic analytes are important. The identification and detection of these gasses are critical to protecting human and environmental health. Hence, there is an urgent need for gas-sensing devices (i.e., gas sensors) to minimize concerns regarding health, safety, and the environment. The importance of gas sensing materials is well recognized as the sensing material is the 'heart' of a sensor that interacts with the target analyte, leading to a detection signal generated by the sensor.

This overview discusses the design and evaluation of polymeric gas sensing materials for the room-temperature detection of harmful gases.

One of the application prospects of gas sensors is in energy storage devices. Energy storage devices include fuel cells and batteries, especially with the recent surge in the popularity of lithium-ion batteries (LIBs), because of their desirable characteristics such as high specific capacity and energy, and a sufficiently long service life. Their widespread applications range from small-format batteries used in smartphones and e-notebooks, to large-format batteries used in electric vehicles and airplanes. However, enhancing safety of these energy storage devices remains a prominent aspect that requires advancements in lithium-ion batteries as it has been shown that gas evolution occurs in LIBs. Some of the common gases released in LIBs are ethylene, hydrogen, carbon dioxide, and carbon monoxide [1]. These analytes are either flammable or can cause negative health effects on humans if their concentration goes above a certain limit.

Another important gas sensing application is the detection of volatile organic compounds (VOCs) that can cause serious damage not only to human health but also to other living organisms and the environment [2]. These toxic VOCs may include but are not limited to formaldehyde, acetaldehyde, and benzene. These analytes are present indoors and outdoors in domestic and industrial settings.

Polymeric materials and metal oxides are the two main types of gas sensing materials. Metal oxide-based sensors have the advantage of high sensitivity, but they operate at elevated temperatures (150°C-500°C), necessitating the need for an additional heating source. Polymers, on the other hand, have received increased attention as sensing materials due to their room-temperature operation and their potential to be modified by incorporating dopants (like metals, metal oxides, acids, etc.) [3].

The overall research arc is on the development and evaluation of polymeric sensing materials that can detect these harmful gases in ppm levels at room temperature. Polymers modified/doped with metal oxides have displayed reasonable sensing behavior making them promising sensing materials in gas sensor applications. Polyaniline (PANI) and its derivatives, e.g., poly (2,5-dimethyl aniline), doped with various concentrations of different metal oxide nanoparticles were synthesized and evaluated as sensing materials for target analytes, along with other polymeric materials like polypyrrole (PPy), polythiophene (PTh), and polyvinylpyrrolidone (PVP).

The sorption characteristics of sensing materials were evaluated using an experimental test set-up involving a specialized gas chromatograph (as shown in Figure 1) [4][5]. In some cases, when an analyte is deemed too hazardous for a particular (academic) testing environment, a "simulant" or "surrogate" has been utilized instead. Sorption trends were used to determine the sensing performance such as sensitivity and selectivity of sensing materials (see Figure 2 as a representation of sorption studies). The effect of environmental factors (e.g., ageing), on the sensing performance, related to the sensing material stability, was also evaluated for selected sensing materials. Other property characteristics of the sensing materials were also determined using different techniques such as scanning electron microscopy (SEM), transmission electron microscopy (TEM), energy dispersive X-rays (EDX), dynamic light scattering (DLS), Brunauer-Emmett-Teller (BET) tests, and X-ray diffraction (XRD), to provide a more detailed explanation and additional confirmation of the sorption trends.
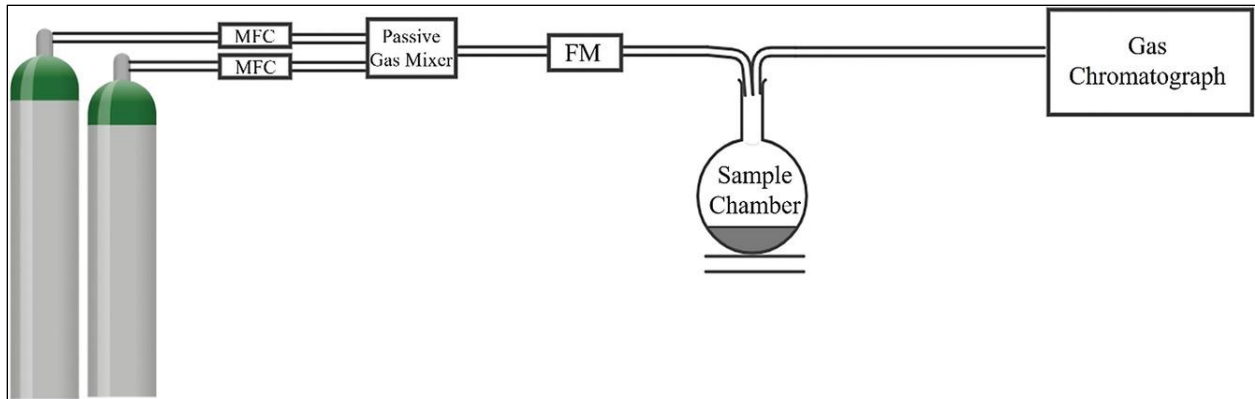
Figure 1: Gas sorption test set-up [5]. Note: MFC= Mass Flow Controller, FM= Flowmeter.
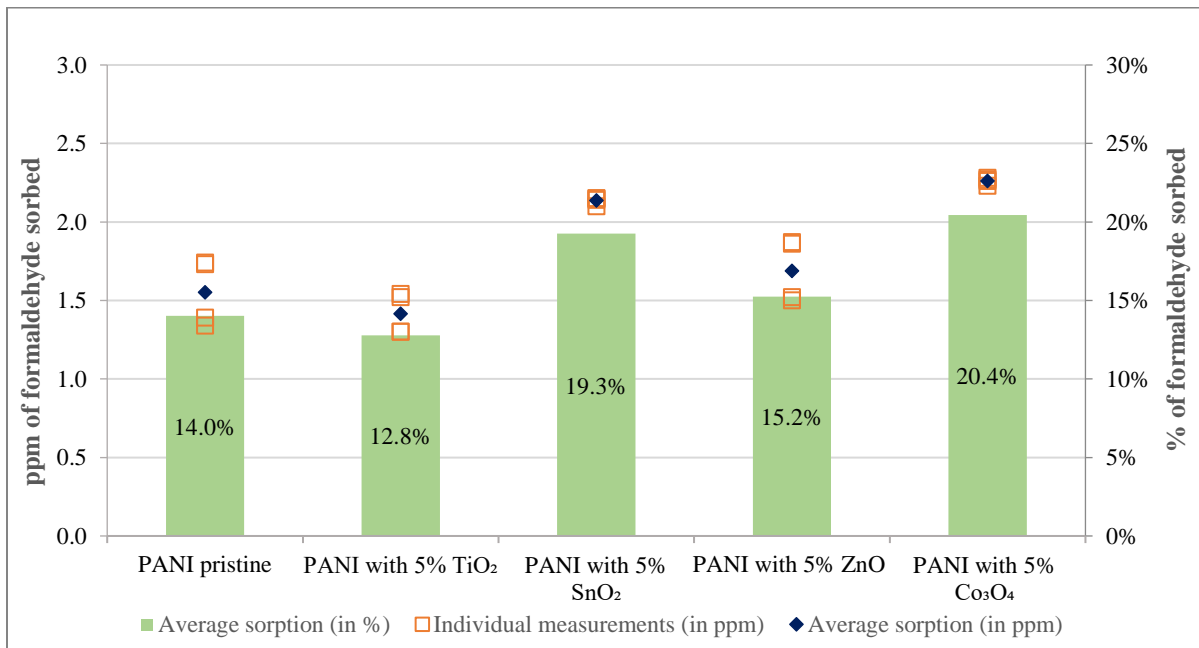

Figure 2: Formaldehyde sorption for PANI materials at 5% dopant level; (Source: F 11.1 ppm).

At this point, target analytes have been identified and the potential polymer backbones for a particular target analyte have been established. In the final step, optimal sensing materials were deposited on a MEMS (micro-electro-mechanical system) sensor which is efficient, inexpensive, and of small size. The sensor as a whole was then evaluated for its sensing performance. The process of designing/selecting the sensing materials, together with relevant examples, will be demonstrated during the IPR conference.

References

[1]   N. E. Galushkin, N. N. Yazvinskaya, and D. N. Galushkin, "Mechanism of Gases Generation during Lithium-Ion Batteries Cycling," J Electrochem Soc, vol. 166, no. 6, pp. A897–A908, 2019, doi: 10.1149/2.0041906jes.

[2]   World Health Organization (WHO) Regional Office for Europe Copenhagen, Air Quality Guidelines for Europe, Second. 2001.

[3]   L. Tirfie Zegebreal, N. A. Tegegne, and F. Gashaw Hone, "Recent progress in hybrid conducting polymers and metal oxide nanocomposite for room-temperature gas sensor applications: A review," Sens Actuators A Phys, vol. 359, p. 114472, 2023, doi: 10.1016/j.sna.2023.114472.

[4]   K. M. E. Stewart and A. Penlidis, "Novel Test System for Gas Sensing Materials and Sensors," Macromol Symp, vol. 324, no. 1, pp. 11–18, Feb. 2013, doi: 10.1002/MASY.201200062.

[5]   B. H. Mavani and A. Penlidis, "Indium Oxide Doped Polyaniline for Detection of Formaldehyde," Macromol React Eng, vol. 16, no. 6, p. 2200012, Dec. 2022, doi: 10.1002/MREN.202200012.

SAEED HADAD
Chemical Engineering
Waterloo

Highly Conductive MXene Quantum Dots/Starch Nanocomposite Polymer Electrolytes for All-Solid-State Lithium-Ion Batteries: Unveiling Insights for Future Sustainable Energy Storage

Highly Conductive MXene Quantum Dots/Starch Nanocomposite Polymer Electrolytes for All-Solid-State Lithium-Ion Batteries: Unveiling Insights for Future Sustainable Energy Storage

The escalating utilization of fossil fuels has sparked significant concerns regarding environmental pollution, underscoring the urgent need for clean, affordable, and efficient energy storage solutions. Among these, lithium-ion batteries (LIBs) have emerged as a safe and versatile energy storage technology with wide-ranging applications across the electronics industry. The current market valuation of LIBs stands at a staggering US$44.5 billion, a figure projected to soar to US$135.1 billion by 2031. However, conventional LIBs suffer from critical drawbacks, including the leakage of liquid electrolytes - notorious for their nephrotoxic and flammable nature - and dendrite growth. Consequently, there is a pressing demand for the development of eco-friendly and sustainable LIBs to meet the evolving needs of society.

Polymer electrolytes (PEs) have emerged as promising alternatives to liquid electrolytes in addressing safety concerns associated with LIBs. However, PEs often grapple with challenges such as low ionic conductivity and charge capacity. To enhance ionic conductivity, it is imperative for the electrolyte to effectively stabilize lithium cations released from the cathode structure and the dissociation of the lithium salt within the PE. Consequently, considerable research attention has been directed towards PEs with a high number of oxygen atoms in their structure, facilitating coordination with lithium cations (Li^+). Natural-based polymers, notably cellulose and starch, stand out as viable options owing to their abundance of oxygen atoms in their repeating units.

Nevertheless, it's crucial to recognize that half of the ionic conductivity and the final battery capacity are determined by the lithium salt within the PE. Upon application of a potential difference during the charging process, this salt undergoes dissociation into positive (M^+) and negative (X^-) charge species. While the electron-rich atoms in the PE can stabilize the positive part (M^+ or Li^+), the presence of unstable negative charge species within the polymer electrolyte poses challenges. These unstable negative charges (X^-) can engage in irreversible reactions with lithium cations, impeding the charge-discharge process and diminishing battery capacity and ionic conductivity. Therefore, an ideal PE should prevent the irreversible reaction of charged species

resulting from the dissociation of a lithium salt by establishing coordination with both positive and negative charge species.

This project aims to pioneer the development of all-solid-state lithium-ion batteries (LIBs) tailored for advanced energy storage applications by replacing liquid electrolytes with a solid nanocomposite electrolyte. The electrolyte design revolves around starch, a natural polymer, and $Ti_3C_2T_z$ MXene nanosheets. Starch is selected for its economic viability, biodegradability, thermal stability, and abundant electron donor oxygen atoms capable of coordinating with lithium ions (Li^+). Meanwhile, $Ti_3C_2T_z$ MXene nanosheets provide mechanical robustness, with titanium (Ti) serving as an electron acceptor to stabilize the negative part of the lithium salt (X^-) and fluorine (F) reducing the dissociation energy of the lithium salt.

The envisioned nanocomposite aims to stabilize both Li^+ and $PF6^-$, mitigating their irreversible reactions and reducing salt dissociation energy, while concurrently thwarting dendrite growth owing to its superior mechanical properties. However, a significant impediment in this endeavor is the aggregation and restacking of the MXene nanosheets. This challenge can be surmounted by modifying the hydroxyl groups of $Ti_3C_2T_z$ using 2-bromoisobutyryl bromide and sodium azide to yield N_3-functionalized MXene. Additionally, these modifications, conducted in diverse acidic reaction environments under sonication, will lead to the reduction of MXene nanosheet dimensions, thereby yielding MXene quantum dots. These quantum dots boast a higher surface area, facilitating enhanced interface interaction between the nanofiller and the polymer matrix.

Subsequently, a one-component nanocomposite can be realized by grafting cellulose acetate onto the N_3-functionalized surface of the MXene nanosheets using a novel copper-catalyzed alkyne-azide cycloaddition click reaction (please refer to the **Figure 1** to view the reaction schematic).
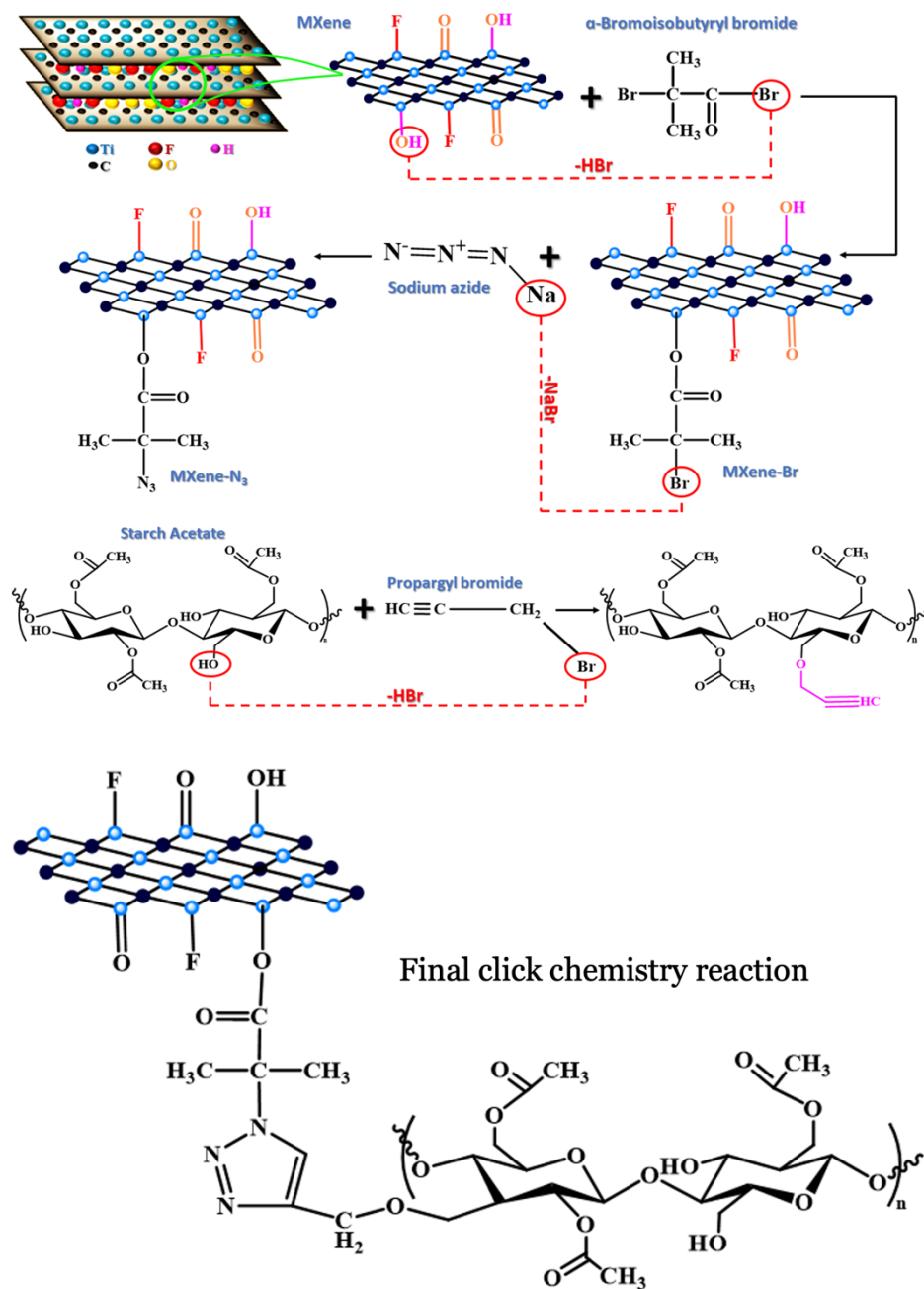
Figure 1. Schematic of the modification steps and the final reaction.

Hence, the final Starch/MXene quantum dots one-component composite presents a compelling array of advantages that underscore its potential for revolutionizing solid-state LIBs and advancing

energy storage technology. With titanium (Ti) serving as an electron acceptor, the composite effectively stabilizes the negative portion of the lithium salt (X^-), thereby enhancing the overall stability of the electrolyte. Moreover, the presence of fluorine (F) within MXene contributes to a reduction in the required dissociation energy of the lithium salt, facilitating more efficient ion transport within the electrolyte. Incorporating MXene into the composite substantially enhances its mechanical properties, providing greater resistance against dendrite growth and thereby enhancing the safety and longevity of the battery. Additionally, the oxygen (O) and hydroxyl (OH) groups present on the MXene surface facilitate the transfer of cations along the electrolyte, leading to improved conductivity and overall battery performance. Furthermore, MXene's unique crosslinking capability (due to its multifunctional surface) eliminates the need for additional crosslinking reactions during the preparation of polymer films, streamlining the manufacturing process and enhancing the structural integrity of the composite. These combined advantages position the Starch/MXene quantum dots one-component composite as a promising candidate for addressing the challenges associated with conventional LIBs and paving the way for safer, more efficient, and sustainable energy storage solutions.

This study endeavors to explore the synthesis and characterization of composites featuring diverse concentrations of MXene (10%, 30%, and 50%). Integral to this investigation are multiple analytical techniques including Fourier-transform infrared spectroscopy (FTIR), carbon-13 nuclear magnetic resonance (C^{13} NMR), and X-ray photoelectron spectroscopy (XPS) to elucidate the modification steps and anticipated reactions. Furthermore, the crystalline structure, thermal properties, and dispersion of the filler within the polymeric matrix will be thoroughly examined through X-ray diffraction (XRD), differential scanning calorimetry (DSC), thermogravimetric analysis (TGA), and transmission electron microscopy (TEM), respectively. Subsequently, the electrochemical properties of the resultant one-component composites will be comprehensively evaluated. This assessment will encompass analyses of ionic conductivity utilizing electrochemical impedance spectroscopy (EIS), determination of cation transfer number, assessment of electrochemical stability window, and characterization of charge-discharge cyclic performance, among other relevant parameters. Through this meticulous investigation, insights into the electrochemical behavior and performance of the composites will be garnered, thereby enriching our understanding of their potential utility in advanced energy storage applications.

ESTATIRA AMIRIEH
Chemical Engineering
Waterloo

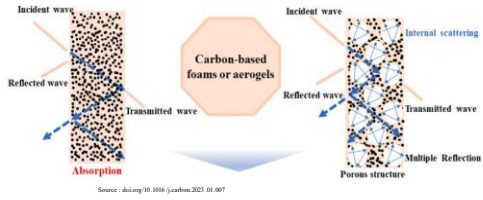# Conductive Bacterial Cellulosic Solids

Slide 1

Conductive Bacterial Cellulosic Scaffolds

PRESENTER: ESTATIRA AMIRIEH
SUPERVISORS: PROF.KAMKAR

UW IPR Symposium May 1, 2024

Slide 2

Electromagnetic Interference (EMI) Shielding

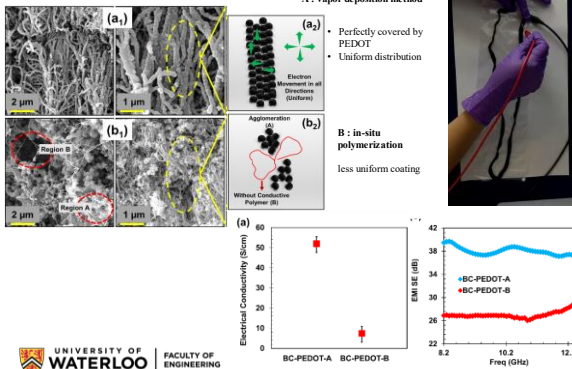Source : doi.org/10.1016/j.carbon.2023.01.007

Bacterial Cellulose

- Biocompatibility and Eco-friendliness
- High Surface Area and Porosity
- High Tensile Strength and Durability
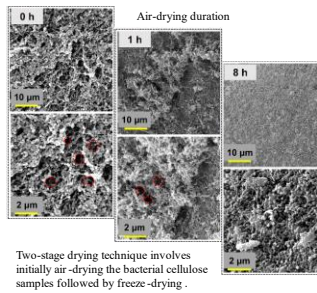- Flexibility and Moldability
- Lightweight

2

Slide 3

Conductive BC -PEDOT

A : vapor deposition method

- Perfectly covered by PEDOT
- Uniform distribution

Electron Movement in all Directions (Uniform)

B : in-situ polymerization

less uniform coating

3

Slide 4

Mix drying effect on EMI shielding

Air-drying duration

Two-stage drying technique involves initially air-drying the bacterial cellulose samples followed by freeze-drying .

4

Slide 5
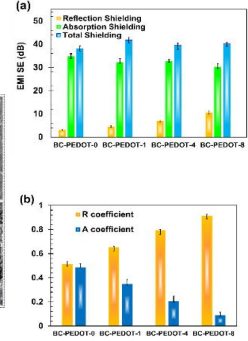
UNIVERSITY OF
WATERLOO

FACULTY OF ENGINEERING

THANK YOU FOR YOUR ATTENTION !

NAIXIN ZHAO
Chemical Engineering
Waterloo

Hydrogen-bond Bearing Conjugated Polymer for Fluoride Sensing

Hydrogen-bond Bearing Conjugated Polymer for Fluoride Sensing

Presenter: Naixin Zhao

Supervisor: Dr. Yuning Li
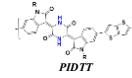
UNIVERSITY OF WATERLOO

Introduction

Fluoride-containing products

- Easily uptake by human body
- Slow excreting
- Potential kidney damage
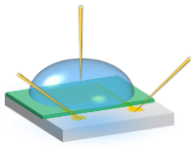
Conjugated polymer with hydrogen-bonding

PIDTT

- Simple fabrication process
- Hydrophobic nature enabled aqueous stability
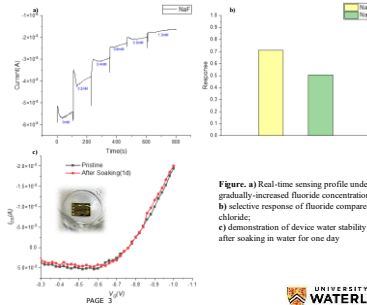- Multiple binding site for acute analysis

PAGE 2 **UNIVERSITY OF WATERLOO**

WGOFET Ion Sensor

Water-gated Organic Field-Effect Transistor (WGOFET)

Figure. a) Real-time sensing profile under gradually-increased fluoride concentration; **b)** selective response of fluoride compared to chloride; **c)** demonstration of device water stability after soaking in water for one day

PAGE 3 **UNIVERSITY OF WATERLOO**

Summary

- Hydrogen-bond bearing conjugated polymer offers high sensitivity towards fluoride
- Selectivity of fluoride ion over other halide ions (chloride)
- Hydrophilicity-enabled water stability for WGOFET operation

PRESENTATION TITLE   PAGE 4   **UNIVERSITY OF WATERLOO**

Thanks!

UNIVERSITY OF WATERLOO

TALHA INCE

Chemical Engineering

Toronto

Non-Invasive Sweat Induction for Wearable Sweat-Based Biosensors

Slide 1:

Non-Invasive Sweat Induction for Wearable Sweat-Based Biosensors

Toronto Metropolitan University

Supervisors: Dr. Hadis Zarrin & Dr. Ramdhane Dhib

MASc Student: Talha Ince

1

Slide 2:

Introduction

- Revolutionary approach to healthcare monitoring.
- Sweat contains a wealth of information reflecting the individual's physiological state.
- Current detection limits for biosensors vary from 0.15µl to 700µl.

Sweat components

Metabolites	Lactate, Glucose, Urea, Cortisol, Hydroxybutyrate, et al.
Electrolytes	Na^+, K^+, Cl^-, NH_4^+, et al.
Trace elements	Zn^{2+}, Cu^{2+}; Fe^{2+}; Ca^{2+}, et al.
Macromolecules	IL-33, IL-6, TNF-α, IFN-γ, Neuropeptide Y, et al.
Nutrients	Vitamin C and D, et al.
Drugs	Scopolamine, Paracetamol, Paroxetine, et al.

2

Slide 3:

Current Methods and Limitations

- Exercise: Needs physical activity, some people cannot.
- Iontophoresis: Needs battery to send current, burning, itchiness, redness, and pain.
- Microneedles: Punctures the skin, increased risk of irritation and infection.

Objective: To develop a method to induce sweat in a non-invasive manner that is within the detection limits of biosensors.

3

Slide 4:

Target Design Schematics

BOTTOM VIEW

Cotton for sweat collection

HPMC
PG
Azone
Oleic Acid
Pilocarpine

Backing Layer
- Made of aluminum foil to insulate the drug mix from leaving/seeping out of the top layer

Drug/Penetration Enhancer/Gel
- Special formulation consisting penetration enhancer to deliver pilocarpine deep into the skin
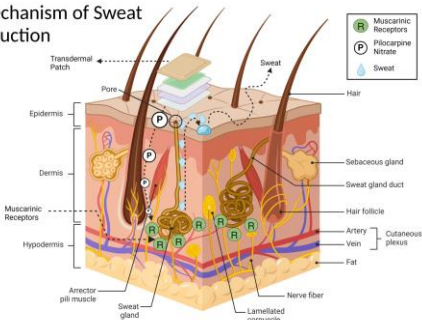
Adhesive Layer
- Adheres to the skin to prevent patch slippage

Skin
- The targeted area
- Stratum corneum (uppermost layer)
- Epidermis and dermis

4

Slide 5:

Mechanism of Sweat Induction

R Muscarinic Receptors
P Pilocarpine Nitrate
Sweat

5

Slide 6:

Technology	Sweat Produced (µl)	Time (min)	Pilocarpine Used (mg)	Degree of Invasivity*	Ref.
Iontophoresis	2	10	2.4	High	Bolat et al., 2022
Iontophoresis	43.8 ± 32.3	20	1.2 ± 0.7	High	Chen et al., 2023
Microneedle	41.2 ± 25.0	20	1.1 ± 0.4	Very high	Chen et al., 2023
Exercise (Bike)	2.25 to 270	15 to 90	None	Low	Wang et al., 2022
Exercise (Treadmill)	33.858 to 6156	20 to 360	None	Low	Bandodkar et al., 2019
Transdermal Patch	0.1 to 0.7	3 to 24	20 to 60	Low	T. Ince, R. Dhib, & H. Zarrin, 2023

6

95